# Planar Microwave Filters with Electronically Tunability and Other Novel Configurations

**Wenxing Tang**

A dissertation submitted for the degree of Doctor of Philosophy

Heriot-Watt University

School of Engineering and Physical Sciences

<May> <2011>

# Abstract

In order to meet the increasing demands of advance wireless communications and radar systems, several novel types of bandpass filters and bandstop filters have been developed in this thesis.

A new type of varactor-tuned dual-mode bandpass filters have been presented to achieve a nearly constant absolute bandwidth over a wide tuning range by using a single DC bias circuit. Since the two operating modes (i.e., the odd and even modes) in a dual-mode microstrip open-loop resonator do not couple to each other, tuning the passband frequency is accomplished by merely changing the two modal frequencies proportionally. Design equations and procedures are derived, and two two-pole tunable bandpass filters and a four-pole tunable bandpass filter of this type are demonstrated experimentally.

Miniature microstrip doublet dual-mode filters that exhibit quasi-elliptic function response without using any cross coupling have been developed. It shows that a single two-pole filter or the doublet can produce two transmission zeros resulting from a double behaviour of the dual-mode resonator of this type. Electromagnetic (EM) simulation and experiment results of the proposed filters are described.

Parallel feed configuration of a microstrip quasi-elliptic function bandpass filter has been built with a pair of open-loop dual-mode resonators. By employing this new coupling scheme, a novel filter topology with three-pole quasi-elliptic function frequency response can be obtained, leading to good passband performance, such as low insertion loss and good matching at the mid-band of passband. A designed three-pole bandpass filter of this type is demonstrated experimentally.

A new class of dual-band filters based on non-degenerate dual-mode microstrip slow-wave open-loop resonators, which support two non-degenerate modes that do not couple, have been introduced. Different feed schemes that affect the filtering characteristics are investigated. Examples of dual-band filters of this type are described with simulation and experiment results.

In order to achieve a wide spurious-free upper passband, a novel design of bandstop filter with cancellation of first spurious mode by using coupled three-section step impedance resonators (SIRs) has been developed. This cancellation occurs when two transmission poles coincide with the first spurious mode (transmission zero) by properly choosing the step impedance ratio and the gap between the SIR and the main transmission line. A stripline bandstop filter and a microstrip bandstop filter of this type are designed, fabricated and tested. As a preliminary investigation, the microstrip filter is tuned electronically using ferroelectric thin film varactors.

# Dedication

To my mother, Yanping, for her great and ever-lasting love and support.

# Acknowledgements

I would like to express my deep appreciation to my supervisor, Professor Jia-Sheng Hong, for his expert guidance throughout my PhD studies. His contributions, suggestions and insight have been invaluable. Without his kindest help and encouragement, completing my research work would not have been possible.

A special thanks goes to Dr. Zhangcheng and Dr. Young-Hoon, for all their time and assistance. I would like to extend my thanks to my friends, Alex, Shilong, Jiani, Liz, Nana, Qingxu, Yejing and Yufen, for their help and friendship.

I am particularly thankful for my friend, Xiang Pan, for her help and encouraging me to pursue my postgraduate studies. I am also grateful to Mr. Jiantang Wu, for his inspiration and encouragement.

I am grateful for the support of my institution, the Department of Electrical, Electronic and Computer Engineering at Heriot-Watt University.

Most importantly, I would like to thank my family, especially my parents and my sisters, for giving me their great and ever-lasting love and support.

ACADEMIC REGISTRY
**Research Thesis Submission**

| | | | |
|---|---|---|---|
| Name*:* | WENXING TANG | | |
| School/PGI: | EPS/EECE | | |
| Version: *(i.e. First, Resubmission, Final)* | Final | Degree Sought (Award **and** Subject area) | PhD in Microwave Engineering |

## Declaration

In accordance with the appropriate regulations I hereby submit my thesis and I declare that:

1) the thesis embodies the results of my own work and has been composed by myself
2) where appropriate, I have made acknowledgement of the work of others and have made reference to work carried out in collaboration with other persons
3) the thesis is the correct version of the thesis for submission and is the same version as any electronic versions submitted*.
4) my thesis for the award referred to, deposited in the Heriot-Watt University Library, should be made available for loan or photocopying and be available via the Institutional Repository, subject to such conditions as the Librarian may require
5) I understand that as a student of the University I am required to abide by the Regulations of the University and to conform to its discipline.

* *Please note that it is the responsibility of the candidate to ensure that the correct version of the thesis is submitted.*

| | | | |
|---|---|---|---|
| Signature of Candidate*:* | | Date: | |

## Submission

| | |
|---|---|
| Submitted By *(name in capitals):* | WENXING TANG |
| Signature of Individual Submitting: | |
| Date Submitted: | |

## For Completion in the Student Service Centre (SSC)

| | | | |
|---|---|---|---|
| *Received in the SSC by (name in capitals):* | | | |
| *Method of Submission* *(Handed in to SSC; posted through internal/external mail):* | | | |
| *E-thesis Submitted (**mandatory for final theses**)* | | | |
| Signature: | | Date: | |

Table of Contents

# List of Tables

# List of Figures

# List of Publications by the Candidate

1. **W. Tang** and J.-S. Hong, "Varactor-Tuned Dual-Mode Bandpass Filters," *Microwave Theory and Techniques, IEEE Transactions on*, vol. 58, pp. 2213-2219, 2010.

2. **W. Tang** and J.-S. Hong, "Coupled stepped-impedance-resonator bandstop filter," *Microwaves, Antennas & Propagation, IET*, vol. 4, pp. 1283-1289, 2010.

3. **W. Tang** and J.-S. Hong, "Microstrip quasi-elliptic function bandpass filter with improved tuning range," presented at Microwave Conference (EuMC), 2010 European, 2010.

4. **W. Tang**, J.-S. Hong, and Y.-H. Chun, "Compact Tunable Microstrip Bandpass Filters with Asymmetrical Frequency Response," presented at Microwave Conference, 2008. EuMC 2008. 38th European, 2008.

5. **W. Tang** and J.-S. Hong, "Tunable microstrip quasi-elliptic function bandpass filters," presented at Microwave Conference, 2009. EuMC 2009. European, 2009.

6. **W. Tang** and J.-S. Hong, "Quasi-elliptic function doublet filters without cross coupling," presented at Microwave Conference, 2009. EuMC 2009. European, 2009.

7. J.-S. Hong and **W. Tang**, "Dual-band filter based on non-degenerate dual-mode slow-wave open-loop resonators," presented at Microwave Symposium Digest, 2009. MTT '09. IEEE MTT-S International, 2009.

8. **W. Tang**, J.-S. Hong and Y.-H. Chun, "Microstrip cross-coupled stepped-impedance line bandstop filter," presented at Microwave Symposium Digest, 2009. MTT '09. IEEE MTT-S International, 2009.

9. **W. Tang** and J.-S. Hong, "Parallel Feed Microstrip Quasi-Elliptic Function Bandpass Filter," *accepted by Microwave Conference (EuMC), 2011 European.*

# Chapter 1

# INTRODUCTION

## 1.1 Motivation

Filters play important roles in many RF/microwave modern wireless systems such as radar, wireless communications, radio astronomy, navigation, sensing and medical instrumentation [1]. They are employed to separate and combine or select and reject signals at various frequencies. With the emerging novel wireless communications, more frequency spectrum is in great demanded. However, the frequency spectrum as a resource is valuable and limited. This continue to challenge RF/microwave filters with ever more stringent requirements such as low insertion loss, high selectivity, linear phase, small size, light weight and lower cost [1]-[3].

Dual-mode resonators have been widely employed to realize many RF/microwave filters because each of dual-mode resonators can be used as a doubly tuned resonant circuit, and therefore the number of resonators required for a given degree of filter is reduced by half, resulting in a compact filter configuration [4]-[8]. In addition, the two modes can be built in such way that they do not couple to each other [9]-[10]. For these reasons, novel dual-mode filter designs have been investigated intensively in recent years.

Dual-mode tunable or reconfigurable filters are attractive because it is compact in size and high selectivity due to a finite-frequency transmission zero associated with the even mode of the dual-mode resonator. This type of filter can be tuned in a simple way that is controlling its odd and even-mode resonant frequencies by loading different capacitance for each mode since the two modes do not couple [11]-[12]. However, two DC bias circuits are required for this type of tunable filter, moreover, the tuning range is quite limited (only about 10%) for a constant absolute bandwidth tuning. This brings some challenges for commercial wireless systems, where single DC bias scheme and wider tuning range are preferred. In this thesis, a possible solution is addressed, in which, a wideband transformer and odd/even-mode tuning rate method are employed, leading to a wider tuning range of 41% by using a single DC bias circuit to control.

High selectivity on both sides of passband is usually demanded for a transmitter bandpass filter, to reduce the interference in adjacent channels and other frequency bands. In convention, high selectivity can be achieved by introducing cross coupling between non-adjacent resonators or input/output of the filter [1]. By using this technique, a pair of finite-frequency transmission zeros can be produced at each side of passband, resulting in a quasi-elliptic function response, hence, high selectivity can be obtained. In difference with this, quasi-elliptic function doublet filters (high selectivity filters) can be built without cross coupling, leading to a compact size with high selectivity performance, which will be discussed in more detail in the thesis.

Low insertion loss is critical requirement in transmitter and receiver filters, which improves the transmitter's efficiency, reduces the thermal load, and improves the receiver's noise figure. Dual-mode resonators are cascaded to form a higher order filter in [10], resulting high selectivity on each side of passband. The higher order filter suffers from higher insertion loss due to the cascading. This is a common problem in conventional filter design. In order to reduce the insertion loss for higher order dual – mode filters, a parallel feed configuration of dual-mode resonators is introduced in this thesis. The proposed parallel feed filter obtains nearly half insertion loss less than the one in [10]. However, its out of band rejection level becomes poorer.

Dual-band filters have gained more attention due to the recent development in wireless communication and radar systems where a dual-band operation is required. Many dual-band filters have been developed to meet the high-quality miniature requirements of the dual-band operation systems. Stepped impedance resonator (SIR) dual-band filters have been demonstrated [13]-[14], stub-line dual-band filters are realized in [15] and a dual-mode waveguide structure has been used in dual-band filter design [16]. In order to minimize the filter size, a novel class of dual-band filters based on the dual-mode microstrip slow-wave open-loop resonator have been investigated in this thesis.

Bandstop filters (or notch filters) have become more and more important in modern wireless systems, which are frequently employed to reject unwanted signals or interference at air interfaces between different systems. Usually, transmission line bandstop filters comprised of distributed resonators would have encountered a restriction on the extent of the upper passband. This type of bandstop filters have had

their second harmonic response centered at no more than three times the fundamental resonant frequency, which fail to meet the requirement of wideband systems. Recent efforts have been made to overcome this restriction by capacitance-load technique [17] or by using compound resonator technique [18] to push the first spurious mode away. In this thesis, an alternative new technique is proposed to cancel or suppress the first spurious mode, leading to a wide upper passband. How to tune the center frequency of this type of bandstop filter is also discussed.

## 1.2 Objectives

The thesis is constructed around the following objectives:

- ✓ To develop dual-mode tunable filters with (a) wider tuning range for a constant absolute bandwidth, (b) using single DC bias scheme, (c) achieving high selectivity on each side of passband by using higher order configuration.

- ✓ To develop compact quasi-elliptic function doublet filters without cross coupling.

- ✓ To develop higher order dual-mode resonator filter with low insertion loss and good mid-band performance.

- ✓ To develop a novel class miniature of dual-band filters using capacitively loaded slow-wave resonators.

- ✓ To develop a novel type of bandstop filter with harmonic suppression, this is required for wideband systems. The tunable bandstop of this type is also to be developed.

## 1.3 Organization of the thesis

Following the introduction, Chapter 2 provides a review of novel tunable or reconfigurable filters and novel dual-mode resonator filters. Band stop filters with various techniques for harmonic suppression are also discussed.

In Chapter 3, some basic theories of filters related to the thesis are addressed.

Chapter 4 describes a novel class of varactor-tuned dual-mode bandpass filters. Design equations and procedures of the proposed filters are derived in a systematical way. The theoretical, full-wave electromagnetic (EM) simulated and measured performances are present. Good agreement between these results is obtained.

In Chapter 5, dual-mode resonator filters with novel configurations are investigated, such as compact quasi-elliptic function doublet filters without cross coupling, higher order dual-mode resonator filter using parallel feed configuration, and miniature dual-band dual-mode filters. The experimental results of these filters are presented.

Chapter 6 introduces a novel type of bandstop filter with harmonic suppression. The cancellation (or suppression) of the first spurious mode (transmission zero) is explained theoretically and validated experimentally. In addition, the tunability of the bandstop filter of this type is also discussed.

Finally, a brief summary of the contributions of the presented works and suggestions for future research work are concluded in Chapter 7.

# Chapter 2

# LITERATURE REVIEWS

## 2.1 Novel Electrically Tunable Filters

Electronically tunable (or reconfigurable) filters are attracting more attention for research and development due to their increasing importance in multiband systems, wideband radar and electronic warfare systems [19]. In general, based on various tuning elements used, tunable filters may be classified as semiconductor (varactor and p-i-n diodes) tunable filters [20]-[29], RF microelectromechanical systems (MEMS) tunable filters [30]-[37], piezoelectric transducer (PET) tunable filters [38]-[41], and ferroelectric materials tunable filters [42]-[46]. A well-known problem for tunable filters is the variation of the bandwidth as the center frequency is tuned. This is mainly due to the frequency dependence of the coupling networks. Various techniques have been addressed to overcome this problem, to achieve constant absolute bandwidth over a broad tuning range using different tuning elements. They are described in the following.

### *2.1.1 Semiconductor (varactor and p-i-n diodes) tunable filters*

Semiconductor technologies are a very popular choice for making tunable filters because of their reliability, compact in size, fast tuning speed and low cost. Many tunable filters have be demonstrated based on varactor or p-i-n diodes and discussed below.

#### *2.1.1.1 Combline tunable filter using input and output compensation method*

A microstrip combline filter is a popular structure for developing tunable or reconfigurable filters. Figure 2-1 illustrates a schematic view of a combline tunable filter [20], where each microstrip line resonator, whose length is about a quarter-wavelength at the operating frequency, is short-circuited at one end and loaded with a

varactor at the other end. In order to achieve a constant absolute bandwidth over a broad tuning range, additional input and output coupling networks are employed to compensate the internal coupling between resonators. The equivalent circuit of the combline filter is depicted in Figure 2-2.

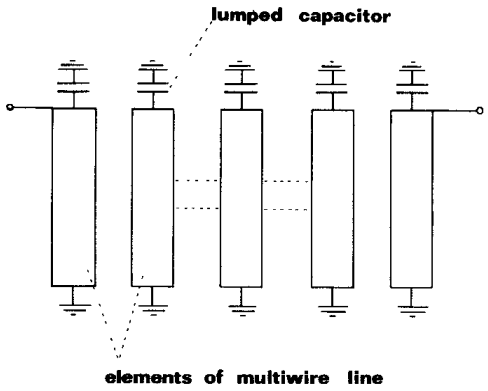


Figure 2-1. Schematic of tunable combline filter (lumped capacitor are replaced by varactor) [20].

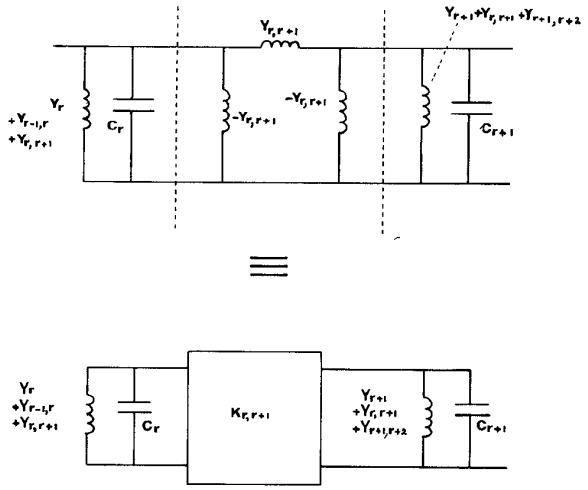

Figure 2-2. Equivalent circuit of combline filter between resonator nodes [20].

Notice that the couplings between transmission lines are constrained to adjacent lines. It shows that the internal coupling between resonators can be considered as an inverter formed from a pi section of the short-circuited stubs given in (2.1)

$$K_{r,r+1} = Y_{r,r+1} / \tan(a\omega) \qquad (2.1)$$

where $a$ is a constant value of the design specification. It is clear that the inverter response depends on the electrical length of the short-circuited stubs that are dependent on frequency. To achieve a constant absolute bandwidth over a wide tuning range, the frequency dependence must be removed. For this reason, the admittance of the entire network is scaled by a factor $\tan(\theta)/\tan(\theta_0)$, where $\theta_0$ is the electrical length of the resonator at resonant frequency $\omega_0$. Thus, the admittance of the $r$ th resonator is given as

$$Y_r^{'} = \frac{j[\omega C_r \tan(\theta) - (Y_r + Y_{r-1,r} + Y_{r,r+1})]}{\tan(\theta_0)} \qquad (2.2)$$

The bandwidth of the filter was obtained by applying the frequency transformation from lowpass prototype to bandpass response, which is given by

$$\omega = \frac{2\omega_0}{\alpha\{\tan(\theta_0) + \theta_0[1 + (\tan(\theta_0)^2)]\}} \qquad (2.3)$$

with

$$\alpha = \frac{Y_r + Y_{r-1,r} + Y_{r,r+1}}{C_{Lr}\tan(\theta_0)} \qquad (2.4)$$

where $C_{Lr}$ denotes the shunt capacitor of the lowpass prototype. From (2.3), it can be seen that the bandwidth of the filter keeps nearly constant over a broad tuning range when $\theta_0 = 53$ (degree). In addition, to remove the frequency variation of the source $G_S$ and the load $G_L$ due to the scaling factor, a redundant impedance transform network has to be introduced at the input and output of the filter shown in Figure 2-3.

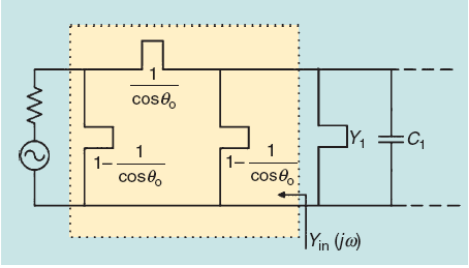


Figure 2-3. Impedance transforming network at input and output of the filter [20].

The input admittance including the impedance transforming network may be derived as

$$Y_{in}(j\omega) = \frac{\sin(2\theta)}{\sin(2\theta_0)} + j[\frac{\cos(2\theta) - \cos(2\theta_0)}{\sin(2\theta_0)}] \qquad (2.5)$$

The real part of the input admittance varies slowly with frequency while the imaginary part is resonant at $\theta_0$. The optimum return loss performance may be achieved by choosing $\theta_0$=45˚.

#### *2.1.1.2 Tunable combline bandpass filter employing step-impedance microstrip lines*

It is well-known that to maintain constant filter response shape and bandwidth, coupling coefficient *k* between resonators must vary inversely with the tuning frequency and external $Q_e$ must also vary directly with the tuning frequency as expressed in the following equations [47]

$$k_{j,j+1}\Big|_{j=1ton-1} = \frac{J_{j,j+1}}{\sqrt{b_j b_{j+1}}} = \frac{FBW}{\sqrt{g_j g_{j+1}}} \propto \frac{1}{f_0} \qquad (2.6)$$

$$Q_e = \frac{b_1}{(J_{01})^2 / G_A} = \frac{g_0 g_1}{FBW} \propto f_0 \qquad (2.7)$$

In order to control the coupling coefficient between resonators of a combline filter, a step-impedance microstrip line method was introduced by Kim et al. [21] as depicted in Figure 2-4. The magnetic coupling is maximum closing to the short-circuited end where the current has highest density while electric coupling is maximum at the opposite ends. By allowing larger gaps near short-circuited ends, the magnetic coupling between microstrip lines will be reduced while the electric coupling remains nearly the same. In this way, the portion of magnetic coupling to electric coupling is changed, which can be utilized to satisfy the coupling coefficient required for the constant absolute bandwidth tuning. Notice that a pairs of lumped inductors are employed for the input and output

coupling. To meet the requirement of the external $Q_e$, the values of the inductor and the position connecting to the first and last resonators are adjusted.

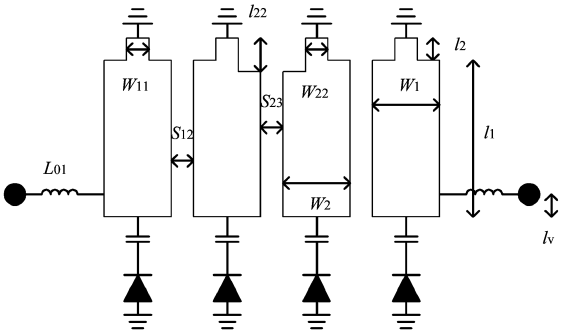


Figure 2-4. Varactor-tuned combline bandpass filter using step-impedance microstrip lines [21].

The experimental performance is displayed in Figure 2-5. it can be seen that the 3-dB passband bandwidth varies less than 3.2% within the 250MHz tuning range at 2GHz.

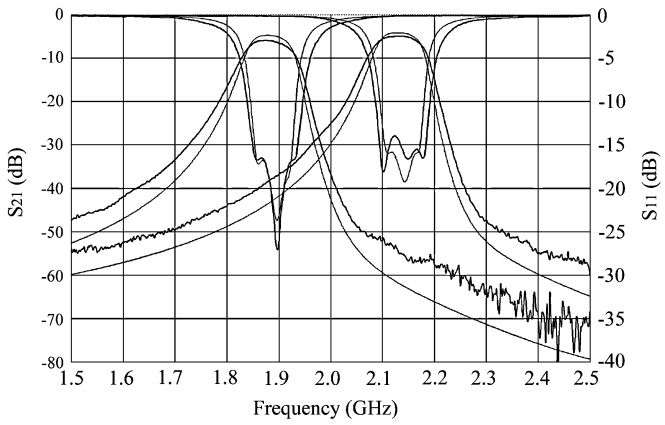


Figure 2-5. Simulated and experimental results of the combline filter using step-impedance microstrip lines [21].

### *2.1.1.3 Tunable combline filter using variable coupling reducer*

The coupling between resonators of a combline filter can also be controlled by placing variable coupling reducer between the resonators depicted in Figure 2-6 [22]. It can be seen that the coupling reducer is designed as detuned resonator made up of a line

segment ending in a variable capacitor. When the varactor loaded at the end of coupling reducer varies, the admittance $Y_{bw}$ (see Figure 2-6(c)) is changed, hence, the coupling between the resonators in adjusted. In this way, the bandwidth of the filter response can be controlled, leading to a constant bandwidth over a wide tuning range.

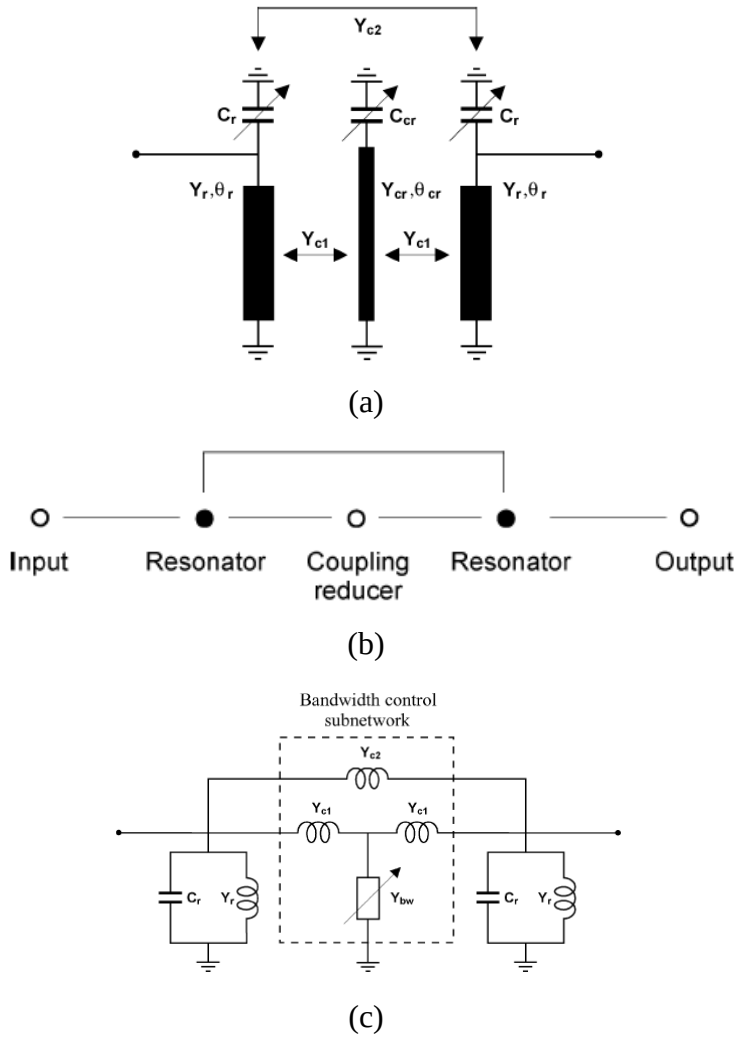


Figure 2-6. Second-order combline filter with variable coupling reducer (a) Circuit diagram. (b) Coupling scheme and (c) Equivalent circuit [22].

The short-circuited end lines are employed for the input and output coupling. This type of structure is usually used in tunable filter designs, which exhibits a dominant inductive coupling with wideband behaviour. A fabricated three-pole filter of this type and its measured performance are shown in Figure 2-7.

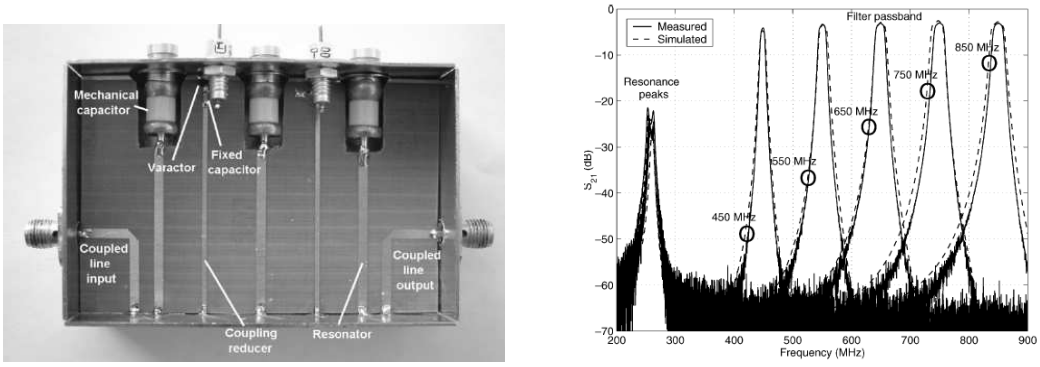


(a) (b)

Figure 2-7. (a) Fabricated combline filter with variable coupling reducer and (b) Measured results [22].

### *2.1.1.4 Tunable filters with corrugated microstrip lines coupled*

Corrugated microstrip coupled lines can be utilized to achieve constant absolute bandwidth over a board tuning range [23]. By using the corrugated coupled-line, a mixed coupling scheme can be obtained. The diagram of the corrugated coupled-line is given in Figure 2-8.

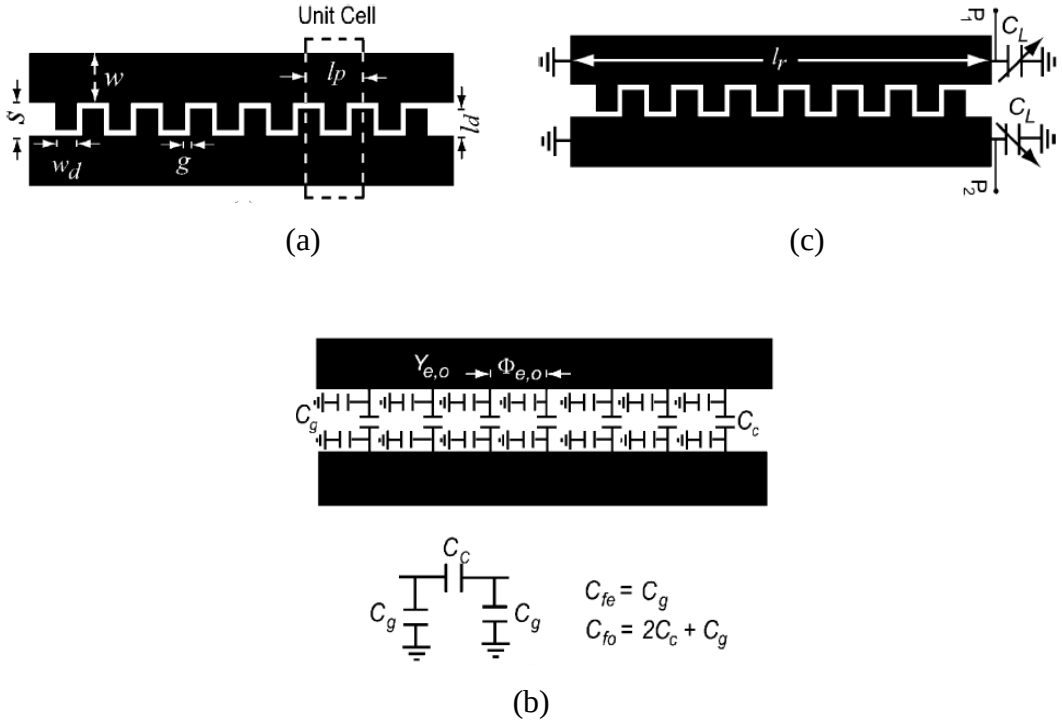


(a) (c)

(b)

Figure 2-8. (a) Corrugated coupled line and (b) Electrical modal (c) Corrugated coupled-lines with a loading capacitor $C_L$ [23].

The Y matrix of the coupled resonators with a tuning capacitor $C_L$ is derived as

$$Y = \begin{bmatrix} \frac{Y_{re}+Y_{ro}}{2} + j\omega C_L & \frac{Y_{re}+Y_{ro}}{2} \\ \frac{Y_{re}+Y_{ro}}{2} & \frac{Y_{re}+Y_{ro}}{2} + j\omega C_L \end{bmatrix} \tag{2.8}$$

where $Y_{re}$ and $Y_{ro}$ denote the even and odd admittance of the two coupled resonators. The coupling coefficient $k_{21}$ is given by

$$k_{21} = \frac{\mathrm{Im}[Y_{12}(\omega_0)]}{b} = \frac{BW}{f_0\sqrt{g_1 g_2}} \tag{2.9}$$

with

$$b = \mathrm{Im}\left[\frac{\omega_0}{2}\frac{\partial Y_{r11}(\omega_0)}{\partial\omega} - \frac{Y_{r11}(\omega_0)}{2}\right], \qquad Y_{r11} = \frac{Y_{re}+Y_{ro}}{2} \tag{2.10}$$

For a given electrical length, the coupling coefficient $k_{21}$ can be synthesized by controlling the even and odd mode fringe capacitance and choosing the length, width and gaps between the corrugations lines. The variation of $k_{21}$ versus center frequency for various corrugation capacitance $C_{fo}$ is displayed in Figure 2-9(a). It is clear that by choosing proper dimensions of the corrugation lines, the coupling coefficient can be controlled to achieve constant absolute bandwidth tuning. The measured results are displayed in Figure 2-9(b). The two finite transmission zeros are introduced by the two additional input and output coupled lines.

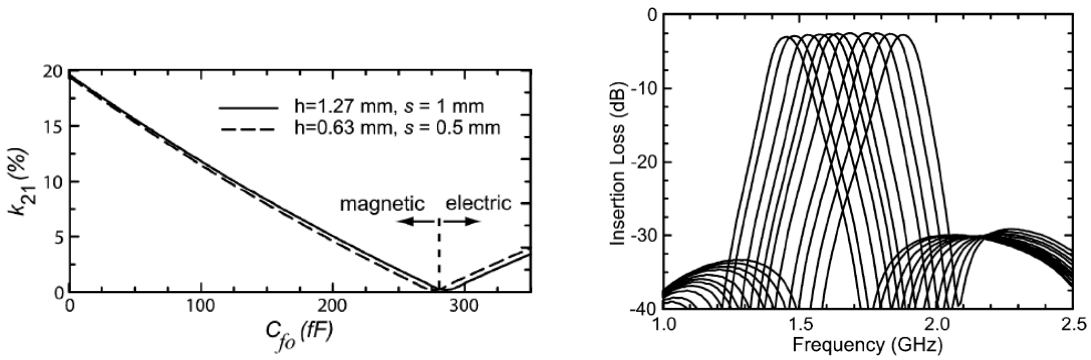


(a) (b)

Figure 2-9 (a) Corrugated coupled $k_{21}$ versus $C_{fo}$. (b) Measured performance [23].

### *2.1.1.5 Reconfigurable filter using a self-scalable combline structure*

A self-scalable combline topology has been investigated in [24]. In difference with conventional tunable filter, where varactor is usually employed to tune the center frequency response, the self-scalable combline switchable filter changes both loading capacitors and the electrical length of resonators to achieve electrically identical in all modes of operation, which is illustrated in Figure 2-10. It can be seen that when the electrical length of the resonators is switched to shorter, the loading capacitors are changed to small value as well. In this way, the passband bandwidth can be maintained nearly constant over a wide tuning range.

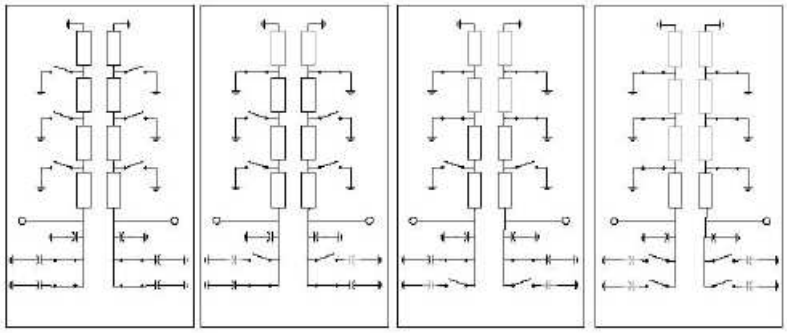

Figure 2-10. Schematic diagrams of different operational modes of the filter [24].

### *2.1.1.6 Reconfigurable filter using lumped-distributed coupled resonators*

The coupling between resonators can be controlled by employing lumped-distributed coupled transmission lines [25]. Figure 2-11 gives the structure of the lumped-distributed coupled transmission lines.

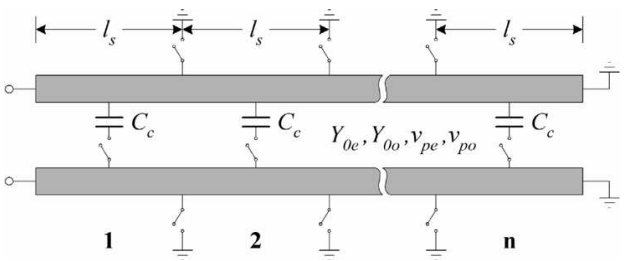


Figure 2-11. Lumped-distributed quarter-wave coupled resonators [25].

Both the capacitors and the electrical length of the resonator can be switched separately as seen from Figure 2-11. Because the lumped capacitive coupling is antiphase to the distributed electromagnet coupling, the total coupling between the resonators can be controlled by changing the lumped capacitors or the gaps between the resonators. This is illustrated in Figure 2-12. To this end, the constant absolute bandwidth can be achieved by switching on proper lumped capacitors while the center frequency is tuned by selecting different electrical length of the resonators. Note that the change in the length of the coupled lines not only contributes to the tuning of the center frequency, but also adjusts the mutual coupling between adjacent resonators.

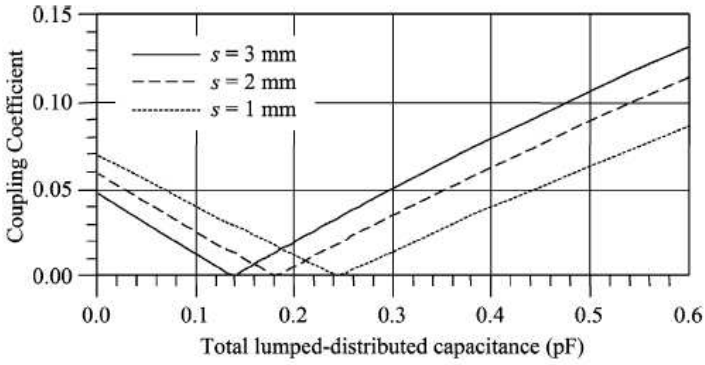


Figure 2-12. Coupling coefficient of lumped-distributed coupled lines versus gap (s) [25].

### *2.1.1.7 Tunable filter with independent electric and magnetic coupling*

Park et al. [26] introduced a tunable filter with independent electric and magnetic coupling shown in Figure 2-13.

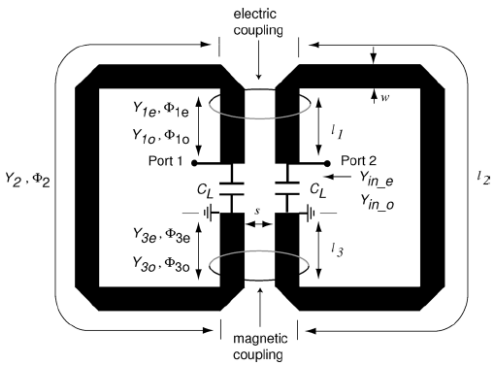


Figure 2-13. Electrical circuit model of the filter [26].

It can be seen that the electric coupling is dominant at the open end of the resonator while magnetic coupling is dominant at the short-circuited ends of the resonators where the current has maximum density. By changing the length of the coupling lines, the portion of electric coupling to magnetic coupling can be adjusted. In other words, the coupling coefficient between the resonators can be controlled against the operating frequency, which is shown in Figure 2-14.

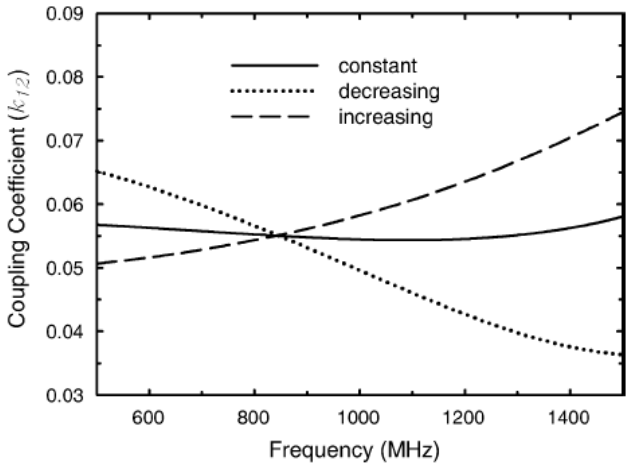


Figure 2-14. The coupling coefficient $k_{12}$ varies with frequency [26].

A wideband transformer is employed as the input and output coupling network shown in Figure 2-15. By properly choosing the transformer section parameters such as $l_s$ and $C_m$, relatively small variation in external coupling $Q_e$ over the entire tuning range can be achieved.

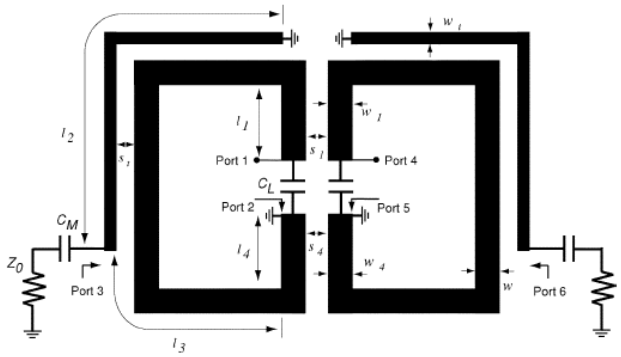


Figure 2-15. Electrical circuit model of the resonator with the external coupling circuit [26].

### *2.1.1.8 Tunable filters using a novel mixed electric and magnetic coupling scheme*

A novel approach for designing tunable filters with constant absolute bandwidth tuning has been introduced by Zhang et al. [27]. The coupling coefficient between resonators is controlled by using a novel mixed electric and magnetic coupling scheme illustrated in Figure 2-16.

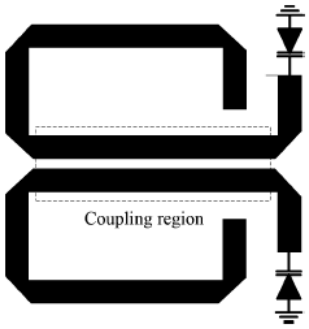


Figure 2-16. Inter-stage coupling structure [27].

The two resonators are coupled to each other through a specified coupling region. To understand how the coupling coefficient can be controlled, normalized voltage and current distributions on the resonator at different resonant frequencies have been investigated given in Figure 2-17. With the voltage and current distributions, the electric and magnetic coupling coefficient $k_e$ and $k_m$ can be expressed as

$$\left|k_{e,i}\right| = p\int_{d1}^{d2}\left|V_i(x)\right|^2 dx \qquad (2.11)$$

$$\left|k_{m,i}\right| = p\int_{d1}^{d2}\left|I_i(x)\right|^2 dx \qquad (2.12)$$

The overall coupling coefficient can be given by

$$\left|k_i\right| = \left|k_{m,i}\right| - \left|k_{e,i}\right| \qquad (2.13)$$

From Figure 2-17, it is clear that by properly choosing the coupling region, the overall coupling coefficient can vary inversely with frequency, which can meet the requirement of constant absolute bandwidth.

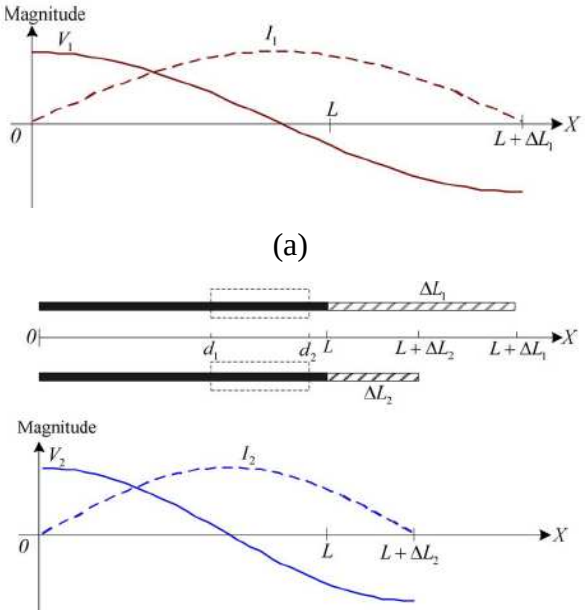


(a)

(b)

Figure 2-17. Normalized voltage and current distributions on the resonator (a) at lower frequency. (b) at upper frequency [27].

A L-shape capacitive network is employed for the input and output coupling network, which not only can meet the requirement of the external $Q_e$, but also can suppress the second harmonic. The layout of the fabricated circuit and its measured performance are present in Figure 2-18. The results show that the tuning range is from 650 to 960MHz with 1-dB absolute bandwidth is $80 \pm 3.5$MHz.

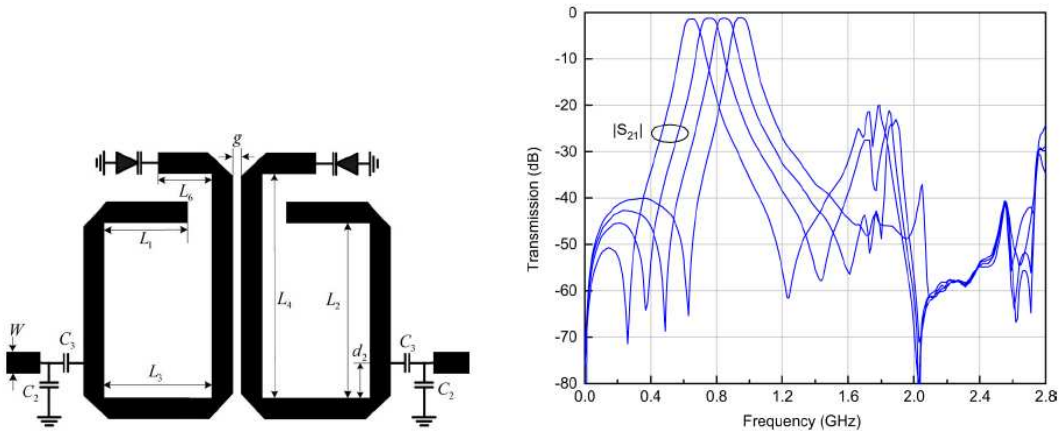


(a)

(b)

Figure 2-18. (a) The fabricated filter using a novel mixed electric and magnetic coupling scheme and (b) Measured performance [27].

### *2.1.1.9 Tunable filters employing Π-and L-capacitive coupling scheme*

Kapilevich et al. introduced Π- and L-capacitive coupling network to achieve less variation of coupling between resonators [28]. In general, the simplest capacitive or inductive coupling elements are frequency dependent ones and cannot satisfy the coupling coefficient required for a constant absolute bandwidth over a wide tuning range. Hence, more complicated coupling schemes such as Π- and L-capacitive coupling networks are suggested. The tunable filter design is based on an optimization method that finds out the desired values of capacitors and the electrical length. The fabricated filter and measured results are given in Figure 2-19. It can be seen that a Π-lumped capacitive network is employed for the input and output coupling network and the small bandwidth variation has been achieved.

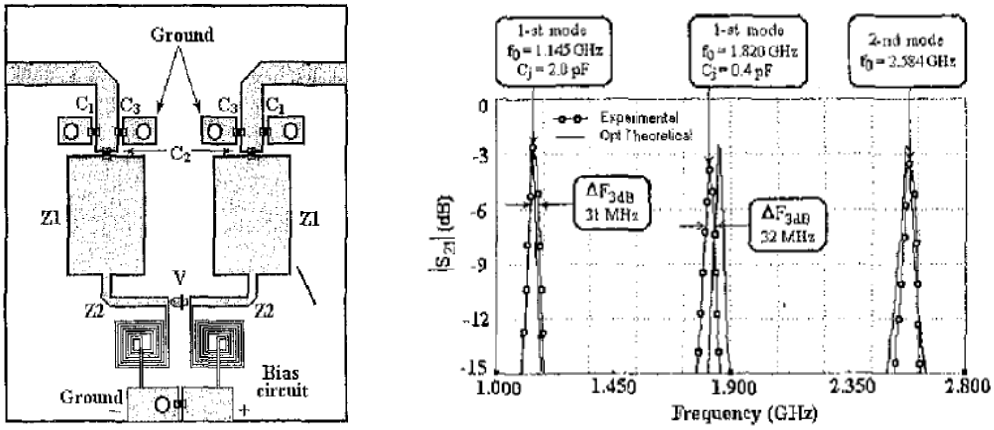


(a) (b)

Figure 2-19. (a) The fabricated circuit and (b) Experimental performance [28].

### *2.1.1.10 Reconfigurable filter based on switched delay line*

A completely new approach to realize tunable filter was introduced by Hunter [29]. The filter can be tuned in such way that simply chooses different phases between two parallel delay lines shown in Figure 2-20. The incident signal is split into two parallel delay lines and combined by a multi-pole switch for the output. By toggling the position of the output switches, the phase between the two parallel delay lines is

changed, resulting in the tuning of the resonant frequency of the filter. The reason behind this can be explained below.

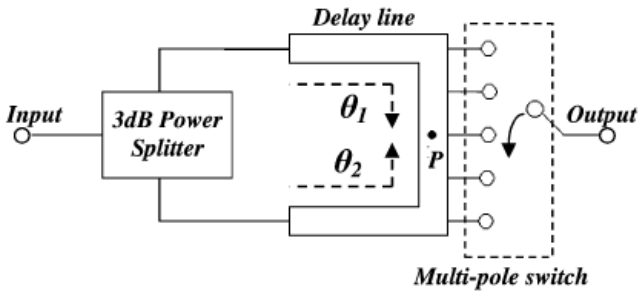


Figure 2-20. Switch delay-line resonator [29].

The voltage at the output point P is given by

$$V_p = \frac{V}{\sqrt{2}}\left(\frac{e^{-j\theta_1} + e^{-j\theta_2}}{2}\right) \qquad (2.14)$$

Therefore, $|V_p|$ is derived as

$$|V_p| = \frac{V}{\sqrt{2}}\cos\left(\frac{\theta}{2}\right), \qquad \theta = \theta_2 - \theta_1 \qquad (2.15)$$

The transfer function is given by (matching load assumed)

$$|S_{21}|^2 = \frac{\frac{|V_p|^2}{Z_0/2}}{\frac{V^2}{Z_0}} = \cos^2\left(\frac{\theta}{2}\right) \qquad (2.16)$$

The relative phase in the two paths can be expressed as

$$\theta = \frac{\pi\omega}{\omega_0} \qquad (2.17)$$

From (2.16)-(2.17), it is clear that the transmission response is entirely determined by the phase relationship between the parallel delay lines, which is demonstrated in Figure 2-21 with two states.

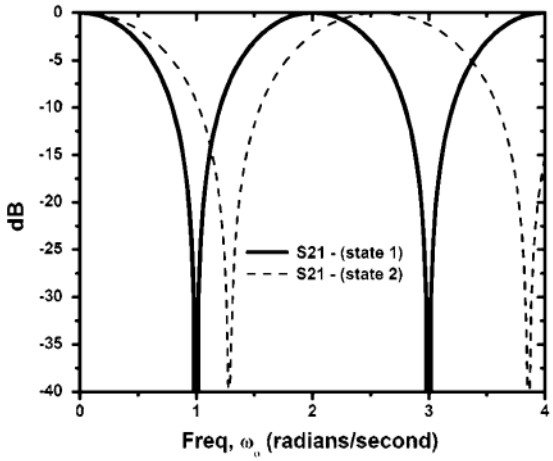


Figure 2-21. Transmission responses of switched delay-line resonator with toggled output switch at point P (solid line) or at position with 20 (degree) electrical length away from point P (dotted line) [29].

### *2.1.2 RF MEMS tunable (or reconfigurable) filters*

Radio frequency (RF) microelectromechanical systems (MEMS) switches and varactors have attracted more attentions in recent years due to their very low loss and high linearity over the varactors, especially for high frequency applications from 10GHz up to more than 100GHz [37]. Some typical MEMS tunable or reconfigurable filters are described as follows.

#### *2.1.2.1 Tunable filters using MEMS bridge varactors*

A MEMS bridge varactor has been introduced in tunable filter design [30] shown in Figure 2-22. The MEMS bridge varactors are fabricated at the height of 1.2 μm above the CPW center conductor on a glass substrate. The pull-down electrodes are fabricated using a 1000-Å-thick SiCr layer with a resistivity of 1-2KΩ/square. The MEMS varactors are loaded on half wave-length resonators to change the phase velocity of the

resonators, which is illustrated in Figure 2-23. By applying a pull-down bias voltage of 0-80V, the bridge height is adjusted so as to control the capacitance of the varactors. In order to compensate the increasingly capacitive behaviour of the resonators when they are tuned toward the lower frequencies, inductive inter-resonator coupling are utilized in the tunable filter design (see in Figure 2-23). The measured results are given in Figure 2-24, which shows good performance regarding to insertion loss at about 20GHz.

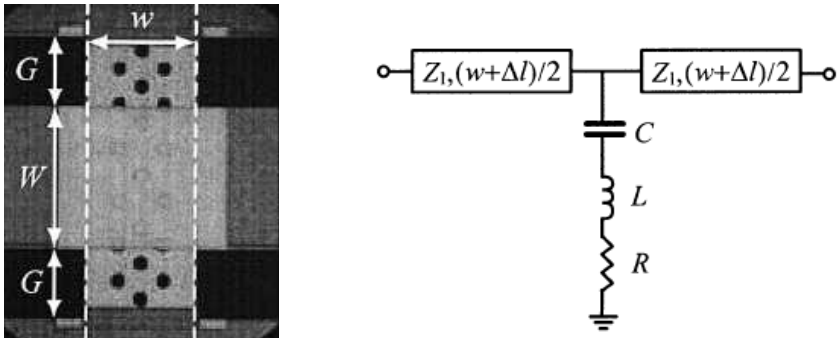


(a) (b)

Figure 2-22. MEMS varactor over a CPW line. (a) Photograph. (b) Circuit model [30].

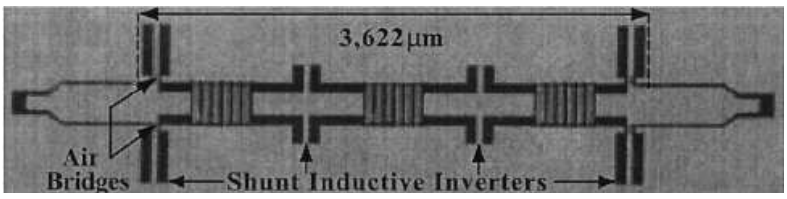


Figure 2-23. Layout of MEMS bridge varactor tunable filter (fix MEMS capacitors are replaced by MEMS varactors) [30].

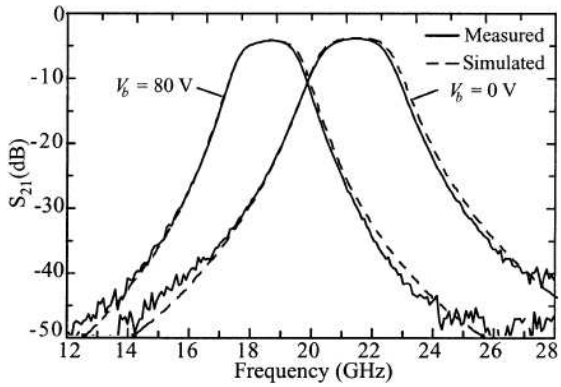


Figure 2-24. Measured and simulated results of the MEMS bridge varactor tunable filter [30].

### *2.1.2.2 Reconfigurable filters based on MEMS DC contact switches*

Pothier et al. introduced a reconfigurable filter topology employing MEMS DC/ohmic contact switches [31], which is presented in Figure 2-25(a).

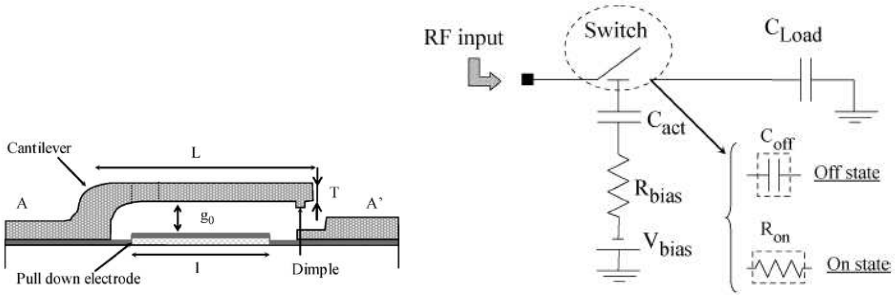


(a) (b)

Figure 2-25. (a) Side view of the MEMS switch. (b) Electrical equivalent circuit of a digital capacitive load to ground with its biasing network [31].

The switch is made of a 3.5-µm-think gold cantilever that is electrostatically actuated using a 120-µm-long actuation electrode. The small dimple is added under the cantilever just above the contact to reduce the contact resistance when it is in the on-state. By switching on or off the cantilever, the loading capacitance is changed, as can be seen in Figure 2-25(b). Very low insertion loss can be achieved with this type of MEMS DC contact switch as illustrated experimentally in Figure 2-26.

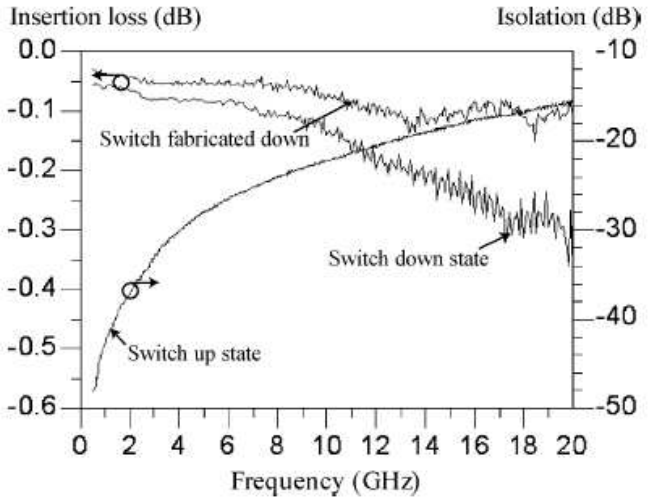


Figure 2-26. Measured isolation and insertion loss of the MEMS dc contact switch [31].

It can be seen that the insertion loss can be reached to 0.3 dB at 20 GHz in the on-state and a 38 dB of isolation at 2 GHz in the off-state. A two bit tunable filter has been demonstrated using the MEMS DC contact switches, which is displayed in Figure 2-27(a). In order to control coupling variation when the frequency is shifted, the two microstrip resonators are coupled by using their magnetic fields and the input-output coupling are adjusted by allocating the capacitive loads. The measured performance of the filter is given in Figure 2-27(b). The filter exhibits a low level of insertion loss (less than 3.2 dB) over a tuning range from 9.55 to 14.95 GHz.

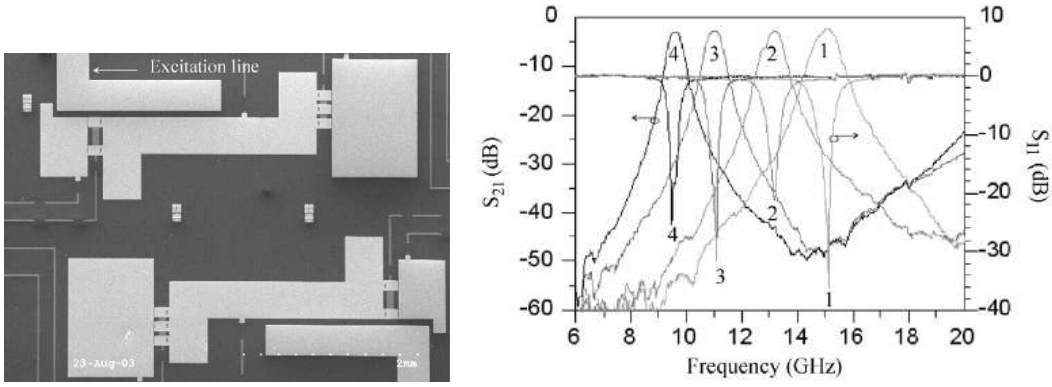


(a) (b)

Figure 2-27. (a) SEM photograph of the tunable filter. (b) Measured performance [31].

### *2.1.3 BST varactor tunable filters*

Thin-film ferroelectric materials, such as barium strontium titanate (BST) have been investigated for frequency agile applications because of their faster tuning speed than MEMS varactors and more linearity than semiconductor varactors. In the following, two types of newly developed BST varactor tunable filters are described.

#### *2.1.3.1 Tunable bandstop filter using BST varactors*

A newly developed tunable bandstop filter employing BST varactors was introduced by Chun et al. [42]. The BST varactor was constructed in an interdigital capacitor (IDC) configuration shown in Figure 2-28.

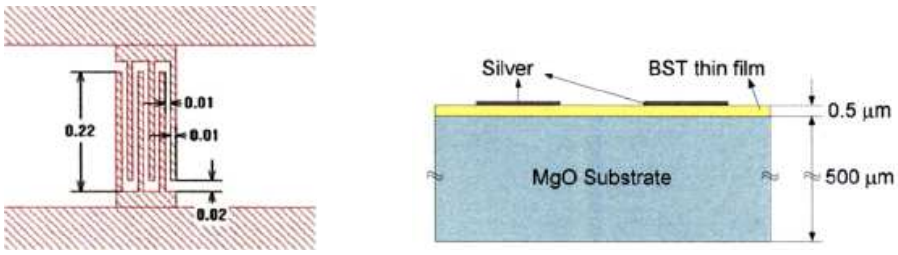


(a) (b)

Figure 2-28. (a) Layout of interdigital BST varactor cell. (b) Profile of layers [42].

The BST varactor is fabricated based on Mgo substrates with a 0.5-μm thick $Ba_{0.5}Sr_{0.5}Tio_3$ (BST) thin film deposited onto the surface by pulsed laser deposition, using a laser fluence of 1.5 $Jcm^{-2}$ at 5 Hz pulsed rate in the presence of an oxygen gas background [46]. The fabricated BST varactor exhibits a capacitive tunability of about 28.6% from 0.4 pF to 0.56 pF by applying a DC bias voltage from 35 V to 0 V, where the capacitive tunability is defined by

$$Capacitive\_Tunability = \frac{C_{\max} - C_{\min}}{C_{\max}} \times 100(\%) \qquad (2.18)$$

where $C_{\max}$ is the capacitance of BST varactor at 0 V bias, $C_{\min}$ denotes the capacitance obtained at a non-zero DC bias. Note that the capacitance $C_{\min}$ decreases as the DC bias voltage is increased. This is because the relative permittivity of BST material is reduced against the applied DC voltage [46]. By employing the BST varactors, a two-pole tunable bandstop filter with a slotted ground structure has been demonstrated and depicted in Figure 2-29(a) and its measured results are given in Figure 2-29(b).

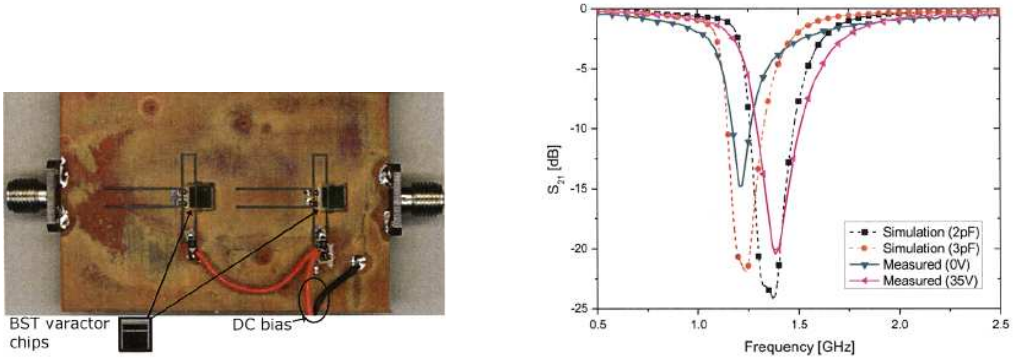


(a) (b)

Figure 2-29. (a) The fabricated BST varactor bandstop filter. (b) Measured performance [42].

It can be seen that the center frequency of the bandstop filter is shifted from 1.2 to 1.4 GHz by applying a DC bias voltage from 0 to 35 V.

### *2.1.3.2 Tunable combline filter employing BST varactors*

Nath et al. introduced a room-temperature third-order combline bandpass filter using thin-film BST interdigital capacitor (IDC) varactors as present in Figure 2-30 (a) [48]. The loading capacitors of the conventional combline filter are replaced by BST varactors. In order to achieve low insertion low, single-layer lithography on sapphire and copper metallization techniques are used for the fabrication of the BST IDC varactors shown in Figure 2-30(b). The length of the finger is 100 µm, the width is 5 µm and the spacing between the fingers was set to be 5 µm. By applying a DC bias voltage of 35 V at 1 MHz, the varactor shows a 12 % tuning and the Q factor of the varactor was found to be 100 at 0 V bias and increasing to 250 at 35 V bias, both measured at 1MHz, which is demonstrated in Figure 2-31.

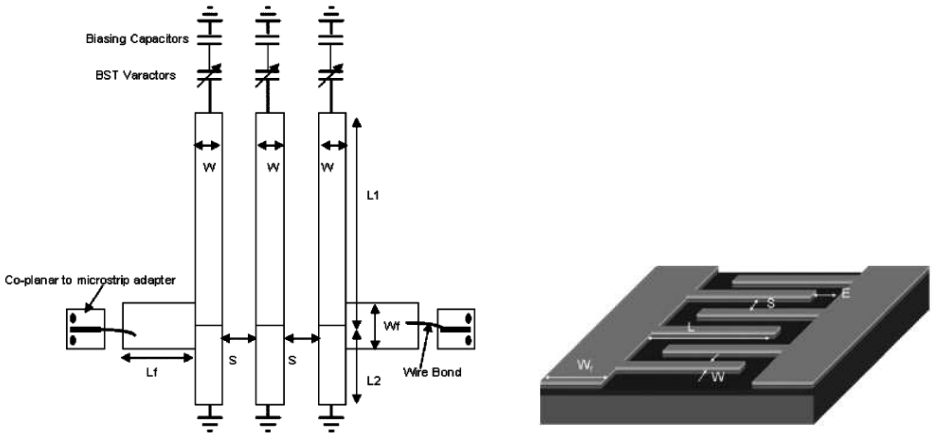


(a) (b)

Figure 2-30. (a) Schematic of the tunable combline bandpass filter. (b) Schematic of interdigital capacitor [48].

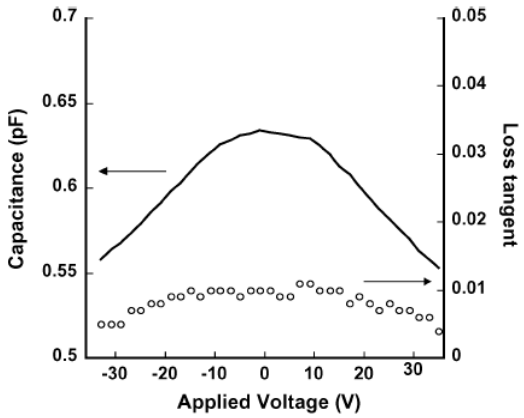


Figure 2-31. Nominal tuning curve of the BST IDC varactor at 1 MHz [48].

By employing the BST IDC varactors, a third-order tunable combline bandpass filter has been designed and fabricated, present in Figure 2-32(a). The measured performance is given in Figure 2-32(b). It can be seen that the filter was tuned from 2.44 to 2.88 GHz with the DC bias voltage varies from 0 to 200 V. The insertion loss is between 3 and 5 dB over the tuning range.

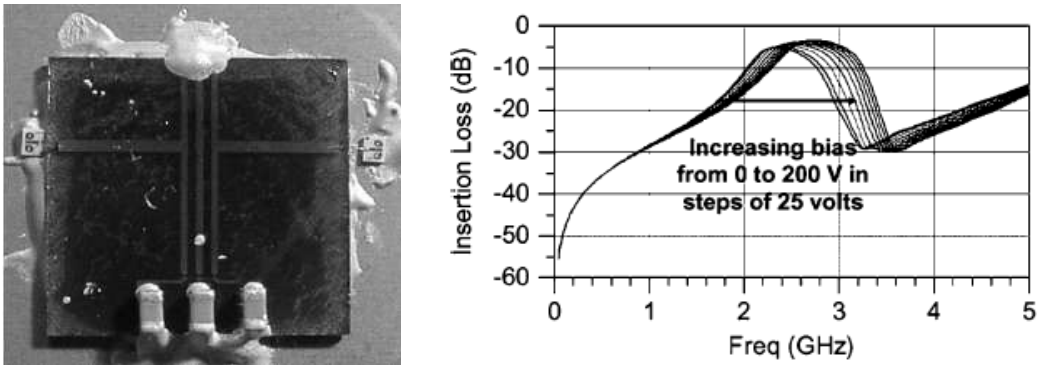


(a) (b)

Figure 2-32. (a) Assembled combline tunable filter using BST varactors. (b) Measured results [48].

### *2.1.4 Piezoelectric transducer tunable filters*

Piezoelectric transducers (PETs) have also been utilized as tuning elements in electronically tunable filter designs. As reported in [38], a PET and an attached

dielectric perturber has been employed to tune a cascaded microstrip open-loop resonator filter [49], which is illustrated in Figure 2-33.

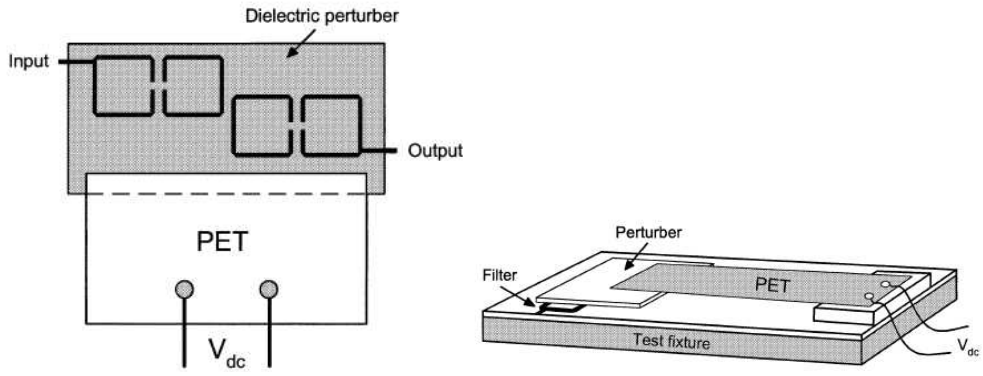


(a) (b)

Figure 2-33. Configuration of the piezoelectric transducer tunable bandpass filter. (a) Top view. (b) Three-dimension view [38].

The PET consists of two piezoelectric layers and one shim layer. The piezoelectric layer is a composition of lead, zirconate, and titanate. The center shim, laminated between the two same polarization piezoelectric layers, adds mechanical strength and stiffness. The shim is connected to one polarity of a DC voltage to deflect the PET and move it up or down vertically. In the mean time, the perturber attached to the PET moves up or down, the effective dielectric constant of the filter decreases or increases, respectively. In this way, both center frequency and inter coupling between resonators can be varied, resulting in a constant absolute bandwidth response as displayed in Figure 2-34.

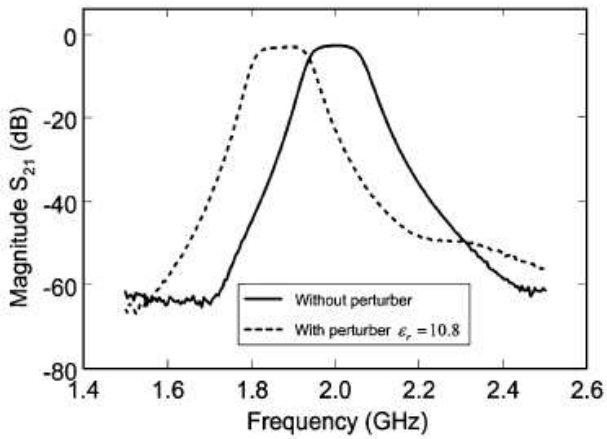


Figure 2-34. Measured results of the tunable bandpass filter using piezoelectric transducer [38].

### *2.1.5 Novel electrically dual-mode tunable filters*

Traditionally, controlling the inter-couplings between resonators is the key condition for a tunable filter to maintain constant absolute bandwidth over a wide tuning range. Many techniques have been addressed above to control the inter-couplings between resonators. In difference, a new type of dual-mode resonator filters have been developed [9]-[10], in which the dual modes do not couple to each other. This leads to a simple tuning scheme because tuning the passband frequency is accomplished by merely changing the two modal frequencies proportionally. Based on this unique characteristic, some tunable filters have been developed and described as follows.

#### *2.1.5.1 Electronically reconfigurable filter based on dual-mode open-loop resonators*

A new type of reconfigurable asymmetric frequency response bandpass filter using dual-mode open-loop resonator was introduced by Chun et al. [11], which is shown in Figure 2-35(a).

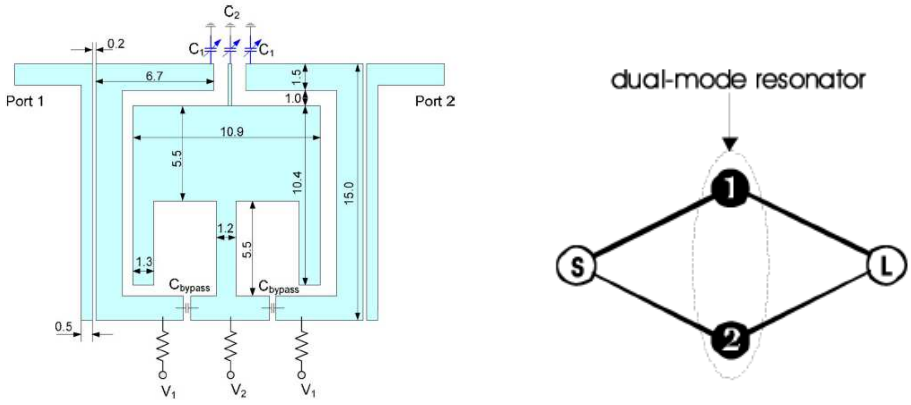


(a) (b)

Figure 2-35. (a) Layout of a reconfigurable dual-mode microstrip open-loop resonator bandpass filter. (b) The coupling scheme [11].

The coupling scheme of the dual-mode filter is given in Figure 2-35(b). It is clear that there is no coupling between the two operating resonant modes. The center frequency of the passband can be tuned if the resonant frequencies of the odd-mode and even-mode are shifted proportionally. In addition, for a filter of this type, its selectivity can be

electronically reconfigurated to exhibit a higher selectivity with a finite frequency transmission zero on either side of the passband. Three varactors (Infineon BB857) are implemented for electronic tuning. To reconfigurated the filter characteristic, two DC biases are employed. The first DC bias V1 is used to change the odd-mode resonant frequency while the second DC bias V2 is used to vary the even-mode resonant frequency. The measured performance is given in Figure 2-36. It can be seen that, depending on the combinations of the two DC biases, not only the passband frequency can be tuned, but the filtering characteristic can be reconfigurated from the high selectivity on the high side of the passband for Case 1 to the high selectivity on the low side of the passband for Case 2.

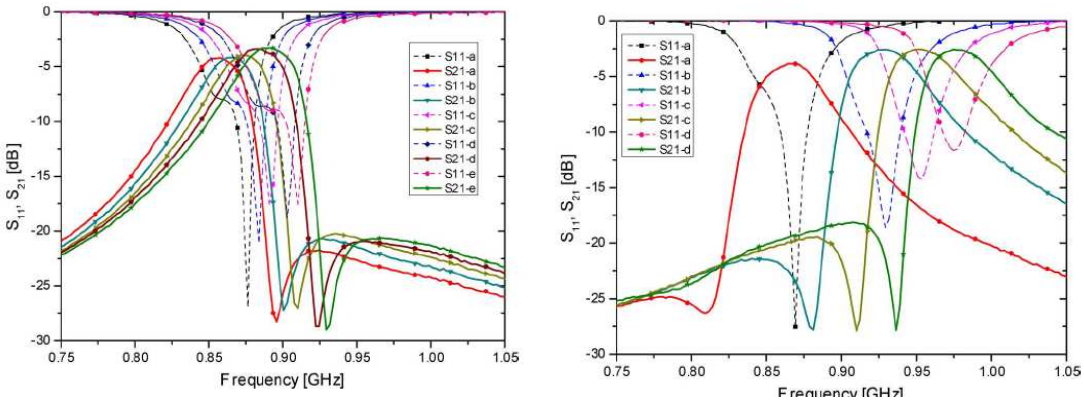


(a) (b)

Figure 2-36. Measured performance of the reconfigurable dual-mode filter using two DC biases. (a) Case 1. (b) Case 2 [11].

### *2.1.5.2 Tunable filter based on doublet configuration*

Liao et al. reported a tunable filter using an E-shaped dual-mode resonator [12]. The layout of the tunable dual-mode filter is presented in Figure 2-37(a). The coupling scheme of the doublet configuration filter is shown in Figure 2-37(b). Varactor C1 is used to vary even mode resonant frequency and varactor C2 is employed to change odd mode resonant frequency. Since the odd mode and even mode are uncoupled degenerate modes, this leads to an improved filter reconfigurability because the center frequency and the bandwidth can be changed independently. Thus, it is possible to achieve a constant absolute bandwidth over a relative wide tuning range by properly choosing the

values of C1 and C2. Varactor diodes of model SMV1233-011L manufactured by Skywalks were used to electronically change C1 and C2. Two DC bias voltages are deployed to tune the filter, one to control C1 and another to control C2.

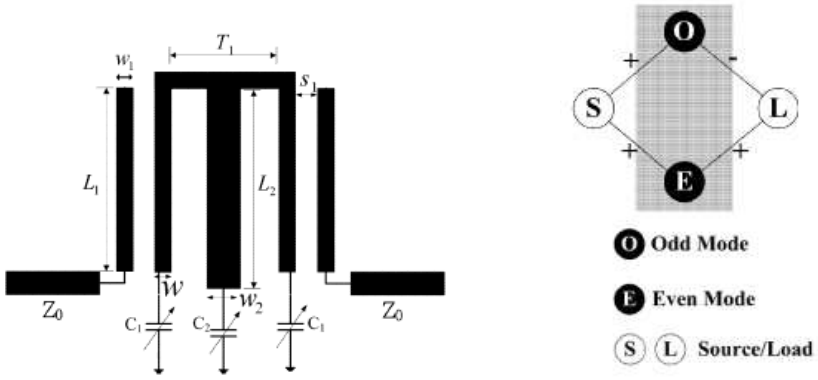


(a) (b)

Figure 2-37. (a) Tunable dual-mode filter using a single triangular patch resonator with varactors across the slots. (b) Coupling scheme [12].

Measured filter responses are plotted in Figure 2-38, which shows that constant absolute bandwidth can be achieved over a tuning range from 1.06 to 1.12 GHz with the finite frequency transmission zero reconfigurated on either side of the passband.

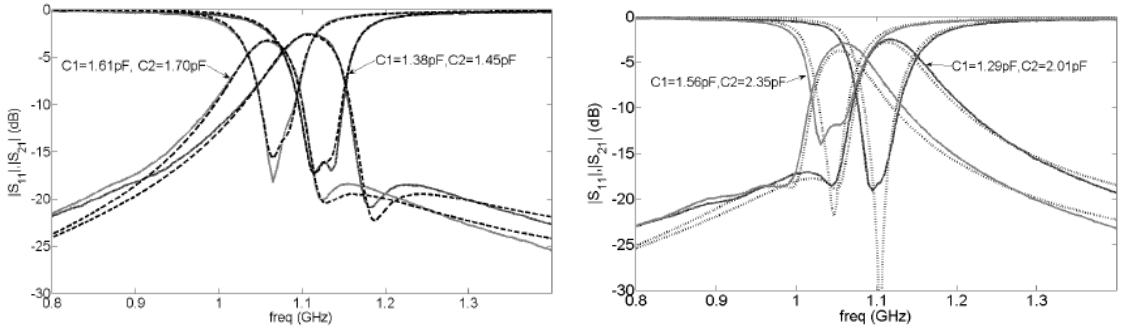


(a) (b)

Figure 2-38. Measured results. (a) One transmission zero on the upper side. (b) One transmission zero on the lower side [12].

### *2.1.6 Summary*

In order to achieve a constant absolute bandwidth for a tunable filter over a broad tuning range, many techniques have been investigated such as using step-impedance combline structure, corrugated coupled lines, self-scalable combline structure, independent electric and magnetic coupling scheme, mixed electric and magnetic coupling scheme, π and L-capacitive coupling scheme. The main idea behind these techniques is to control the portion of electric coupling to magnetic coupling over the tuning range. Moreover, for a wider bandwidth variation control, variable coupling reducer and lumped-distributed coupling lines are used to adjust the inter-coupling between resonators effectively.

Tunable or reconfigurable filters using Semiconductors, MEMS switches, piezoelectric transducers, and BST thin-film materials have also been demonstrated. In which, novel topologies and manufacture techniques were employed. Table 2-1 gives the comparison of these tuning device technologies [50].

**TABLE 2-1**

**Comparison of tuning device technologies [50].**

| Tuning Technology | Tuning Speed | Q or Rs at 10GHz | Bias | Power Consumption | Linearity |
|---|---|---|---|---|---|
| Semiconductor p-i-n diode | ns | Rs ≈ 1-4 Ω | 10-30 mA | High | High |
| Semiconductor varactor | ns | Q ≈ 30-40 | < 30 V | Low | Low |
| MEMS | μs | Q ≈ 50-400 | 30-90 V | negligible | High |
| Ferroelectric thin-film | ns | Q ≈ 30-150 | < 30 V | negligible | Moderate |
| Piezoelectric transducer | > 100 μs | Q > 500 | > 100 V | negligible | High |

## 2.2 Microstrip Dual-Mode Filters

Microstrip dual-mode filters are of interest for applications in RF/microwave circuits and systems because each of dual-mode resonators can be used as a doubly tuned resonant circuit, and therefore the number of resonators required for a given degree of filter is reduced by half, resulting in a compact filter configuration [1]. Several types of dual-mode microstrip resonators have been demonstrated including the circular ring [4], the square loop [5], the circular dick and the square patch [51]-[52]. The dual-mode microstrip triangular patch or loop resonators and filters have also been reported [53]-[54]. In addition, a new type of dual-mode resonators and filters has been introduced [9]-[10], which has a different coupling scheme comparing to the conventional ones. Some typical dual-mode filters are described as follows.

### *2.2.1 Dual-mode filter using microstrip square patch*

A microstrip square patch dual-mode resonator filter has been investigated in [1], [51]. The microstrip square patch resonator can be represented by a wheeler's cavity model [55], as shown in Figure 2-39.

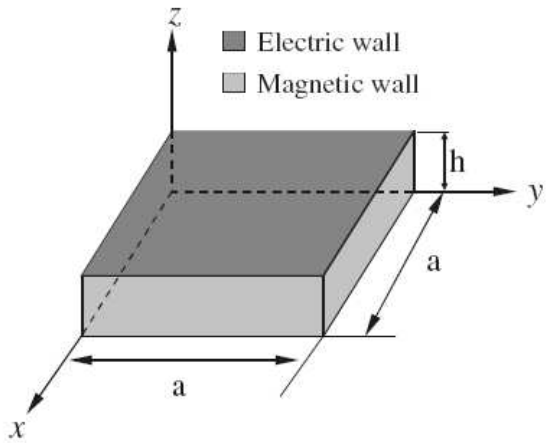


Figure 2-39. Cavity model of a dual-mode microstrip resonator [1].

where the top and bottom of the cavity are perfect electric walls and the remaining sides are the perfect magnetic walls. The EM fields inside the cavity can be given in terms of $TM^{z}_{mn0}$ modes:

$$E_z = \sum_{m=0}^{\infty}\sum_{n=0}^{\infty} A_{mn}\cos(\frac{m\pi}{a}x)\cos(\frac{n\pi}{a}y)$$

$$H_x = (\frac{j\omega\varepsilon_{eff}}{k_c^2})(\frac{\partial E_z}{\partial y}),\ H_y = -(\frac{j\omega\varepsilon_{eff}}{k_c^2})(\frac{\partial E_z}{\partial x}) \qquad (2.19)$$

$$k_c^2 = (\frac{m\pi}{a})^2 + (\frac{n\pi}{a})^2$$

where $A_{mn}$ denotes the mode amplitude, $\omega$ is the angular frequency, and a and $\varepsilon_{eff}$ are the effective width and permittivity [55]. The resonant frequency of the cavity is given by

$$f_{mn0} = \frac{1}{2\pi\sqrt{\mu\varepsilon_{eff}}}\sqrt{(\frac{m\pi}{a})^2 + (\frac{n\pi}{a})^2} \qquad (2.20)$$

A pair of degenerate modes, which have the same resonant frequency, can be $TM^z_{100}$ and $TM^z_{010}$ modes. These two modes are orthogonal to each other and have the same resonant frequency as indicated in Figure 2-40.

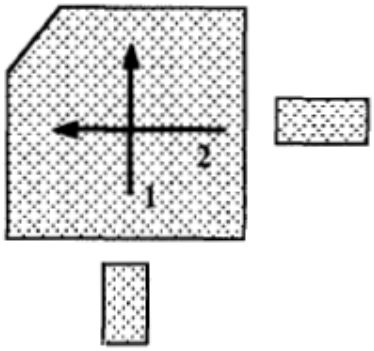


Figure 2-40. Dual-mode square patch resonator [51]. (The arrows represent the orthogonal modes within the resonator).

In order to couple them, a small perturbation has been applied at a location that is assumed at a 45˚ offset from its two orthogonal modes. The coupling coefficient of the two orthogonal modes is depending of the size of perturbation. Thus, by properly choosing the size of the perturbation and the input/output coupling, a dual-mode filter can be realized. Figure 2-41(a) presents a fabricated two-pole dual-mode square patch resonator microstrip filter, and the measured results are given in Figure 2-41(b).

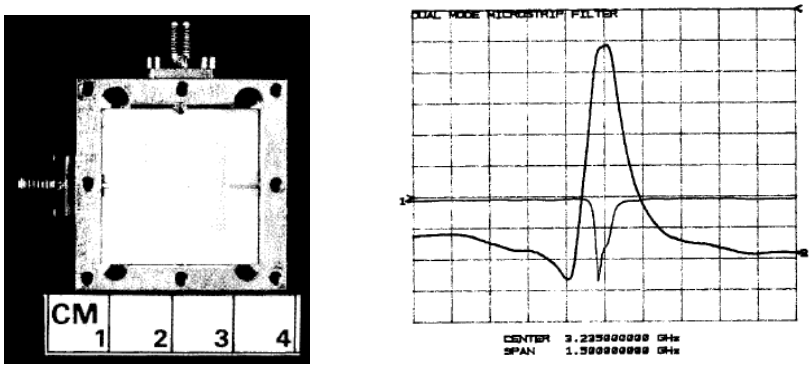


(a) (b)

Figure 2-41. (a) Fabricated dual-mode square patch resonator microstrip filter. (b) measured performance [51].

### *2.2.2 Dual-mode filter employing microstrip ring resonator*

Degenerate modes of a microstrip ring resonator have been used in dual-mode filter design as reported by Wolff [4]. The ring resonator is excited by symmetrical coupling lines. Under this condition, only one of the degenerate modes will be excited. Both modes are orthogonal to each other, hence, no coupling occurs between the two modes. The two modes can be considered as two waves that travel clockwise and anti-clockwise on the microstrip ring resonator. In order to split the two degenerate modes, two methods can be employed. The first method is to couple the ring resonator asymmetrically shown in Figure 2-42. By varying the asymmetrical angle, the mode split can be obtained. The second way of exciting the two degenerate modes is to couple the ring resonator symmetrically and to use a small perturbation located at 45˚ offset from the axis of coupling lines, which is illustrated in Figure 2-43(a). The degree of coupling modes depends on the size of the disturb as can be seen in Figure 2-43(b).

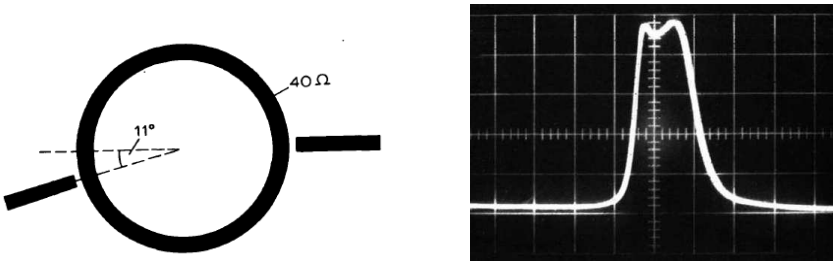


(a) (b)

Figure 2-42. (a) Asymmetrically coupled microstrip ring resonator. (b) Measured performance [4].

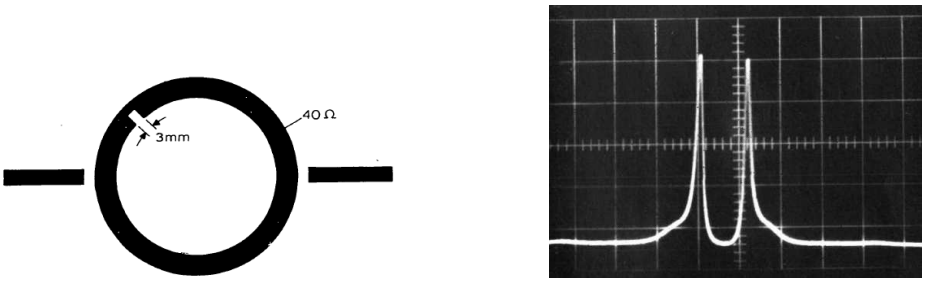


(a) (b)

Figure 2-43. (a) Microstrip ring resonator disturbed by a notch. (b) Measured results [4].

### *2.2.3 Dual-mode filter based on microstrip triangular patch resonator*

Hong et al. introduced a new type of dual-mode filters by using triangular patch resonators [9]. In distinct to conventional dual-mode resonators, e.g., the square patch dual-mode resonators and dual-mode ring resonator, the dual modes do not couple to each other. The dual modes can result from the rotation and superposition of a fundamental mode. By employing a wheeler's cavity mode, the electromagnetic (EM) fields inside the triangular cavity can be expanded in terms of $TM^{z}_{m,n,l}$ modes [56] given by

$$\begin{aligned} E_z(x,y) = A_{m,n,l}\{&\cos[(\frac{2\pi x}{\sqrt{3}a}+\frac{2\pi}{3})l]\cos[\frac{2\pi(m-n)y}{3a}] \\ &+\cos[(\frac{2\pi x}{\sqrt{3}a}+\frac{2\pi}{3})m]\cos[\frac{2\pi(n-l)y}{3a}] \\ &+\cos[(\frac{2\pi x}{\sqrt{3}a}+\frac{2\pi}{3})n]\cos[\frac{2\pi(l-m)y}{3a}]\} \end{aligned}$$

$$H_x=(\frac{j}{\omega\mu_0})(\frac{\partial E_z}{\partial y}),\quad H_y=(\frac{-j}{\omega\mu_0})(\frac{\partial E_z}{\partial x}) \tag{2.20}$$

where $A_{m,n,l}$ is a constant and a is the length of the triangle side. A fundamental mode, which can be found from (2.20) is the $TM^{z}_{1,0,-1}$ mode given by

$$E_z(x,y) = A_{1,0,-1}\{2\cos(\frac{2\pi x}{\sqrt{3}a} + \frac{2\pi}{3})\cos(\frac{2\pi y}{3a}) + \cos(\frac{4\pi y}{3a})]\} \qquad (2.21)$$

To rotate the fundamental mode, the coordinate system id rotated by $\alpha = 2\pi/3$ and $\beta = -2\pi/3$ as displayed in Figure 2-44.

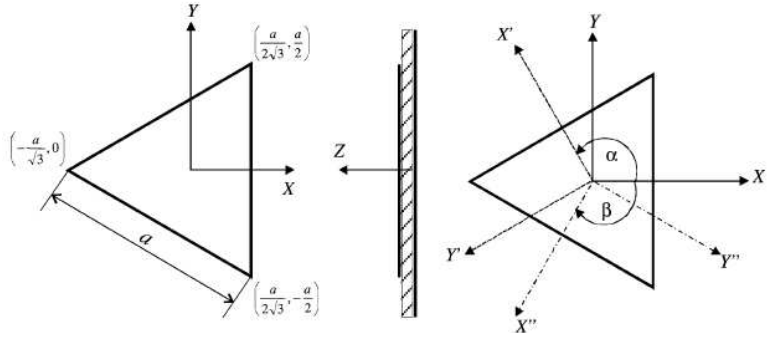


(a) (b)

Figure 2-44. (a) Equilateral triangular microstrip patch geometry. (b) Rotated coordinate system [9].

By superposition the fundamental mode and the rotated fundamental mode, a pair of fundamental degenerate modes can be found as illustrated in Figure 2-45.

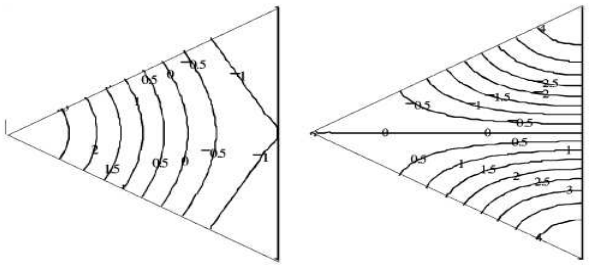

(a) (b)

Figure 2-45. Electric-field patterns of the degenerate modes. (a) Mode 1. (b) Mode 2[9].

As can be seen, with respect to the horizontal symmetric place, modes 1 and 2 behave as an even and odd mode, respectively. The mode splitting can be achieved by introducing a small cut or a narrow slit along its symmetric axis shown in Figure 2-47.

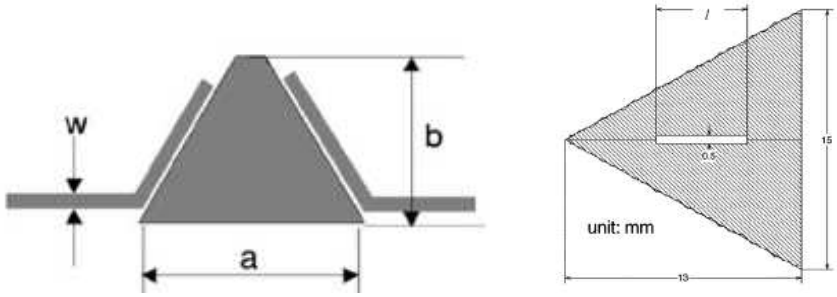


(a) (b)

Figure 2-46. Dual-mode microstrip triangular patch resonator with (a) a small cut and (b) a narrow slit [9].

It is also found that the split-mode frequencies are equal to the two self-resonant frequencies by using a magnetic or electric wall along the symmetrical axes, respectively. The results performed by full-wave EM simulation are given in Figure 2-47. It is evident that the two modes are hardly coupled to each other for the mode perturbations introduced.

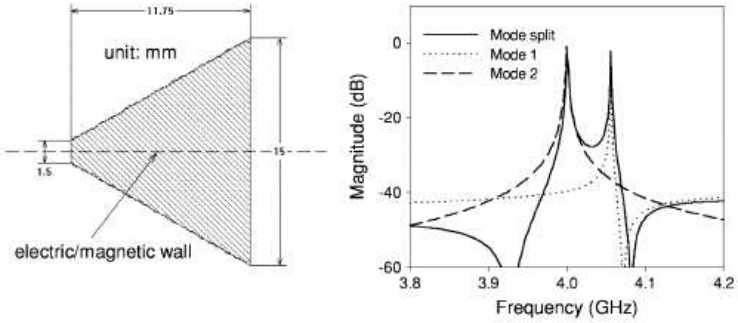


(a) (b)

Figure 2-47. Simulated split-mode frequencies (full-line) and self-resonant frequencies (dotted line for mode 1 and dashed line for mode 2) for a perturbed (small cut) dual-mode triangular microstrip resonator. (a) Layout. (b) Simulated results [9].

### *2.2.4 Dual-mode filters employing microstrip open-loop resonators*

A miniature dual-mode microstrip open-loop resonator has been investigated [10], which layout is displayed in Figure 2-48.

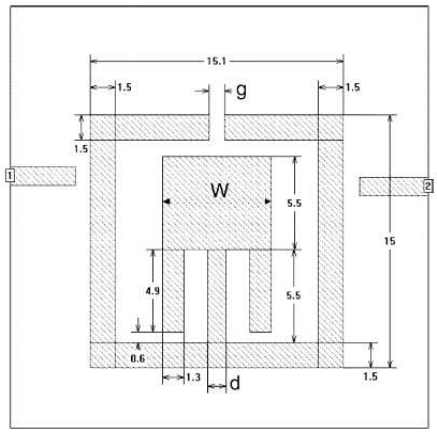


Figure 2-48. Layout of a dual-mode microstrip open-loop resonator [10].

A loading element with a variable parameter W is tapped from inside onto the open loop. The modal resonant characteristic is changed when W varies. Figure 2-49 gives the frequency response of the dual-mode open-loop resonator.

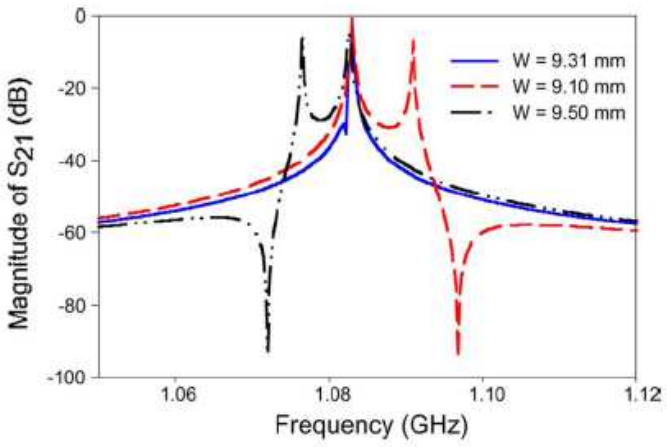


Figure 2-49. Modal resonant characteristic of the dual-mode open-loop resonator [10].

It can be seen that one modal resonant frequency is varied against the parameter W, while the other one is hardly changed. The charge distribution of the two modes is depicted in Figure 2-50 by using full-wave EM simulation.

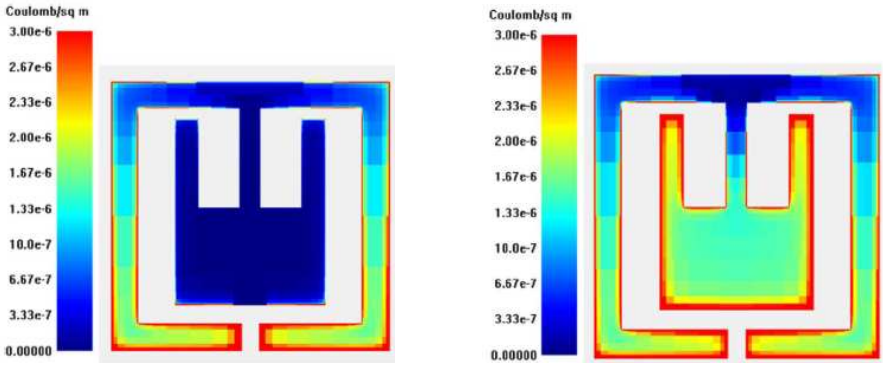


(a) (b)

Figure 2-50. Charge distribution. (a) Odd mode. (b) Even mode [10].

It is evident that the tapping point of the loading element is actually a virtual ground for the odd mode, hence, the loading element does not affect the odd-mode resonant frequency. It is also found that the two operating modes do not couple as the two split-mode frequencies are equal to the two self-resonant frequencies, respectively. Based on the dual-mode open-loop resonator, a two-pole dual-mode filter has been developed as given in Figure 2-51 with the measured performance. Notice that the finite-frequency transmission zero is closely associated with the even mode, which means the location of the finite-frequency transmission zero can be controlled by varying the even modal resonant frequency, resulting in a reconfigurable characteristic of the dual-mode filter.

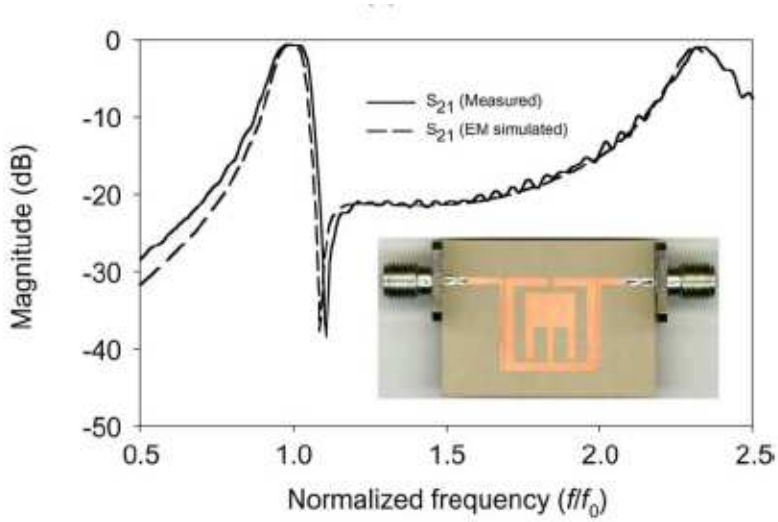


Figure 2-51. Measured and simulated frequency response of dual-mode filter. (the inset shows a photograph of the fabricated filter) [10].

### *2.2.5 Summary*

Several types of dual-mode resonators have been addressed. By introducing a perturbation to a single mode resonator at 45˚ offset from the two orthogonal modes, the coupling between two degenerate modes can be achieved, and the degree of the coupling can be controlled by changing the perturbation parameters. Asymmetric coupling method was also introduced to excite the two coupled degenerate modes for a ring resonator. A new type of dual-mode resonators has been investigated, in which the two degenerate modes do not couple due to an orthogonal nature of their fields or a cancellation of their electric and magnetic couplings.

## 2.3 Dual-Band Filters

Recent development in wireless communication and radar systems has presented new challenges to design and produce high-quality miniature components with a dual-band operation. For example, RF integrated transceivers are required for both global system for mobile communications (GSM) and wireless code-division multiple-access (WCDMA) operations [57]-[58], and dual-band antennas are designed for receiving signal at 0.9/1.8 GHz and at 2.4/5.2 GHz [59]-[60]. This has stimulated the development of many different types of dual-band filters [13]-[16], [61]-[68]. When the two operation bands are close to each other, transmission zero (s) can be introduced to realize two separated sub-bands for dual-band operation [61]-[63]. Microstrip dual-band filters operating at the two resonant modes of the stepped impedance resonators have been demonstrated [65]. Dual-band filters can also be realized using the stub line [67], folded waveguide [68], and dual-mode waveguide [16]. Two types of dual-band filters are addressed below.

### *2.3.1 Dual-band filter using vertical-stacked stepped impedance resonator (SIR)*

A vertical-stacked stepped impedance resonator has been employed to realize dual-band filter as reported in [65]. By using a stepped impedance resonator (SIR), both the fundamental and the second resonant frequencies can be easily adjusted over a broad frequency range. Figure 2-52(a) gives a SIR structure with input/output tapping.

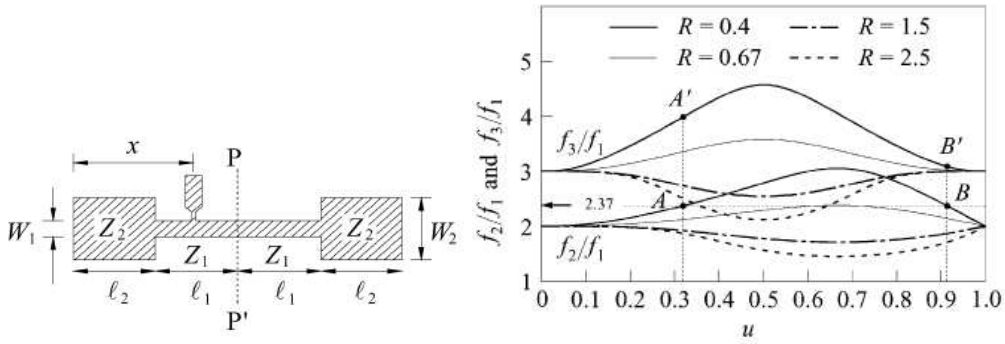


(a) (b)

Figure 2-52. (a) SIR with input/output tapping. (b) Normalized $f_2 / f_1$ and $f_3 / f_1$ for an SIR with impedance ratios R=0.4, 0.67, 1.5 and 2.5, $u = \theta_2 /(\theta_1 + \theta_2)$ [65].

The resonant frequencies can be derived by

$$\tan\theta_1 = R\cot\theta_2 \qquad \text{odd mode} \qquad (2.22)$$

$$\cot\theta_1 = -R\cot\theta_2 \qquad \text{even mode} \qquad (2.23)$$

where $\theta_1$ and $\theta_2$ are electrical length of the microstrip sections with characteristic impedance $Z_1$ and $Z_2$, respectively, and $R = Z_2 / Z_1$ is the impedance ratio of the SIR. The second ( $f_2$ ) and third ( $f_3$ ) resonant frequencies normalized with respect to the first one ( $f_1$ ) for different R are plotted in Figure 2-52(b), which shows that by varying the ratio of the SIR, the resonant frequencies of different modes can be controlled to realize dual bands operation. The coupling coefficients required for the two operating passbands can be obtained by changing the length ( $l$ ) and gap ( $d$ ) between the SIRs, shown in Figure 2-53. Which indicates there are two degrees of freedom in designing a coupled stage, thus, it is possible to make a coupled stage match the two coefficients required by specifications of the two passbands. The external $Q_e$ required for the two passband can be obtained by adjusting the location of the tap position as indicated in Figure 2-52(a). Fabricated circuit and measured results are given in Figure 2-54. It can be seen that by using vertical-stacked stepped impedance resonators, a miniature dual-band filter can be developed.

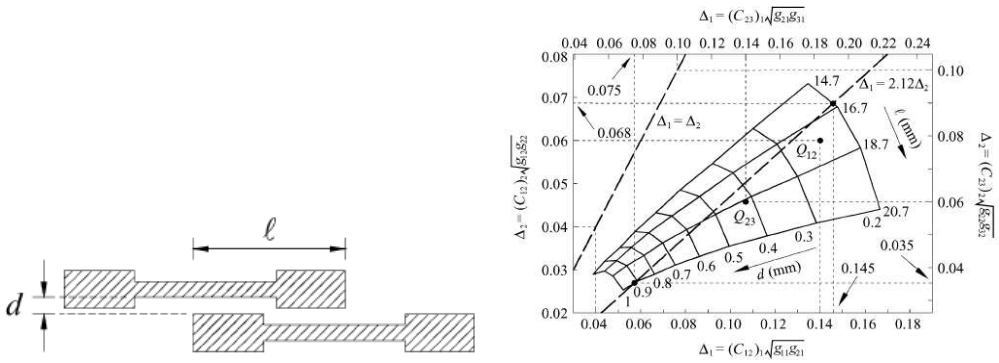


(a) (b)

Figure 2-53. (a) Coupling structure. (b) Fractional bandwidth design graph [65].

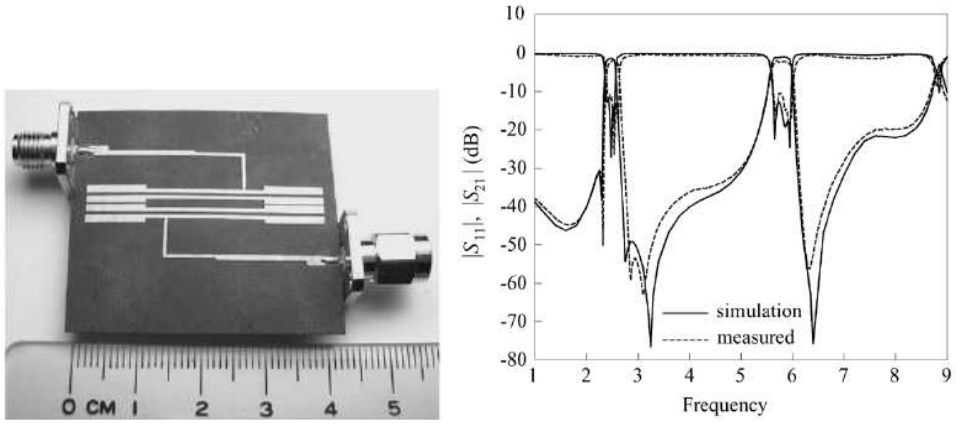


(a) (b)

Figure 2-54. (a) Photograph of the vertical-stacked SIR dual-band filter. (b) Measured performance [65].

### *2.3.2 Dual-band filter using stub-loaded open-loop resonators*

Mondal et al. introduced a new type dual-band filter by employing stub-loaded open-loop resonators [67], which is illustrated in Figure 2-55(a). As can be seen, a shunt open stub is loaded onto a conventional open-loop resonator. The mode positions are depended on the electrical length $\theta_1$ and $\theta_s$ shown in Figure 2-55(b). Thus, dual-band filters having passbands at two desired frequencies can be realized using this stub loaded open-loop resonator.

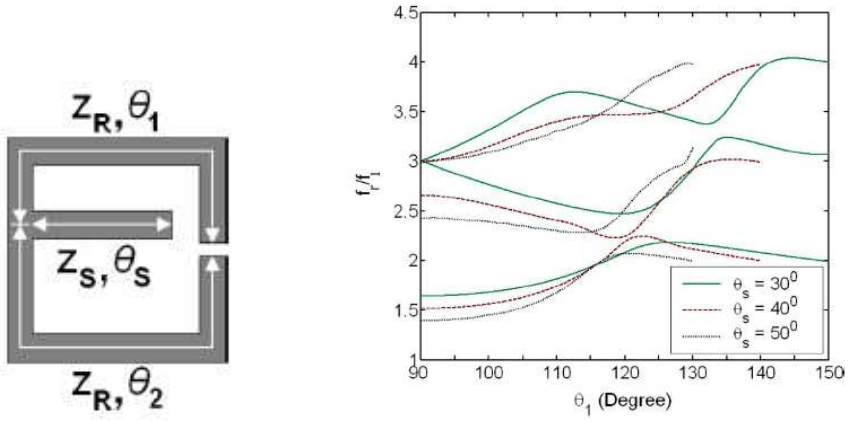


(a) (b)

Figure 2-55. (a) Stub loaded open-loop resonator. (b) Higher order resonance $f_r$ with respect to $f_1$ for three different stub lengths [67].

The coupling coefficients at the dual band frequencies can be specified by choosing different coupling schemes, i.e., electric, magnetic, and mixed coupling, because these coupling schemes can result in different ratios of coupling coefficients at the dual band frequencies., which is shown in Figure 2-56.

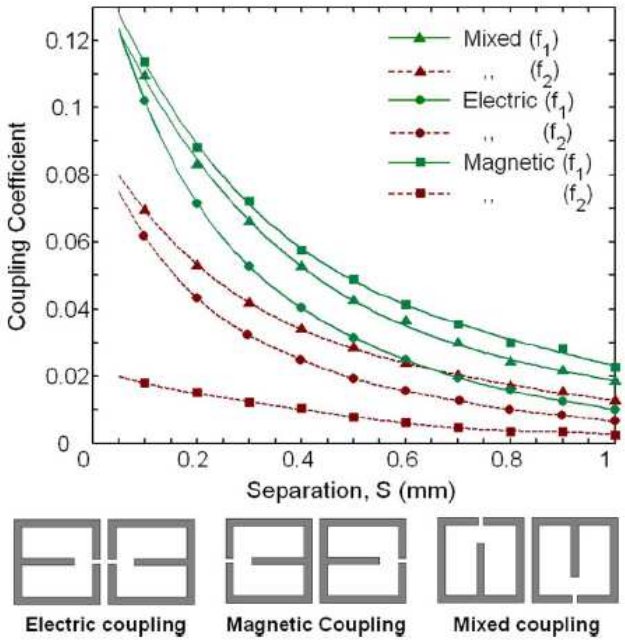


Figure 2-56. Variation of coupling coefficient with separation between the resonators. $f_1 = 2.8$ and $f_2 = 4.4$ GHz [67].

The external $Q_e$ required for the dual bands can be obtained by tuning the tapping position and the characteristic impedances of the stub, as depicted in Figure 2-57.

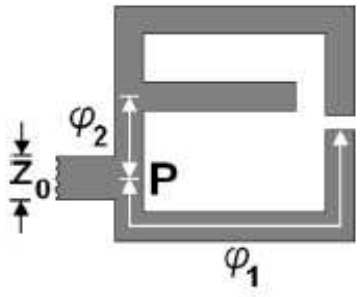


Figure 2-57. Stub-loaded open-loop resonator with tapped-line feeding [67].

### *2.3.3 Summary*

Two types of dual-band filters have been addressed. By properly choosing the parameters of coupling sections or using different coupling scheme, the coupling coefficients required for the two desired pass bands can be derived. In addition, the external $Q_e$ for the dual-band specifications can also be determined by adjusting the position of the tapped line of the input/output coupling. Miniature of the dual-band filters can be achieved by using vertical-stacked configuration or square open-loop resonators.

## 2.4 Bandstop or Notch Filters with Wide Spurious Free Passbands

Planar bandstop or notch filters are useful for RF/microwave applications [1]. In particular, narrow-band band-reject or notch filters have become more and more important in most microwave communications and radar systems as there exist more unwanted signals or interference at air interfaces. This has stimulated new developments of microstrip band reject filters [70]-[73]. Usually, transmission line bandstop filters comprised of distributed resonators would have encountered a restriction on the extent of the upper passband because of spurious response [47]. Recent efforts have been made to overcome this restriction using new design techniques [17]-[18], in which a

capacitive-loading technique and compound resonators technique are employed. These techniques will be addressed below.

### *2.4.1 Bandstop filter based on capacitive-loading technique*

A parallel-coupled line bandstop filter was introduced displaying a spurious-free passband region up to more than four times the stopband center frequency by loading capacitive elements to the coupled line [17], which is shown in Figure 2-58(a). In order to move the first spurious mode to higher frequency, approximately 45˚ long coupled lines instead of 90˚ long coupled lines in conventional design [47] are employed. The capacitive elements then are loaded to compensate the short coupled lines to provide the bandstop response. The simulated performance of the bandstop filter is displayed in Figure 2-58(b), which shows that a wide spurious-free passband was achieved.

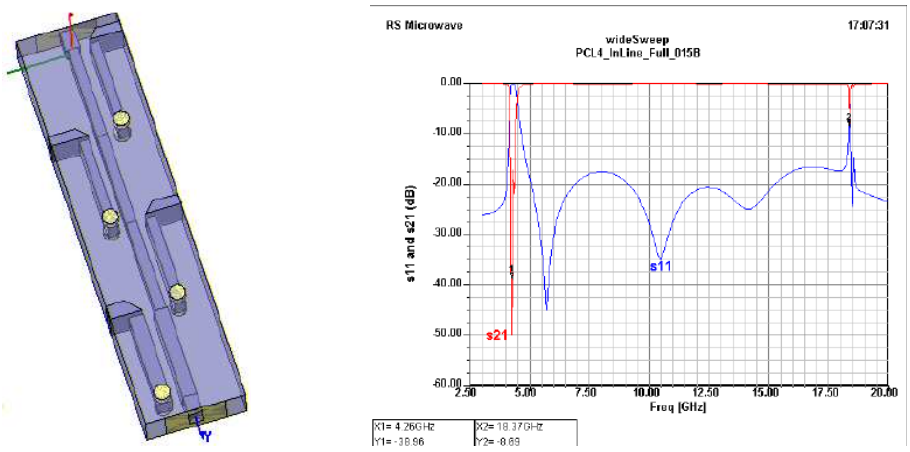


(a) (b)

Figure 2-58. (a) Layout of the bandstop filter using capacitive loading elements (yellow colour ones). (b) Simulated performance [17].

### *2.4.2 Bandstop filter using compound resonators*

Levy et al. introduced a new type of bandstop filters with the use of compound resonators having shorter electrical length to obtain extended upper passbands [18]. The new bandstop filter prototype circuit is depicted in Figure 2-59.

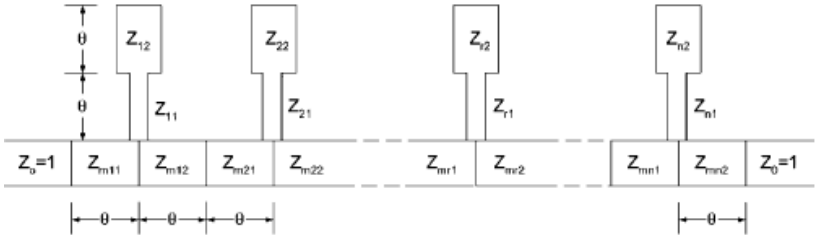


Figure 2-59. New commensurate bandstop filter [18].

The "compound" stub is consisting of a unit element having a relatively high impedance $Z_{r1}$ and a lower impedance open-circuited stub of impedance $Z_{r2}$. The ratio of the center frequency of the first spurious to the fundamental resonant frequency is $(180-\theta_r)/\theta_r$. Thus, when $\theta_r$ is 45˚, this ratio is 3, but when $\theta_r$ is less, the ratio increases, i.e., if $\theta_r$ is 25.7˚, the ratio increases to 6. Therefore, the upper passbands can be extended. Notice that the impedance matching can be done by varying the impedances of the main lines, i.e., the $Z_{mri}$ and the impedance of the stubs, i.e., the $Z_{r1}$ of the compound stubs shown in Figure 2-59.

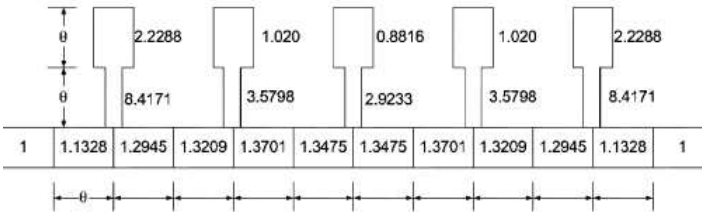


(a)

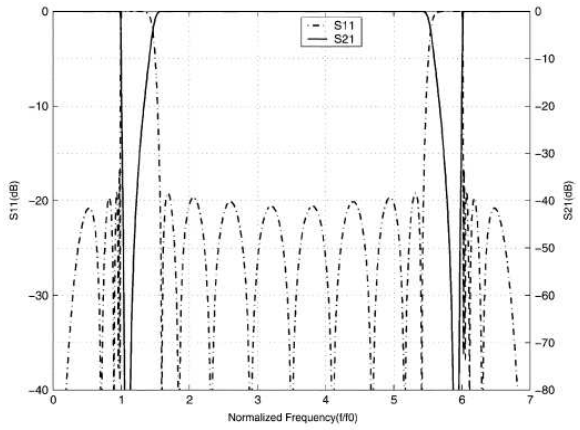


(b)

Figure 2-60. (a) Optimized chebyshev filter. ($\theta_r$ =25.7 degree) (b) Performance of the filter [18].

The layout of the optimized chebyshev filter is displayed in Figure 2-60(a), and the frequency response is depicted in Figure 2-60(b). It can be seen that the upper passband width were extended up to six times the fundamental bandstop center frequency with good impedance matching obtained.

### *2.4.3 Summary*

In order to extend the upper passband bandwidth of a bandstop filter, capacitive-loading technique and compound resonators technique have been investigated. By allowing capacitive elements loaded to parallel coupled lines, the electrical length of the parallel coupled lines becomes shorter, resulting in a higher first spurious response. Compound resonators are also employed to extend the upper passband bandwidth. The ratio of the first spurious mode to the fundamental one can be controlled by choosing electrical length of the compound resonators.

# Chapter 3

# BASIC THEORIES OF FILTERS

## 3.1 Introduction

Microwave filter theory has be introduced since 1930's, and is still developing due to the integration of active devices in filter circuits and ongoing development in network synthesis with distributed elements [47], [74]. Early microwave filter design was conducted by using the image parameter method, but for a more accurate design, insertion loss method and coupling matrix method were introduced based on prescribed frequency response such as Butterworth response, Chebeshe response and Elliptic function response [75]-[78].

In order to help to develop and understand the proposed works in this thesis, some basic theories and concepts such as the ideal requirement for a constant absolute bandwidth tuning of a conventional tunable bandpass filter (single-mode filter), the concept of tuning rate of a resoantor, external quality factor ($Q_e$) extract methods, and capacitively loaded slow-wave transmission line resonator are addressed below.

## 3.2 Conventional Tunable Bandpass Filter Design Method

Generally, tunable bandpass filters are of narrow bandwidth, hence, it is convenient to employ the external quality factor ($Q_e$) of the end resoantors and coupling coefficients ($k$) between adjacent resonators as the design parameters [47]. These parameters may be derived from a lowpass prototype shown in Figure 3-1(a). By employing lowpass to bandpass transformation and impedance inverter ($K$), a corresponding bandpass filter prototype with only one type of resoantors (series-type resoantors) can be achieved as depicted in Figure 3-1(b). From Figure 3-1(b), a generalized bandpass filter prototype using impedance inverters can be derived as illustrated in Figure 3-1(c). where $g_j$ denote the prototype filter element values ($j$ =1 to n-1, n is the order of the filter), $L_{rj}$ and $C_{rj}$ denote the series resonators derived from

the lowpass to bandpass frequency transformation of the lowpass prototype filter. $K_{j,j+1}$ presents the impedance inverter. $X_j(\omega)$ denotes the generalized resonator, $\omega_1'$ denotes the cutoff angular frequency of the lowpass prototype filter, $\omega_0$, $\omega_1$, $\omega_2$, and *FBW* are the center frequency, the two edge frequencies of the passband, and the fractional bandwidth of the corresponding bandpass filter, respectively, and $R_A$, $R_B$ denote the impedance of the source and load.

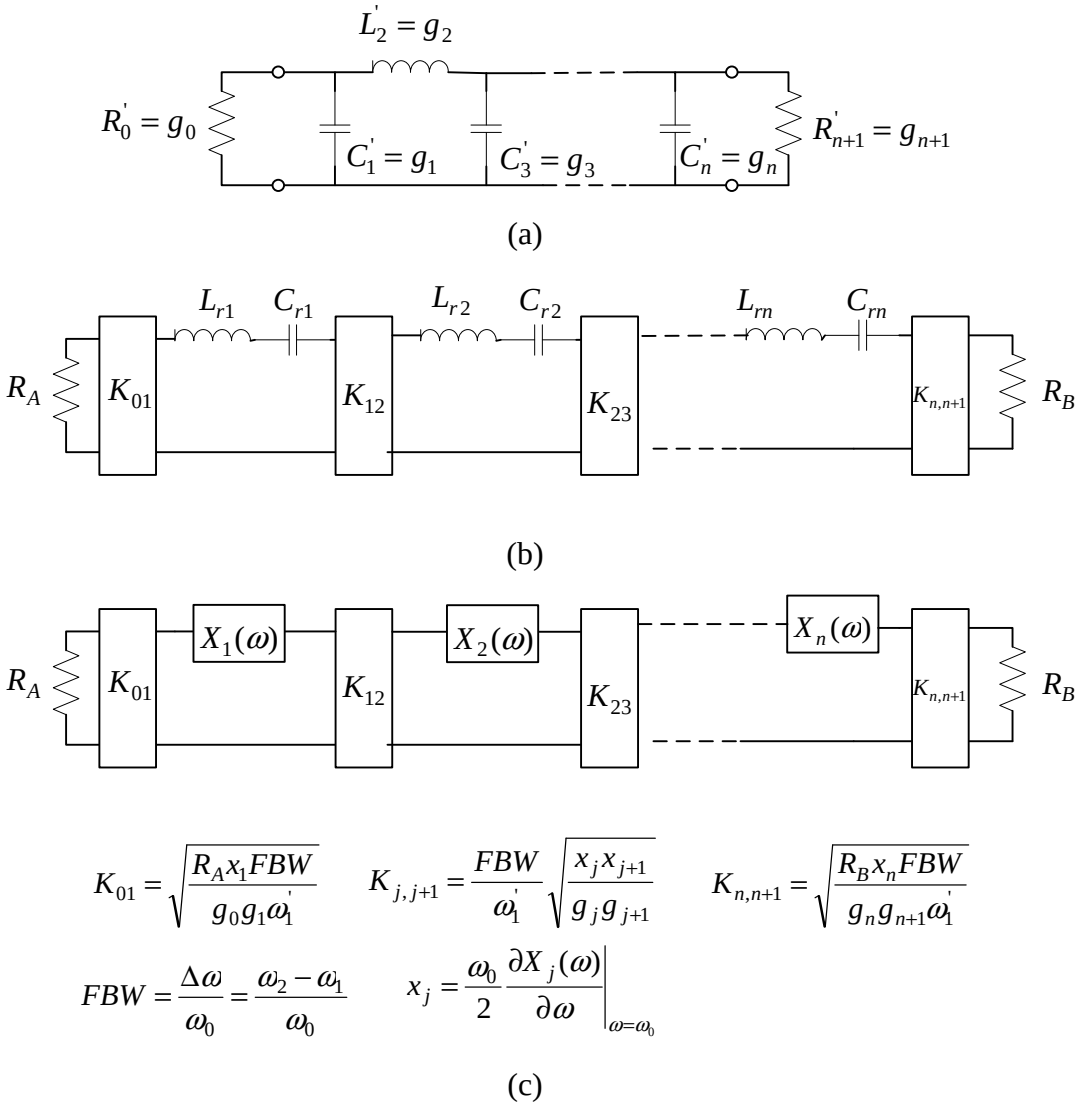


$$K_{01} = \sqrt{\frac{R_A x_1 FBW}{g_0 g_1 \omega_1'}} \qquad K_{j,j+1} = \frac{FBW}{\omega_1'}\sqrt{\frac{x_j x_{j+1}}{g_j g_{j+1}}} \qquad K_{n,n+1} = \sqrt{\frac{R_B x_n FBW}{g_n g_{n+1} \omega_1'}}$$

$$FBW = \frac{\Delta\omega}{\omega_0} = \frac{\omega_2 - \omega_1}{\omega_0} \qquad x_j = \frac{\omega_0}{2}\frac{\partial X_j(\omega)}{\partial \omega}\bigg|_{\omega=\omega_0}$$

Figure 3-1. (a) A lowpass prototype filter. (b) Its corresponding bandpass filter using impedance inverter. (c) A generalized bandpass filter using impedance inverter [47].

The quality factor $Q$ of any resonator having a series-type resonance and series resistance R can be defined by [47]

$$Q = \frac{x}{R} \qquad (3.1)$$

where $x$ is the reactance slope parameter of the resonator, given by

$$x = \frac{\omega_0}{2} \frac{\partial X}{\partial \omega}\bigg|_{\omega=\omega_0} \qquad (3.2)$$

where $X$ is the reactance of the resonator.

Likewise, the quality factor $Q$ of any resonator having a shunt-type resonance and shunt conductance G can be defined by

$$Q = \frac{b}{G} \qquad (3.3)$$

where $b$ is the susceptance slope parameter of the resonator, given by

$$b = \frac{\omega_0}{2} \frac{\partial B}{\partial \omega}\bigg|_{\omega=\omega_0} \qquad (3.4)$$

where $B$ is the susceptance of the resonator.

By using (3.1), the quality factor $Q_e$ of the first and the last resonators in Figure 3-1(c) can be determined as

$$Q_e = \frac{x_1}{R_A^{'}} = \frac{x_1}{(K_{01}^2 / R_A)} \qquad (3.5)$$

with

$$x_1 = \omega_0 L_{r1} = \frac{1}{\omega_0 C_{r1}}$$

This is illustarted in Figure 3-2.

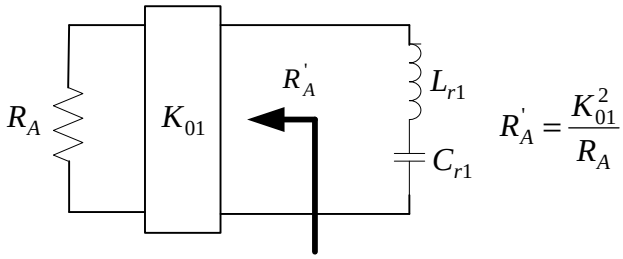


Figure 3-2. Calculation of the external quality factor Qe.

The generalized coupling coefficient ($k_{j,j+1}$) may be found from the usual definition of coupling coefficient for a lumped element resoantors with inductive couplings as [1]

$$k_{j,j+1} = \frac{L_{j,j+1}}{L_j L_{j+1}} \qquad (3.6)$$

where $L_{j,j+1}$ denotes the mutual inductance, $L_j$ and $L_{j+1}$ denote the self inductances. From (3.6), the coupling coefficients $k_{j,j+1}$ of the generalized bandpass filter in Fgiure 3-1(c) can be determined as

$$k_{j,j+1}\Big|_{j=1\_to\_n-1} = \frac{K_{j,j+1}}{\sqrt{x_j x_{j+1}}} \qquad (3.7)$$

From the above analysis, the design paramenters for a generalized narrow-bandwidth bandpass filter can be given by

$$(Q_e)_A = \frac{x_1}{(K_{01}^2 / R_A)} = \frac{g_0 g_1 \omega_1^{'}}{FBW} = \frac{g_0 g_1 \omega_1^{'} \omega_0}{\Delta\omega} \qquad (3.8)$$

$$(Q_e)_B = \frac{x_n}{(K_{n,n+1}^2 / R_B)} = \frac{g_n g_{n+1} \omega_1^{'}}{FBW} = \frac{g_n g_{n+1} \omega_1^{'} \omega_0}{\Delta\omega} \qquad (3.9)$$

$$k_{j,j+1}\Big|_{j=1\_to\_n-1} = \frac{K_{j,j+1}}{\sqrt{x_j x_{j+1}}} = \frac{FBW}{\omega_1^{'}\sqrt{g_j g_{j+1}}} = \frac{\Delta\omega}{\omega_0 \omega_1^{'}\sqrt{g_j g_{j+1}}} \qquad (3.10)$$

It is clear that to achieve a constant absolute bandwidth over a wide tuning range, which means $\Delta\omega$ is kept constant, thus, external quality factor $Q_e$ must vary directly with the tuning frequency and coupling coefficient ($k$) must also vary inversely with the tuning frequency.

### 3.3 Tuning rate of a resonator

In order to shift the odd-and even-mode resonant frequencies proportionally by loading the same capacitance in the proposed tunable dual-mode filter design in Chapter 4, the concept of tuning rate of a resonator is introduced. The tuning rate of a resonator indicates how much a resonant frequency is shifted by varying a loading capacitance, which can be controlled by varying the characteristic admittance (or characteristic impedance) of a resonator. A simple circuit model is used to demonstrate this as shown in Figure 3-3(a).

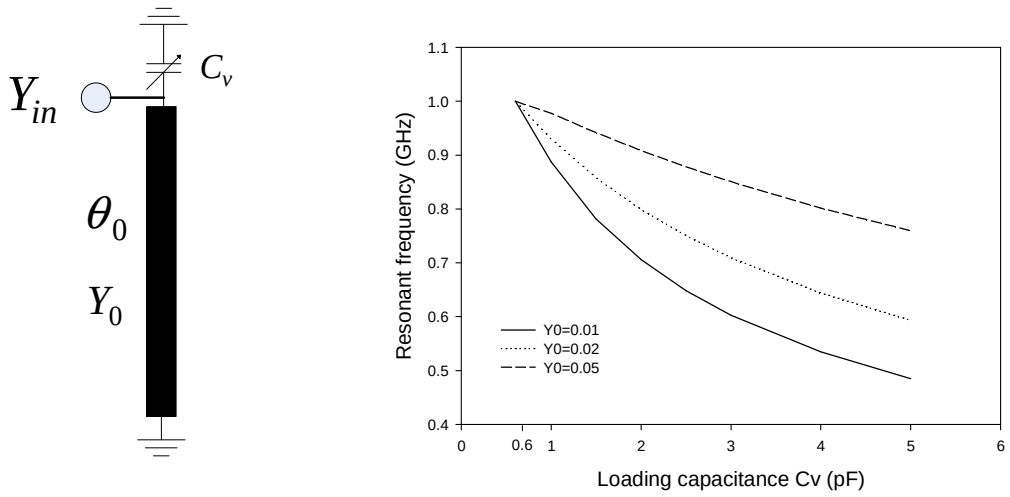


(a) (b)

Figure 3-3. (a) Circuit model of a resonator. (b) Calculated frequency response.

As it can be seen, one end of the resonator is loaded with a variable capacitance $C_v$ while the other end is short-circuited. Assume $C_v$ varies from $C_{v1}$ to $C_{v2}$, the corresponding resonant frequency shifts from $f_{01}$ to $f_{02}$, hence, the tuning rate can be defined by

$$Tuning\ rate = \frac{|f_{02} - f_{01}|}{|C_{v2} - C_{v1}|}\ \text{(GHz/pF)} \qquad (3.11)$$

A reference port is added for deriving an input admittance $Y_{in}$, which is given by

$$Y_{in} = j(\omega C_v - \frac{Y_0}{\tan\theta_0}) \qquad (3.12)$$

where $Y_0$ and $\theta_0$ are the admittance and electrical length of the resonator.

The resonant frequency of the resonator can be found by

$$\text{Im}[Y_{in}] = 0 \qquad (3.13)$$

Assume the resonator is resonant at 1 GHz with a loading capacitance of 0.6 pF. For different values of admittance, i.e., $Y_0$ =0.01 (S), 0.02 (S), and 0.05 (S), the corresponding electrical length $\theta_0$ can be found from (3.12)-(3.13) as 68˚, 80˚, and 85˚, respectively. By varying the loading capacitance $C_v$ from 0.6 to 5.0 pF, the shifts of the resonant frequency for different values of admittance of the resonator are plotted in Figure 3-3(b), and the tuning rates, calculated using (3.11), are listed in Table 3-1. It is evident that the smaller the admittance of the resonator is, the faster the resonant frequency is shifted (larger tuning rate). To this end, it can be concluded that by varying the admittance of a resonator, the corresponding tuning rate can be controlled.

**TABLE 3-1**

**Comparison of the tuning rates for different admittance of the resonator shown in Figure 3-3(a).**

| Admittance $Y_0$ (S) | Loading capacitance $C_v$ (pF) | Resonant frequency tuning | | Tuning rate |
|---|---|---|---|---|
| | | Start (GHz) | End (GHz) | |
| 0.01 | 0.6 to 5.0 | 1.0 | 0.4851 | 11.7% |
| 0.02 | 0.6 to 5.0 | 1.0 | 0.5931 | 9.2% |
| 0.05 | 0.6 to 5.0 | 1.0 | 0.7595 | 5.5% |

## 3.4 External quality factor ($Q_e$) extract methods

External quality factor ($Q_e$) is one of the important parameters in a narrow bandpass filter design, which can mainly affect the shape of the passband response of a filter. External quality factor ($Q_e$) can be calculated from a circuit model by using equations or can be extracted from a full-wave electromagnetic (EM) simulation. To demonstrate these methods, an example for extracting $Q_e$ of a combline filter is given below.

Figure 3-4(a) shows a combline bandpass filter feed using tapped lines. For narrow band applications, the coupling effect between the first and the second resonators may be neglected for deriving $Q_e$ of the filter. Thus, the first (or the last) resonator loaded with the source (or the load) admittance $G_0$ can be given as depicted in Figure 3-4(b). The resonator is loaded with a capacitance $C_v$ at one end and shorted-circuited at the other end. The input admittance $Y_{in}$ can be derived by

$$Y_{in} = jY_0\left(\frac{\omega C_v + Y_0 \tan\theta_1}{Y_0 - \omega C_v \tan\theta_1} - \frac{1}{\tan(\theta_0 - \theta_1)}\right) \qquad (3.14)$$

with

$$\omega = 2\pi f$$

where $Y_0$ and $\theta_0$ are the admittance and the electrical length of the resonator, $\theta_1$ denotes the location of the tapped line.

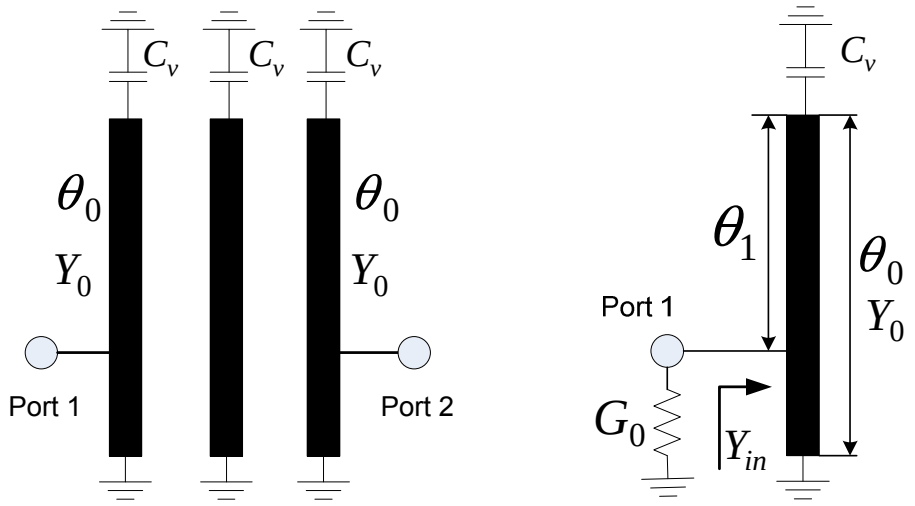


(a) (b)

Figure 3-4. (a) A combline filter using tapped-line-feed. (b) The first (or last) resonator of the filter with port 1 excited.

The resonant frequency ( $f_0$ ) of the resonator can be found from (3.15)

$$\mathrm{Im}[Y_{in}] = 0 \qquad (3.15)$$

As the resonator can be considered as a shunt-type resonator connected with a shunt conductance (the source $G_0$ ), the $Q_e$ may be determined by (3.16) as

$$Q_e = \frac{b}{G_0} \qquad (3.16)$$

with

$$b = \frac{f_0}{2} \frac{\partial \,\mathrm{Im}[Y_{in}]}{\partial f}\bigg|_{f=f_0}$$

where $b$ is the susceptance slope parameter and $f_0$ is the resonant frequency of the resonator.

External quality factor ($Q_e$) can also be extracted in light of full-wave EM simulation, which can be more accurate comparing to the circuit model extract method. This is because parasitic effects, i.e., discontinuities of transmission line, open-end fringing field effects, and unwanted cross coupling effects can be taken into account by using full-wave EM simulation. External quality factor ($Q_e$) of a resonator can be related to its frequency response by [1]

$$Q_e = \frac{f_0}{\Delta f_{3dB}} \qquad (3.17)$$

with

$$f_0 = (f_1 + f_2)/2\ , \quad \Delta f_{3dB} = f_2 - f_1$$

where $f_0$ and $\Delta f_{3dB}$ are the resonant frequency and 3dB bandwidth of the frequency response. These parameters are illustrated in Figure 3-5(b). Figure 3-5(b) is a typical frequency response of a resonator excited by weak couplings and Figure 3-5(a) shows a layout of extracting $Q_e$ of a resonator using full-wave EM simulation [79]. Port 2 is weakly excited as the resonator is considered as single loaded resonator by port 1. A reference place and a tip-feed line are used to minimize the discontinuity effects. To compare the two extract methods, assume $Y_0$=0.014 S, $\theta_0$=53˚, $\theta_1$=41˚, $C_v$=1.6 pF and $G_0$=0.02 S. The corresponding dimensions of the stripline resonator based on a substrate with dielectric constant $\varepsilon_r$=3.0 and a thickness of 2.0 mm can be found and shown in Figure 3-5(a). The stripline structure (operating in TEM mode) is used so as to have a close response to the ideal circuit model. $Q_e$ and $f_0$ of the resonator can then be calculated using (3.14)-(3.16) and extracted using (3.17) by performing full-wave EM simulation [79]. Both results are given in Table 3-2.

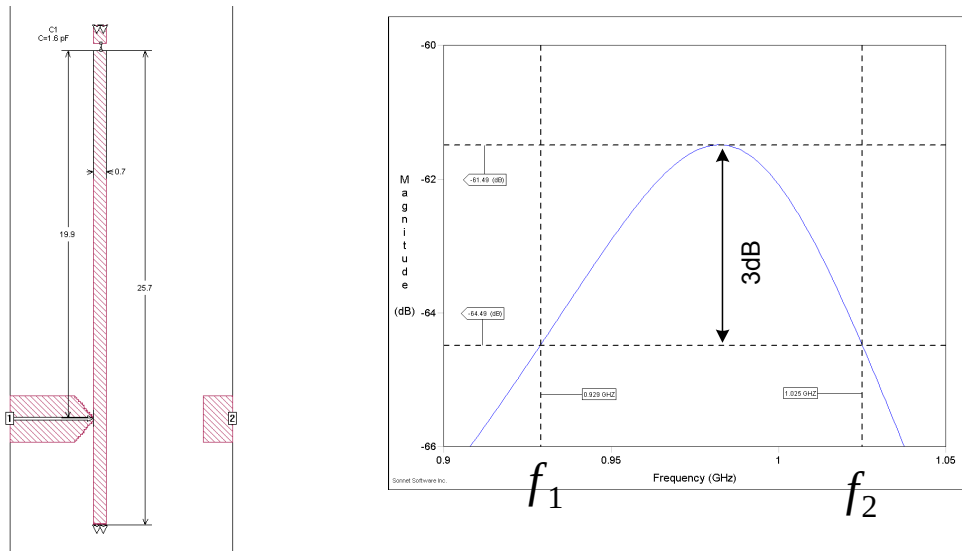


(a) (b)

Figure 3-5. (a) Layout of extracting $Q_e$ of a resonator. (b) Its frequency response.

**TABLE 3-2**

**Comparison of $Q_e$ extract methods.**

| Extract methods | $f_0$ (GHz) | $Q_e$ |
|---|---|---|
| circuit model extract method | 1.009 | 10.354 |
| full-wave EM simulation extract method | 0.98 | 10.17 |

The difference between the two results may due to parasitic effects such as discontinuity effects and open-end fringing field effects. Notice that external quality factor $Q_e$ can also be extracted from group delay of a resonator frequency response by performing full-wave EM simulation, which will be addressed in Chapter 4.

### 3.5 Slow-wave resonators

In order to minimize the size of a filter and to achieve a wider upper stopband, slow-wave resonators are usually employed in filter designs [80]-[82]. Generally, planar bandpass filters that are comprised of half-wavelength resonators inherently have a spurious passband at $2\ f_0$. The spurious passband can be suppressed by cascading a lowpass filter or bandstop filter in the cost of larger circuit size and extra insertion loss. Quarter-wavelength resonator filters have the first spurious passband at $3\ f_0$, but they require short-circuit connection to ground, which may be no desired in planar filter fabrication techniques. Lumped-element filters ideally do not have any spurious response. However, they suffer from poorer power handling and higher loss. To this end, a new type of slow-wave resonator was introduced by Hong, et. al [82] as shown in Figure 3-6.

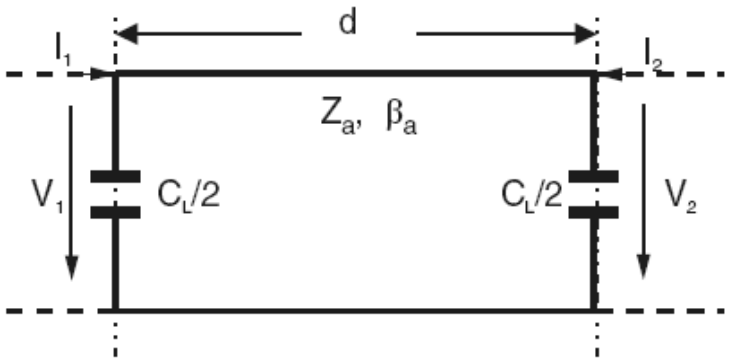


Figure 3-6. Capacitively loaded transmission line resonator [1].

where $C_L$ is the loaded capacitance, $Z_a$, $\beta_a$, and $d$ are the characteristic impedance, the propagation constant and the length of the unloaded lossless transmission line resonator. By employing the loading capacitance, electromagnetic (EM) wave energy can be stored in the capacitors, resulting in a slow-wave effect. The detailed analysis of this type of slow-wave resonator is given below [1].

The circuit response of the resonator shown in Figure 3-6 may be determined by

$$\begin{bmatrix} V_1 \\ I_1 \end{bmatrix} = \begin{bmatrix} A & B \\ C & D \end{bmatrix} \cdot \begin{bmatrix} V_2 \\ -I_2 \end{bmatrix} \qquad (3.18)$$

with

$$A = D = \cos\theta_a - \frac{1}{2}\omega C_L Z_a \sin\theta_a \tag{3.19}$$

$$B = jZ_a \sin\theta_a \tag{3.20}$$

$$C = j\left(\omega C_L \cos\theta_a + \frac{1}{Z_a}\sin\theta_a - \frac{1}{4}\omega^2 C_L^2 Z_a \sin\theta_a\right) \tag{3.20}$$

where $\theta_a = \beta_a d$ is the electrical length of the resonator. $\omega = 2\pi f$ denotes the angular frequency. A, B, C, and D are the network parameters of the transmission matrix. By applying the boundary conditions $I_1 = I_2 = 0$, the resonant condition can be found as

$$\cos\theta_{a0} - \frac{1}{2}\omega_0 C_L Z_a \sin\theta_{a0} = -1 \tag{3.21}$$

$$\cos\theta_{a1} - \frac{1}{2}\omega_1 C_L Z_a \sin\theta_{a1} = 1 \tag{3.22}$$

Notice that

$$A = \left.\frac{V_1}{V_2}\right|_{I_2=0} = \begin{cases} -1\_(\text{for the fundamental resonance}) \\ 1\_(\text{for the first spurious resonance}) \end{cases} \tag{3.23}$$

$$\frac{C}{A} = \left.\frac{I_1}{V_1}\right|_{I_2=0} = \left.\frac{I_2}{V_2}\right|_{I_1=0} = 0 \tag{3.24}$$

where the subscripts 0 and 1 denote the fundamental and the first spurious resonance, respectively. The two eigenequations can be found from (3.18)-(3.22) as

$$\theta_{a0} = 2\tan^{-1}\left(\frac{1}{\pi f_0 C_L Z_a}\right) \qquad (3.25)$$

$$\theta_{a1} = 2\pi - 2\tan^{-1}\left(\pi f_1 C_L Z_a\right) \qquad (3.26)$$

From which the fundamental resonant frequency $f_0$ and the first spurious resonant frequency $f_1$ can be calculated and plotted in Figure 3-7, as well as their ratio for different loading capacitance.

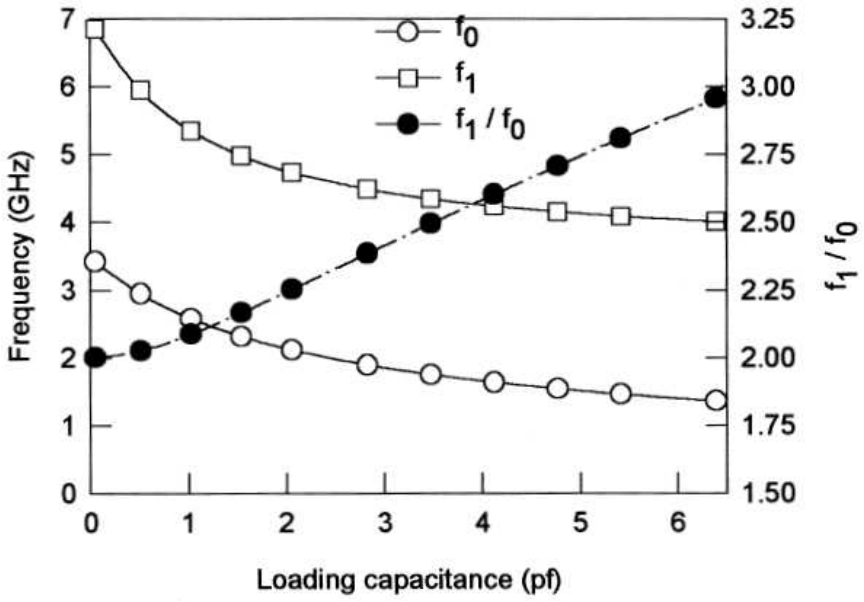


Figure 3-7. Fundamental and first spurious resonant frequencies of a capacitively loaded transmission line resonator, as well as their ratio against loading capacitance [1].

It is clear that both resonant frequencies decrease as the loading capacitance is increased, which indicates a slow-wave effect. However, the ratio of the first spurious resonant frequency to the fundamental one is increased. The reason behind this phenomenon may be explained by calculating the propagation constant (or phase velocity) of the transmission line. To do this, Floquet's theorem [83] may be applied, i.e.,

$$V_2 = e^{-j\beta d} V_1 \qquad (3.27)$$

$$-I_2 = e^{-j\beta d} I_1 \qquad (3.28)$$

Note that the circuit of Figure 3-6 may be considered as a unit cell of a periodically loaded transmission line. By substituting (3.27) and (3.28) to (3.18)-(3.22), the dispersion equation can be derived by

$$\cos(\beta d) = \cos\theta_a - \frac{1}{2}\omega C_L Z_a \sin\theta_a \qquad (3.29)$$

Since the dispersion equation governs the wave propagation characteristics of the loaded line, the phase velocities of the loaded line at the fundamental ($v_{p0}$) and the first spurious resonant frequency ($v_{p1}$) can be obtained by applying corresponding resonant frequency ( $f_0$ and $f_1$) into (3.29), which can be given as

$$\frac{f_1}{f_0} = 2\frac{v_{p1}}{v_{p0}} \qquad (3.30)$$

If there were no dispersion, the phase velocity would be a constant. However, for the periodically loaded line, the phase velocity is frequency-dependent. As can be seen from (3.30), the dispersion is increased when the ratio of the first spurious resonant frequency to the fundamental one is increased by loading larger capacitance.

Based on this type of resonator, a new type of dual-mode slow-wave resonators can be developed, which will be employed to build the proposed miniature dual-band filters in Chapter 5.

## 3.6 Summary

Some basic theories of filters have been addressed in detail to help to develop the proposed filters in this thesis.

For a tunable filter design, in order to achieve a constant absolute bandwidth over a wide tuning range, external quality factor $Q_e$ must vary directly with the tuning frequency and coupling coefficient ( $k$ ) must also vary inversely with the tuning frequency. The ideal requirement of these parmeters can be derived from a lowpass prototype.

The concept of tuning rate of a resoantor has been introduced in Section 3.3. It shows that the tuning rate of a resonator may depend on the characteristic impedance of the resonator.

To extract external quality factor $Q_e$ from a practical filter, both circuit model extract method and full-wave EM simulation extract method can be applied. The results of the example in Section 3.4 show a good agreement between the two methods.

Slow-wave resonators are usually employed to design a compact bandpass filter with a wide upper stopband. Detailed analysis of a novel capacitively loaded transmission line resonator has been given, which shows slow-wave effect can occur when capacitance is loaded on a transmission line resonator, and dispersion phenomenon on a periodically capacitive loaded transmission line has also been discussed.

# Chapter 4

# NOVEL DUAL-MODE TUNABLE FILTERS

## 4.1 Introduction

Dual-mode microstrip resonator tunable filters are attractive because each dual-mode resonator can be used as a doubly tuned resonant circuit and, therefore, the number of resonators required for a given degree of filter is reduced by half, resulting in a compact filter configuration.

Chun *et al*. [11] and Liao et al. [12] introduced a new type of electronically tunable dual-mode microstrip resonator bandpass filter. In difference with the conventional dual-mode filter, this new type of dual-mode resonator filter exhibits a distinct characteristic, for which the dual modes do not couple. This leads to a simple tuning scheme since tuning the passband frequency is accomplished by merely changing the two modal frequencies proportionally. Moreover, high selectivity performance can be achieved due to a finite transmission zero associated with the even mode of the dual-mode resonator. However, the reported filters only showed a tuning range of about 10%, and two DC bias circuits are required to control its odd and even-mode resonant frequencies by loading different capacitance. In order to simplify the biasing circuit by using single DC bias scheme and improve the tuning range, a possible solution is addressed in this chapter, in which, a wideband transformer and odd/even-mode tuning rate method are employed.

Two two-pole tunable bandpass filters and a four-pole tunable bandpass filter of this type are designed, simualted and tested experimentally.

## 4.2 Two-Pole Varactor-Tuned Dual-Mode Bandpass Filters

In this section, Two two-pole varactor-tuned bandpass filters have been investigated theoretically. By employing a wideband transformer and odd/even-mode tuning rate method, the filters can be achieved a tuning range of 41% while keeping a

nearly constant absolute bandwidth using a single DC bias circuit. The filters exhibit high selectivity on either side of passband due to a finite-frequency transmission zero associated with even mode of the dual-mode resonator and this transmission zero can be shifted along the passband when both the odd and even modes are tuned.

The proposed filter structure is shown in Figure 4-1. It can be seen that a wideband transformer is applied as the input/output (I/O) coupling structure for the filter. The wideband transformer may be considered as a type of interdigital coupled lines, which is known to have a dominant inductive coupling with wideband behaviour. Therefore, the I/O coupling can be adjusted to achieve constant bandwidth tuning requirement over a wide tuning range. While for the transformer used in the reported filters [11]-[12], capacitive coupling is dominant and it is difficult to control I/O coupling properly over a wide tuning range due to the lack of inductive coupling associated with the structure. In a conventional tunable dual-mode filter, I/O coupling is used to compensate both the variation of a slope parameter $x$ (or $b$) and the coupling between resonators due to the frequency change. However, for the proposed dual mode tunable filter, I/O coupling is only used to compensate the variation of $x$ (or $b$) since its even and odd modes do not couple to each other.

Design equations and procedures are derived as follows.

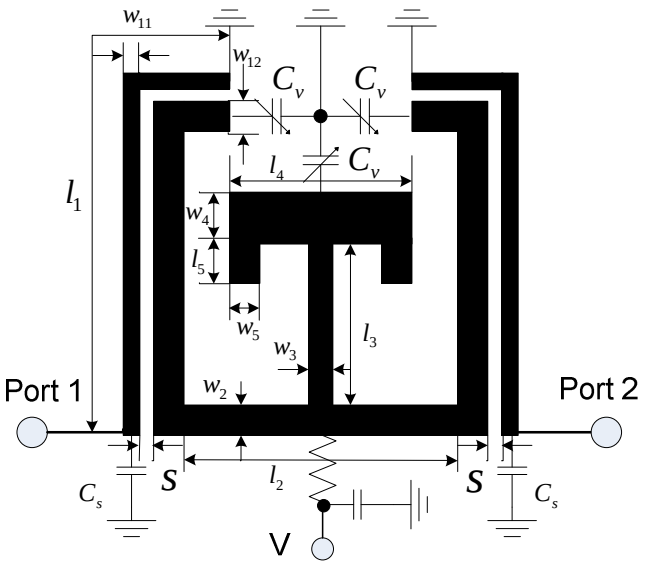


Figure 4-1. Layout of the proposed two-pole dual-mode tunable filter.

### *4.2.1 Theory and design equations*

For our investigation, Figure 4-1 shows a layout of the proposed two-pole varactor-tuned dual-mode microstrip bandpass filter. Variable capacitances $C_v$ are supposed to be loaded varactors. These three same varactors are to be used with a single DC bias circuit, which makes both the implementation and tuning simple.

The proposed dual-mode filter has a coupling scheme as shown in Figure 4-2, where S and L denote the input and output ports respectively; node 1 denotes the odd mode and node 2 for the even mode. Because this two operating modes do not couple, this leads to a simple tuning scheme. How to achieve this ideally is discussed below.

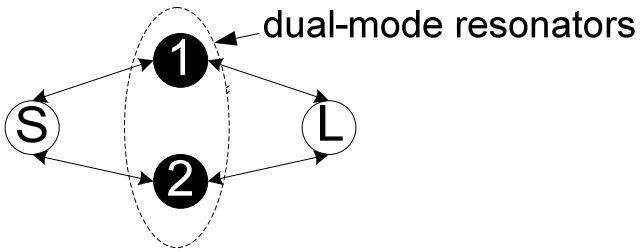


Figure 4-2. The coupling scheme of the filter.

#### *4.2.1.1 Ideal requirement for tunable dual-mode filter*

To tune the center frequency of this type of dual-mode filter while keeping constant filter response shape and bandwidth, two factors ideally need to be considered. Firstly, the resonant frequencies of odd-mode ( $f_0^o$ ) and even-mode ( $f_0^e$ ) need to be shifted proportionally. Secondly, the shape and bandwidth of odd-and even-mode frequency response must keep constant over the entire tuning range, this would require the external quality factor for the odd-mode ($Q_{exo}$) and even-mode ($Q_{exe}$) vary directly with the tuning frequency [47]. These parameters may be represented by

$$\left| f_0^e - f_0^o \right| = A \qquad (4.1)$$

$$Q_{exe} = \frac{f_0^e}{\Delta f_{3dB}^e} \tag{4.2}$$

$$Q_{exo} = \frac{f_0^o}{\Delta f_{3dB}^o} \tag{4.3}$$

where A denotes the separation between even-and odd-mode resonant frequencies; $\Delta f_{3dB}^o$, $\Delta f_{3dB}^e$ are the 3-dB bandwidths of odd-and even-mode, respectively [1]. Note that ideally $\Delta f_{3dB}^e$, $\Delta f_{3dB}^o$ and A are to be constant over the entire tuning range for constant absolute bandwidth tuning.

It is notice that ideal requirement for tunable dual-mode filter is distinct to that of conventional tunable filter discussed in Section 3.2 due to two operating modes of the dual-mode filter do not couple.

To determine the desired curves from the equations (4.1)-(4.3) for a prescribed frequency response, a coupling matrix method may be applied [75], [78]. According to the coupling scheme in Figure 4-2, the coupling matrix of the filter may be defined as

$$M = \begin{bmatrix} 0 & ms1 & ms2 & 0 \\ ms1 & m11 & 0 & mL1 \\ ms2 & 0 & m22 & mL2 \\ 0 & mL1 & mL2 & 0 \end{bmatrix} \tag{4.4}$$

where *msi* (i=1 to 2) presents the coupling between the source and resonators, *mLi* denotes the coupling between the load and resonators, *mii* denotes resonator tuning. In order to excite the odd and even modes, this requires $mL1 = -ms1$ and $mL2 = ms2$. To calculate the transmission coefficient S21 and reflection coefficient S11 of the proposed coupling matrix, the following expressions may be employed [75].

$$S_{21} = -2j[A]^{-1}_{n+2,1} \tag{4.5}$$

$$S_{11} = 1 + 2j[A]^{-1}_{1,1} \tag{4.6}$$

where n denotes the number of resonators, $[A]_{ij}^{-1}$ is the $i$ th row and $j$ th column element of $[A]^{-1}$, the matrix $[A]$ is given by

$$[A]=[m]+\Omega[U]-j[q] \qquad (4.7)$$

where $[U]$ is the identity matrix of $(n+2)\times(n+2)$ except that $[U]_{11}=[U]_{n+2,n+2}=0$, $[q]$ denotes the $(n+2)\times(n+2)$ matrix with all entries zeros except for $[q]_{11}=[q]_{n+2,n+2}=1$, and $\Omega$ is the frequency variable of the lowpass prototype. For the synthesis of the coupling matrix coefficients, a gradient-based optimization technique can be employed [1]. After the matrix coefficients are determined, the odd-and even-mode resonant frequencies ( $f_0^o$ , $f_0^e$ ) and external quality factor ( $Q_{exo}$ , $Q_{exe}$ ) can be derived by [75]

$$f_o^o = f_0 - \frac{f_0 \cdot FBW}{2} m11 \qquad (4.8)$$

$$f_o^e = f_0 - \frac{f_0 \cdot FBW}{2} m22 \qquad (4.9)$$

$$Q_{exo} = \frac{1}{FBW \cdot ms1^2} \qquad (4.10)$$

$$Q_{exe} = \frac{1}{FBW \cdot ms2^2} \qquad (4.11)$$

where $f_0$ is the centre frequency and $FBW$ is the fractional bandwidth of the prescribed frequency response. From (4.8)-(4.11) and (4.1)-(4.3), the design curves of the dual-mode tunable filter can be determined.

#### *4.2.1.2 Odd-and even-mode tuning rates*

To shift the odd-and even-mode resonant frequencies proportionally by loading the same capacitance, the tuning rate of odd and even modes need to be characterized.

The concept of tuning rate of a resonator can be referred to Section 3.3. The tuning rate indicates how much an odd or even modal frequency is shifted by varying capacitance $C_v$. Assume $C_v$ varies from $C_{v1}$ to $C_{v2}$, the odd-mode frequency shifts from $f_{01}^o$ to $f_{02}^o$, and the even-mode frequency shifts from $f_{01}^e$ to $f_{02}^e$. Thus, the tuning rate of odd-and even-mode can be defined as

$$Tuning\ rate = \frac{\left| f_{02}^{o/e} - f_{01}^{o/e} \right|}{\left| C_{v2} - C_{v1} \right|} \text{ (GHz/pF)} \qquad (4.12)$$

where the superscript $o/e$ denotes the odd or even modes.

By placing a short circuit or open circuit at the symmetric plane of the circuit in Figure 4-1, we obtain the circuit model for the odd mode or even modes, without input/output coupling as shown in Figure 4-3(a) and (c). To demonstrate that how to control the modal tuning rate, the circuit models of Figure 4-3(a) and (c) may be modified as that of Figure 4-3(b) and (d), respectively. A reference port is added for deriving an input admittance, i.e., for the odd mode,

$$Y_{ino} = j(\omega C_v - \frac{Y_o}{\tan\theta_o}) \qquad (4.13)$$

and for the even-mode,

$$Y_{ine} = j\{Y_0 \frac{Y_L + Y_0 \tan\theta_0}{Y_0 - Y_L \tan\theta_0} + \omega C_v\} \qquad (4.14)$$

with

$$Y_L = Y_e \frac{\omega(C_v/2 + C_{stub}) + Y_e \tan\theta_e}{Y_e - \omega(C_v/2 + C_{stub})\tan\theta_e}$$

where $C_v$ is loading capacitance, $C_{stub}$ represents the bended short open-circuited stub, which may be estimated from $C_{stub} = (Y_1 \tan\theta_1)/\omega$. $Y_o, Y_e$, $Y_1, \theta_o, \theta_e$, and $\theta_1$ are the admittances and electrical lengths for the transmission line sections shown in Figure 4-3. The resonant frequencies of the odd and even mode can be found from (4.15)

$$\mathrm{Im}[Y_{ino}] = 0 \qquad \mathrm{Im}[Y_{ine}] = 0 \qquad (4.15)$$

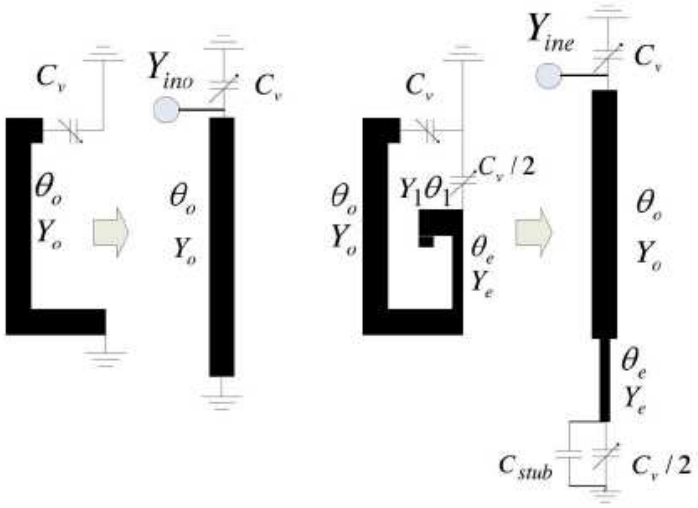


(a) (b) (c) (d)

Figure 4-3. Circuit model of (a, b) odd-mode and (c, d) even-mode.

From (4.13), it can be seen that the resonant frequency of the odd mode depends on the parameters $C_v$, $Y_o$, $\theta_o$. Assume that the loading capacitance $C_v$ varies from $C_{v1}$ (0.6 pF) to $C_{v2}$ (5 pF). For $\theta_o = 80^\circ$ at a nominal frequency of 1 GHz, the modal tuning rate can be calculated by (4.12) with different values $Y_o$, and the results are plotted in Figure 4-4 (a). Similarly, for $Y_o = 0.02$ S, the modal tuning rate can also be calculated against different values of $\theta_o$, and the results are present in Figure 4-4 (b). These two sets of results show that the smaller the admittance $Y_o$ or the shorter the electrical length $\theta_o$ is, the larger the modal tuning rate.

With loading the same capacitance range, the tuning rate of the even mode depending on the parameters $Y_e$ , $\theta_e$ is investigated. From equations (4.13) and (4.14), it is envisaged that the resonant frequency of the even mode can be shifted by varying $Y_e$ , $\theta_e$ while the resonant frequency of the odd mode is not changed for given $Y_o$ and $\theta_o$. This means that the tuning rate of the even mode may be controlled so as to match the tuning rate of the odd mode by varying $Y_e$ and $\theta_e$.

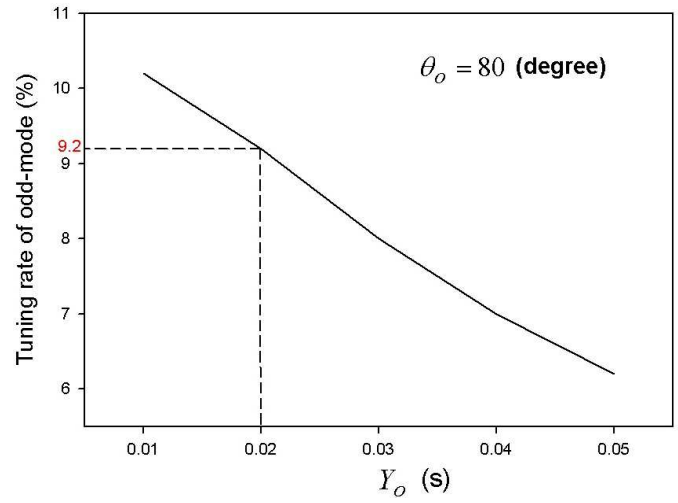


(a)

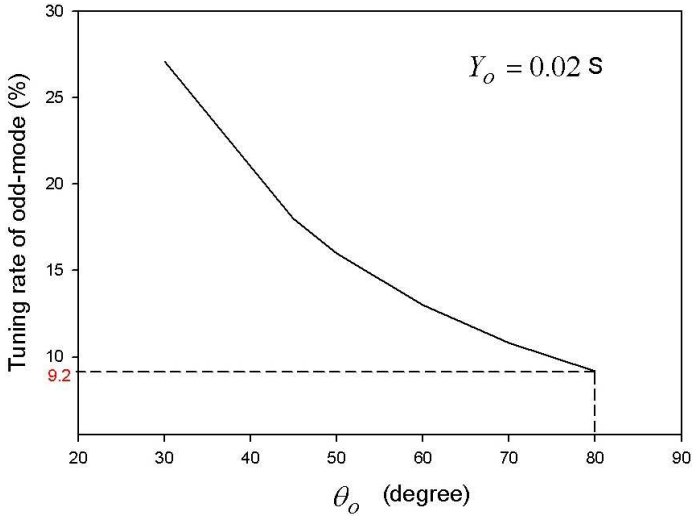


(b)

Figure 4-4. The tuning rate of odd-mode varies with (a) $Y_o$ and (b) $\theta_o$ (where $C_{v1} = 0.6$ pF; $C_{v2} = 5.0$ pF).

For given separations between the odd-and even-mode resonant frequencies over a loading capacitance range, the values of $Y_e$ and $\theta_e$ may be determined from (4.16) and (4.17),

$$\left| f_{01}^{e} - f_{01}^{o} \right|_{C_v = C_{v1}} = A \qquad (4.16)$$

$$\left| f_{02}^{e} - f_{02}^{o} \right|_{C_v = C_{v2}} = B \qquad (4.17)$$

where A, B are the separations between odd-and even-mode resonant frequencies for a loading capacitance of $C_{v1}$, $C_{v2}$. Ideally, they are also proportional to the bandwidth. For the constant absolute bandwidth tuning, the resonant frequencies of odd-mode and even-mode need to be shifted proportionally, hence, B should be equalled to A. To demonstrate how to achieve this, assume that A=100 MHz; $Y_o = 0.02$ S; $\theta_o$ = 80˚ at 1 GHz, which is the nominal high frequency of a given tuning range; $C_{v1} = 0.6$ pF; and $C_{v2} = 5.0$ pF. Also, for the demonstration, $C_{stub}$ is chosen for three values: $C_{stub}$ = 0, $C_{stub}$ = 0.3 pF and $C_{stub}$ =1.3 pF to represent different cases of the short open-circuited stub. By applying (4.13) and (4.14) and (4.16) and (4.17), $Y_e$, $\theta_e$ can be determined for B=A as follows: $Y_e = 0.018$ S and $\theta_e$ = 68.54˚ when $C_{stub}$ = 0; $Y_e = 0.016$ S and $\theta_e$ = 62.17˚ when $C_{stub}$ = 0.3 pF; $Y_e = 0.006$ S and $\theta_e$ = 23.43˚ when $C_{stub}$ = 1.3 pF. After $Y_e$, $\theta_e$ are determined, the tuning rate of even mode can then be calculated by (4.12), for all the three cases, as 9.2%, which is equal to that of odd mode (see Figure 4-4). The resonant frequencies of the odd and even modes against the loading capacitance $C_v$, varying from 0.6 to 5.0 pF, are plotted in Figure 4-5 for a comparison. Note that, for the even mode, the curves for the three different values of $C_{stub}$ coincide together, which implies that the effect of the short open-circuited stub can easily be compensated by $Y_e$ and $\theta_e$ with negligible influence to the even-mode tuning rate. This, however, allows a more flexible design for the loading element inside the open loop. From the analysis above, it is clear that the tuning rate of the even mode is controllable to be equal to the tuning rate of the odd mode. As such, the resonant frequencies of the two operating modes can be controlled to shift proportionally.

The separation between the modal frequencies, which is ideally proportional to the bandwidth, varies with the tuning range present in Figure 4-6, obtained by using (4.13) and (4.14) and (4.16) and (4.17). It shows that the wider the tuning range, the larger the variation of the frequency separation. This somewhat limits the tuning range for a large constant absolute bandwidth.

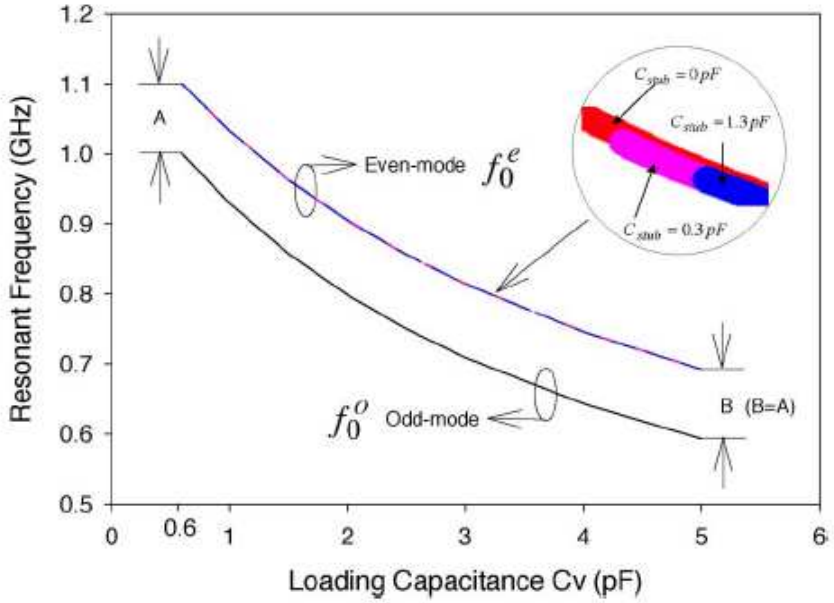


Figure 4-5. The resonant frequency of even-mode comparing with that of odd-mode.

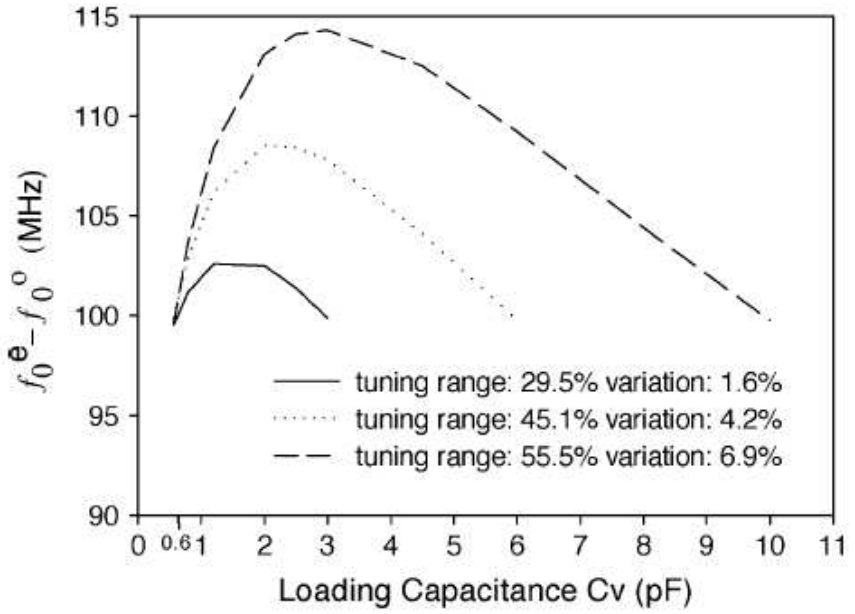


Figure 4-6. Modal frequency separation varies against the tuning range. (Note that for the tuning range of 29.5%, $Y_e = 0.0163\,\mathrm{S}$ and $\theta_e = 69.04^\circ$; for the tuning range of 45.1%, $Y_e = 0.0185\,\mathrm{S}$ and $\theta_e = 68.8^\circ$; for the tuning range of 55.5%, $Y_e = 0.0215\,\mathrm{S}$ and $\theta_e = 68.44^\circ$. )

#### *4.2.1.3 External coupling of the filter*

With the input/output coupling, the circuit models of odd and even modes are present in Figure 4-7. The input reflection coefficient of odd mode ($S_{11o}$) and even mode ($S_{11e}$) may be found by

$$S_{11o}(f) = S_{11}(f) - S_{21}(f) \qquad (4.18)$$

$$S_{11e}(f) = S_{11}(f) + S_{21}(f) \qquad (4.19)$$

where $S_{11}(f)$ and $S_{21}(f)$ are the two-port scattering parameters of the filter [1], which can be extracted using a full-wave electromagnetic (EM) simulation tool [79].

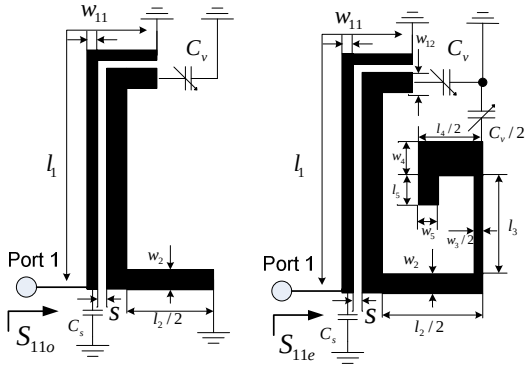


(a) (b)

Figure 4-7. Circuit model of (a) odd mode and (b) even mode with input/output coupling.

The external quality factor of odd-mode ($Q_{exo}$) and even-mode ($Q_{exe}$) of the proposed filter may be derived from the group delay of the input reflection coefficient of odd-and even-mode [1] as follows:

$$Q_{exo} = \frac{2\pi f_0^o \cdot \tau_{S11o}(f_0^o)}{2} \qquad (4.20)$$

$$Q_{exe} = \frac{2\pi f_0^e \cdot \tau_{S11e}(f_0^e)}{2} \qquad (4.21)$$

where

$$\tau_{S11o}(f) = -\frac{\partial \varphi_{S11o}(f)}{(2\pi)\partial f} \qquad (4.22)$$

$$\tau_{S11e}(f) = -\frac{\partial \varphi_{S11e}(f)}{(2\pi)\partial f} \qquad (4.23)$$

where $\tau_{S11o}(f)$, $\tau_{S11e}(f)$ are group delays of odd and even modes; $\varphi_{S11o}(f)$ and $\varphi_{S11e}(f)$ denote the phase responses of the input reflection coefficient of odd and even mode. A typical group delay response of input reflection coefficient of odd-mode is shown in Figure 4-8.

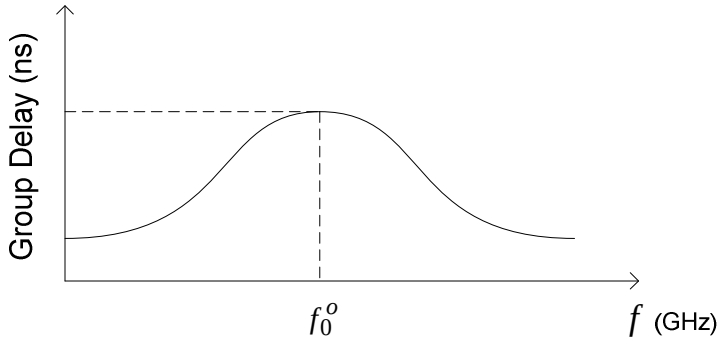


Figure 4-8. The typical group delay response of input reflection coefficient of odd-mode.

To maintain the shape and bandwidth of odd-and even-mode frequency response over the entire tuning range, $Q_{exo}$ and $Q_{exe}$ of the proposed tunable filter must satisfy equations (4.2) and (4.3) and this may be achieved by properly choosing the transformer parameters $w_{11}$, $l_1$, $s$ and $C_s$ shown in Figure 4-7. In general, for given $l_1$, which depends on the contour of the open loop, a stronger coupling can be obtained with a smaller $s$. In addition, the coupling turns to be more inductive and can be enhanced with a narrower $w_{11}$ and larger $C_s$.

It should be mentioned that the reason for using full-wave EM simulation to extract the design parameters, i.e., the resonant frequency of odd-mode ( $f_0^o$ ) and even-

mode ( $f_0^e$ ), and the external quality factor of odd-mode ( $Q_{exo}$ ) and even-mode ( $Q_{exe}$ ) is to include parasitic effects such as right-angle bend parasitics, open-end fringing, via-hole inductance, and even unwanted cross coupling between nonadjacent transmission lines. These parasitic effects are difficult to be taken into account by the ideal electrical circuit modeling. However, for the initial design and characterizing the proposed dual-mode filter, the electrical circuit modeling is useful and given in the Appendix.

#### *4.2.1.4 Design procedure*

- *Step1: Determine of the requirements of the ideal tunable dual-mode filter:* The requirements of the ideal tunable filter may be derived from its fix frequency response centring at the high frequency edge of a given tuning range. The separation (A) of the odd-and even-mode resonant frequencies and the required $Q_{exo}$ and $Q_{exe}$ for the ideal tunable filter then can be determined from (4.1)-(4.3).

- *Step2: Design of Transformer Network:* To maintain the shape and bandwidth of odd-and even-mode frequency response over the tuning range, $Q_{exo}$ and $Q_{exe}$ of the proposed tunable filter given in (4.20) and (4.21) must satisfy (4.2) and (4.3) by properly choosing the transformer parameters $w_{11}$, $l_1$, $s$ and $C_s$.

- *Step 3: Design of the even-mode tuning rate:* The tuning rate of the even mode may be designed to match the tuning rate of the odd mode by using (4.16) and (4.17) with B=A for the constant absolute bandwidth tuning. As there are six degrees of freedom to determine the tuning rate of even-mode i.e. $w_3$, $l_3$, $w_4$, $l_4$, $w_5$, and $l_5$, four parameters may be chosen first, and then the last two can be determined by (4.16) and (4.17). Since the purpose of using $w_4$, $l_4$, $w_5$, and $l_5$ is to shorten the length of the even mode within the square loop of the odd mode (see Figure 4-1), these parameters may be chosen first.

To go through the design procedure, two examples are given below.

### *4.2.2 Design example_ Tunable filter with finite-frequency transmission zero located at high side of the passband (Filter A)*

The proposed filter has been designed using microstrip lines with the following specifications:

| | |
|---|---|
| Tunable range: | 0.6~1.07 GHz |
| Fractional bandwidth (FBW) | 2.9% at 1.07 GHz |
| Number of poles: | 2 |

To derive the required design parameters for the tunable filter, a filter centring at 1.07 GHz has been designed firstly with a finite-frequency transmission zero located at 1.12 GHz, a fractional bandwidth of 2.9% and passband return loss of 20 dB. The desired parameters may be derived from a target coupling matrix corresponding to the prescribed response by using the method given in Section 4.2.1.1, which results $f_0^o = 1.053$ GHz; $f_0^e = 1.098$ GHz; $Q_{exo} = 27.2$ and $Q_{exe} = 105.2$ . With these design parameters, the desired values for the ideal tunable filter are derived according to (4.1)-(4.3) and plotted in Figure 4-9 using the full line. The proposed tunable filter can be designed in light of full-wave EM simulation. By comparing the extracted $Q_{exo}$ $Q_{exe}$ $f_0^o$ and $f_0^e$ from EM simulation (see Section 4.2.1.3) with the desired ones from target coupling matrix, the dimensions of the dual-mode filter can be determined. For our example, a substrate with dielectric constant of 10.2 and thickness of 1.27 mm is used. The odd-mode resonator is formed using a 50-Ω line, which has a tuning rate as that shown in Figure 4-4. Although it is possible to use other characteristic impedance line, the resultant tuning rate will be different. The loading capacitance $C_v$ is chosen to be 0.6 pF. The electrical length of odd-mode resonator can then be determined initially for $f_0^o = 1.053$ GHz. To achieve desired values for $Q_{exo}$ and $Q_{exe}$ , obtained from (4.2) and (4.3), respectively, as shown (full line) in Figure 4-9(a), the transformer parameters, i.e. $w_{11}$ , $l_1$ , $s$ and $C_s$ are chosen, so that the extracted external quality factors from (4.20) and (4.21) could best satisfy those desired over the tuning range. The resultant extracted $Q_{exo}$ and $Q_{exe}$ are also plotted (dot line) in Figure 4-9(a). The parameters for the even mode, i.e., $w_3$ , $l_3$ , $w_4$ , $l_4$ , $w_5$ and $l_5$ are

derived based on (4.16) and (4.17) with B = A, so that the resonant frequencies of the odd mode and even modes can be shifted proportionally. Initially, $w_4$, $l_4$, $w_5$, and $l_5$ were chosen as 4, 8, 1, and 1 mm, respectively. After that, $w_3$ and $l_3$ are determined from (4.16) and (4.17). Note that $w_4, l_4$, $w_5$, $l_5$ may be readjusted so that the loading elements of even-mode are within the square-loop of odd mode. The plot of the separation of the odd-and even-mode resonant frequencies is displayed in Figure 4-9(b).

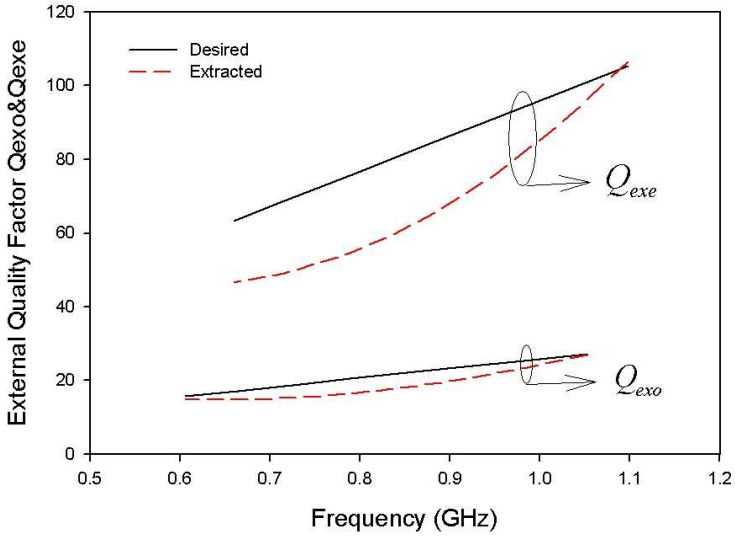


(a)

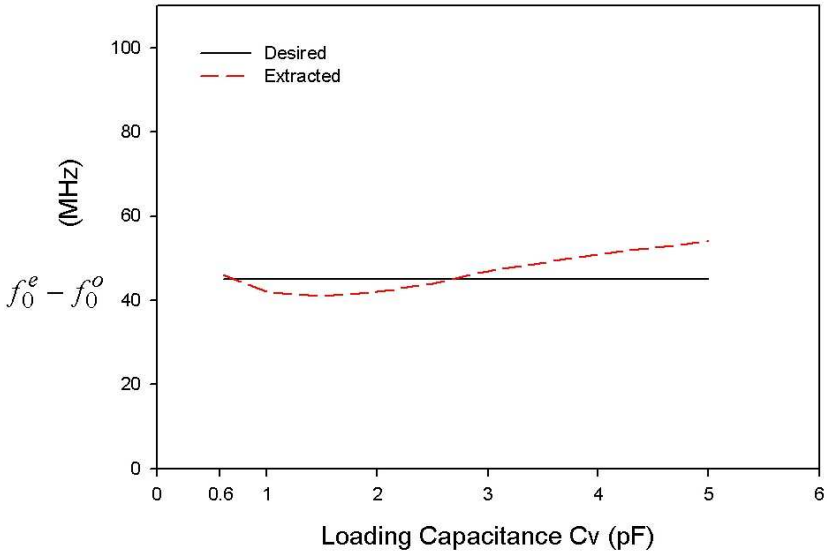


(b)

Figure 4-9. (a) External quality factor $Q_{exe}$, $Q_{exo}$ and (b) $f_0^e - f_0^o$ of the desired and extracted proposed tunable filter (Filter A).

It is shown that the resonant frequencies of odd mode and even modes are shifted nearly proportionally after the tuning rate of the even mode is modified. Note that the extracted result of Figure 4-9(b) was obtained by EM simulation and with the I/O structure, whereas the result shown in Figure 4-5 was obtained from the theory without considering the I/O coupling. Nevertheless, they all showed that both modes can be tuned proportionally over a certain tuning range.

The parameters for the final layout of the proposed tunable filter, as referring to Figure 4-1, is given in Table 4-1.

**TABLE 4-1**

**Parameters of the proposed tunable dual-mode filter (Filter A) (in millimeters) (see Figure 4-1)**

| $w_{11}$ | $w_2$ | $w_3$ | $w_4$ | $w_5$ | $w_{12}$ |
|---|---|---|---|---|---|
| 0.2 | 0.7 | 0.5 | 0.3 | 1.2 | 1.0 |
| $l_1$ | $l_2$ | $l_3$ | $l_4$ | $l_5$ | $s$ |
| 17.7 | 12.7 | 13 | 8.5 | 2 | 0.2 |
| $C_s$ | 2.8 pF | | $C_v$ | 0.6 to 5.0 pF | |

Full-wave EM simulated responses of the filter are present in Figure 4-10. It can be seen that, the tunable filter exhibits a nearly constant 3-dB absolute-bandwidth ($80 \pm 5$ MHz), and its centre frequency is tuned from 0.6 to 1.03 GHz with the capacitance $C_v$ of loading varactors changes from 5.0 to 0.6 pF. To demonstrate this type of tunable filter experimentally, the designed filter is fabricated as shown in Figure 4-11 with an overall circuit size of 15.5 mm×19.3 mm. The matching capacitance $C_s$ is realized by AVX chip capacitor [84], while the variable capacitance $C_v$ is implemented by M/A COM MA46H202 varactor [85]. In this case, three varactors are used, which are applied by a

single DC bias circuit. The measured results for a DC bias ranging from 2.2 V to 22.0 V are also plotted in Figure 4-10, which are obtained using Agilent 8510B network analyzer. From Figure 4-10, we can observe that the measured tunable characteristics are in good agreement with the simulated ones. The experimental varactor-tuned bandpass filter shows high selectivity on high side of the passband with less than 1.8 dB insertion loss and more than 10 dB return loss over a tuning range of 41% from 0.6 to 1.03 GHz. The measured 3-dB bandwidth is $85 \pm 5$ MHz.

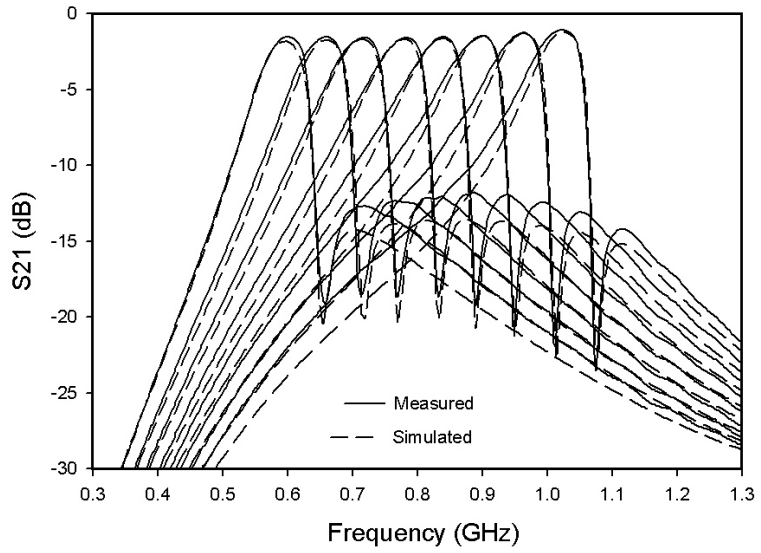


(a)

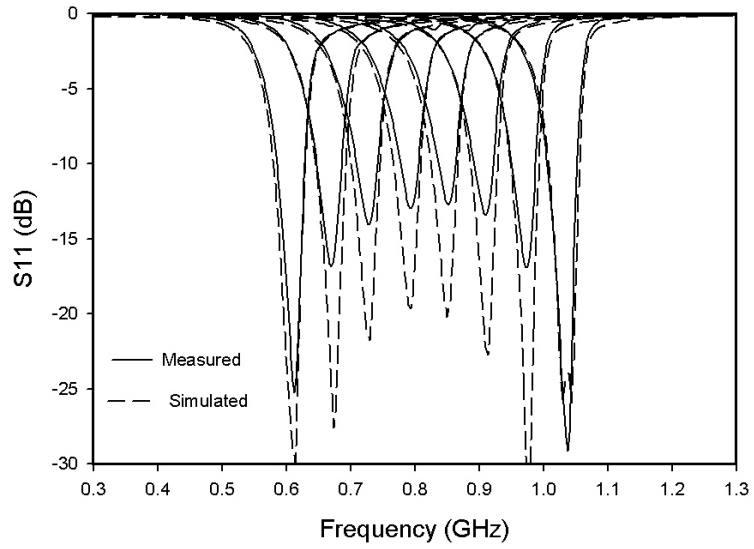


(b)

Figure 4-10. Measured and EM simulated S-parameters of the proposed filter (Filter A). (a) $S_{21}$ and (b) $S_{11}$. The bias voltage is between 2.2-22V. The 3-dB absolute-bandwidth is $85 \pm 5$ MHz from 0.6 to 1.03 GHz.

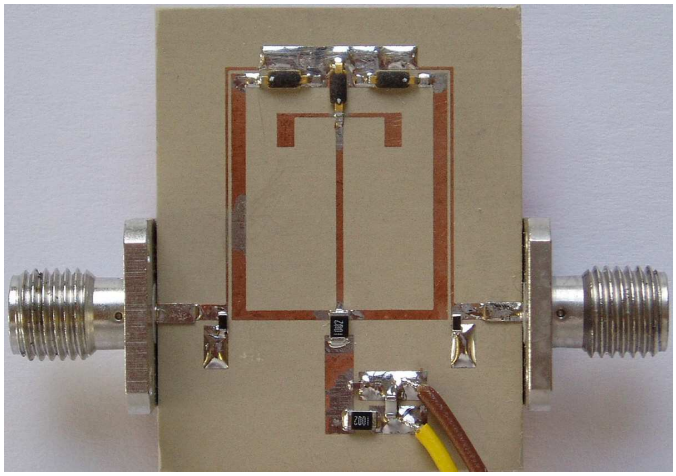

Figure 4-11. Photograph of the fabricated proposed filter (Filter A).

A further discussion is made here on the design. From Figure 4-9(a), it can be seen that the $Q_{exe}$ does not meet the ideal values after the even-mode tuning rate being modified. This is because the parameters of the even mode have the effects on both $Q_{exe}$ and the tuning rate. Therefore, there is a trade-off in the design, and as a result, the designed bandwidth would be slightly different from the desired specification. However, the bandwidth can be readjusted by slightly varying the even-mode resonant frequency. Comparing Figure 4-9(a) and (b), it can be seen that when the extracted $Q_{exe}$ is smaller (the coupling to the even mode being stronger), the separation between the odd- and even-mode frequencies is smaller, which thus minimizes the variation of the 3-dB bandwidth at these frequencies within the tuning range. In addition, it is recommended to design the filter with a slightly larger bandwidth than the required specification.

### *4.2.3 Design example_ Tunable filter with finite-frequency transmission zero located at low side of the passband (Filter B)*

Filter B can be designed following the same design procedure as filter A. The layout of filter B is present in Figure 4-12.

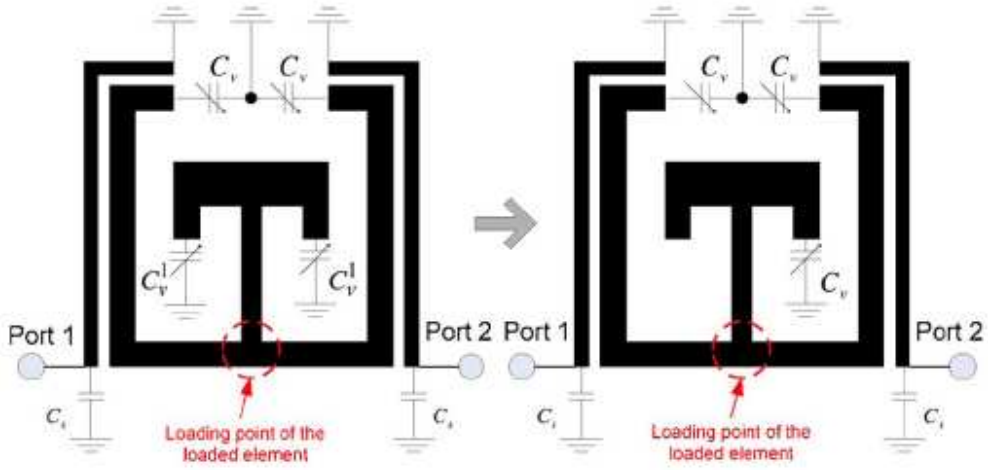


(a) (b)

Figure 4-12. Layout of filter B. (a) with symmetrical structure and (b) with asymmetrical structure (dimensions refer to Figure 4-1).

It should be noticed that the location of loaded varactor for the even mode is different from that of filter A. This is because the resonant frequency of the even mode of filter B is required to be lower than that of the odd mode in order to produce a finite frequency transmission zero located at low side of the passband. By employing the similar design procedure, filter B with a symmetrical varactor loading structure can be designed. The filter parameters are listed in Table 4-2.

**TABLE 4-2**

**Parameters of the proposed tunable dual-mode filter (Filter B) (in millimeters) (see Figure 4-1)**

<table>
<tr><td>$w_{11}$</td><td>$w_2$</td><td>$w_3$</td><td>$w_4$</td><td>$w_5$</td><td>$w_{12}$</td></tr>
<tr><td>0.2</td><td>0.7</td><td>0.3</td><td>0.5</td><td>0.3</td><td>1.0</td></tr>
<tr><td>$l_1$</td><td>$l_2$</td><td>$l_3$</td><td>$l_4$</td><td>$l_5$</td><td>$s$</td></tr>
<tr><td>17.7</td><td>12.7</td><td>14</td><td>6.5</td><td>3.9</td><td>0.2</td></tr>
<tr><td rowspan="2">$C_s$</td><td colspan="2" rowspan="2">2.8 pF</td><td rowspan="2">$C_v$</td><td colspan="2">0.41 to 2.95 pF (sym.)</td></tr>
<tr><td colspan="2">0.6 to 5.0 pF (asym.)</td></tr>
</table>

In order to reduce the number of varactors, filter B with an asymmetrical varactor loading structure can then be developed from the designed symmetrical one. A symmetrically loaded element for the even mode can have an equivalent asymmetrically loaded element as long as the loading point is symmetrical with respect to the I/O ports (see Figure 4-12). Both designs result in the same filtering responses as shown in Figure 4-13. In this case, the only difference between the two designs, i.e., symmetrical and asymmetrical, is the loading capacitance for the even mode, as indicated in Table 4-2.

While the extracted external quality factors for both modes are similar to that of Figure 4-9(a), the extracted even–odd-mode separation with respect to the loading capacitance $C_v$ shows a different characteristic, as illustrated in Figure 4-14. The 3-dB bandwidth of filter B has a larger variation than filter A, the reason is that when the coupling to even mode is stronger, the frequency separation is larger as well, resulting in a larger 3-dB bandwidth.

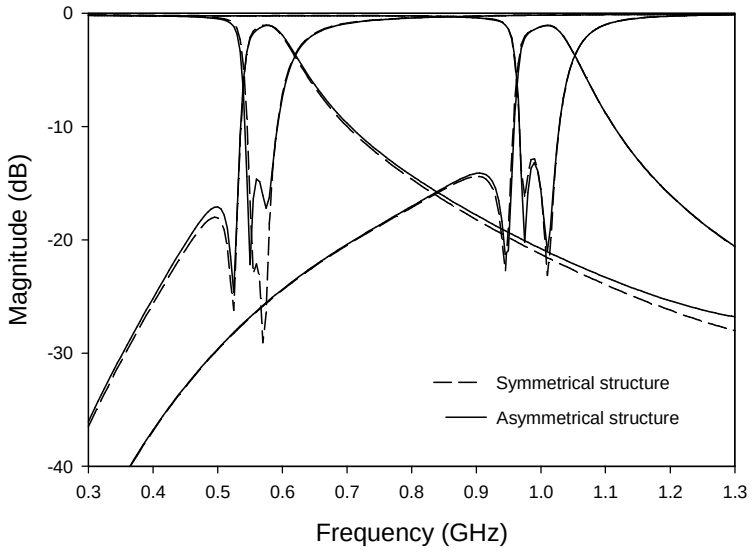


Figure 4-13. The EM simulated performance of filter B with symmetrical structure and asymmetrical structure.

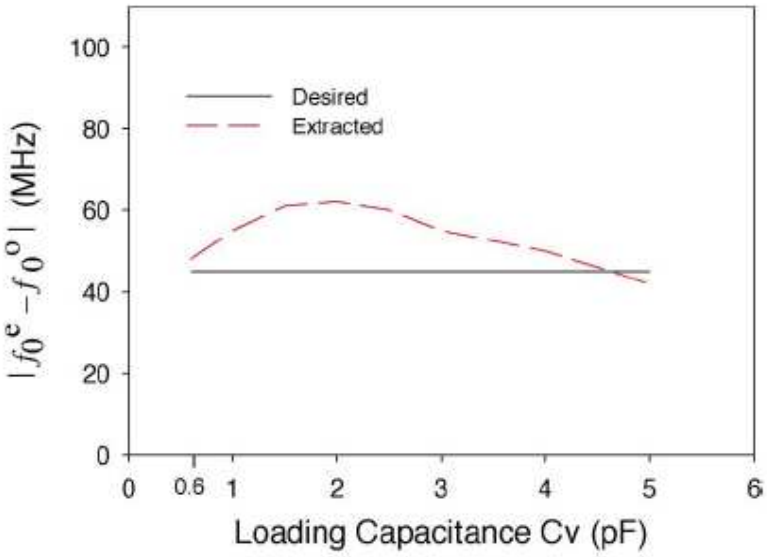


Figure 4-14. Desired and extracted $\left|f_0^e - f_0^o\right|$ for the proposed tunable filter (filter B).

The experimental filter for filter B, fabricated using the same substrate as that for filter A, is shown in Figure 4-15 with an overall circuit size of 15.5 mm×18.5 mm. It is EM-simulated and measured responses are displayed in Figure 4-16. From Figure 4-16, it can be seen that the measured tunable characteristics are similar to the simulated ones. The experimental varactor-tuned bandpass filter shows a high selectivity on the lowside of the passband with less than 2.2-dB insertion loss and more than 10-dB return loss over a tuning range of 41% from 0.57 to 0.98 GHz. The applied bias voltage is between 2.2–22.0 V. The measured 3-dB bandwidth is 91 ± 6 MHz over the tuning range.

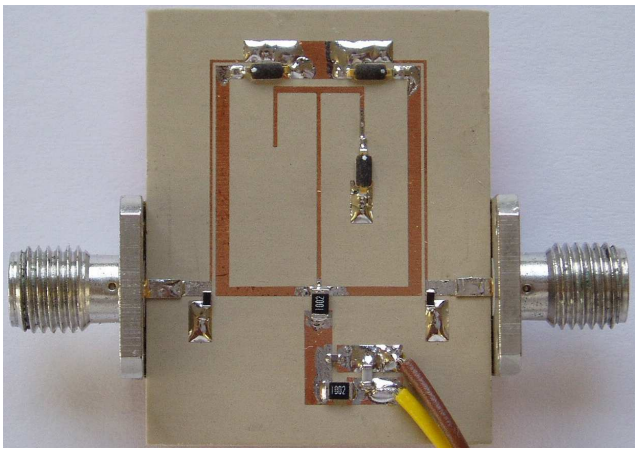

Figure 4-15. Photograph of the fabricated proposed filter (Filter B).

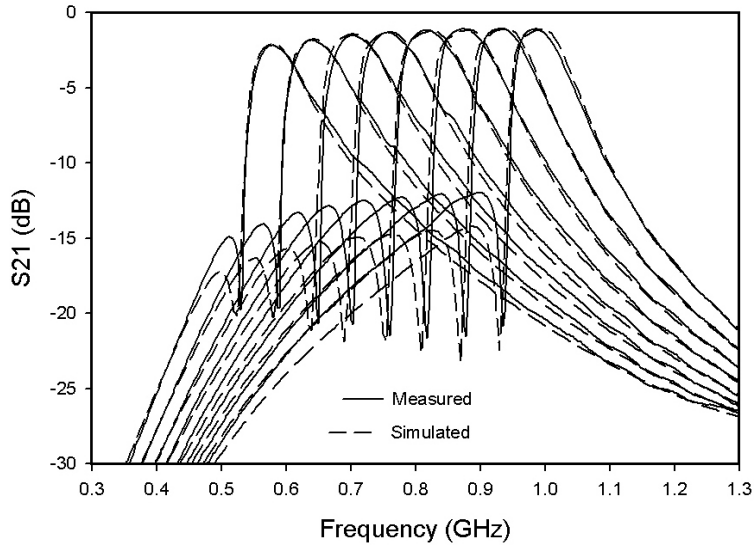


(a)

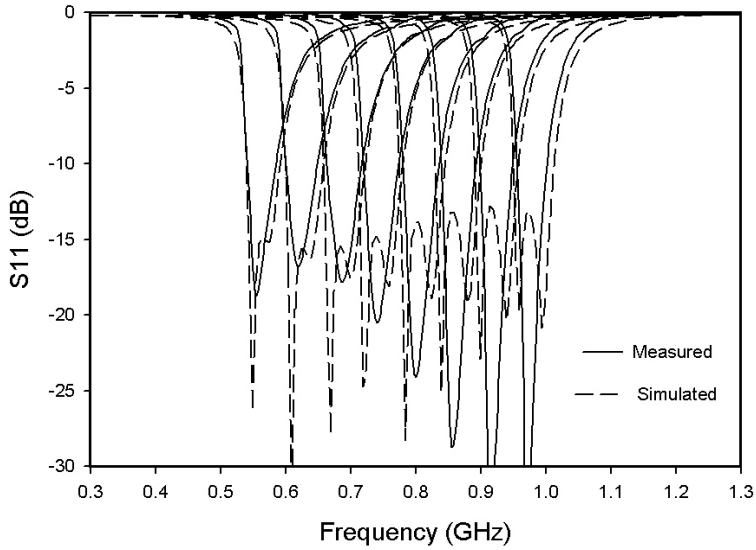


(b)

Figure 4-16. Measured and EM simulated S-parameters of the proposed filter (Filter B). (a) $S_{21}$ and (b) $S_{11}$. The bias voltage is between 2.2-22V. The 3-dB absolute-bandwidth is $91 \pm 6$ MHz from 0.57 to 0.98 GHz.

## 4.3 Four-Pole Varactor-Tuned Dual-Mode Bandpass Filters with Quasi-Elliptic Function Response

The two-pole dual mode tunable filter, consisting only one dual-mode resonator, exhibits high selectivity on either side of passband (see Section 4.2). In order to obtain a

quasi-elliptic function response, two dual-mode resonators can be cascaded through nonresonating nodes [86] to build up a four-pole filter of this type. Two transmission zeros, located on each side of the passband, are inherently associated with the even-modes of the dual-mode resonators, thus, when the two even-mode frequencies are tuned, the associated transmission zeros shift accordingly, resulting in a tunable quasi-elliptic function response.

### *4.3.1 Filter structure and operation*

Figure 4-17 shows a layout of the proposed four-pole dual-mode tunable filter, Variable capacitances C are supposed to be loaded varactors. These six same varactors are to be used with a single DC bias circuit, which makes both the implementation and tuning simple.

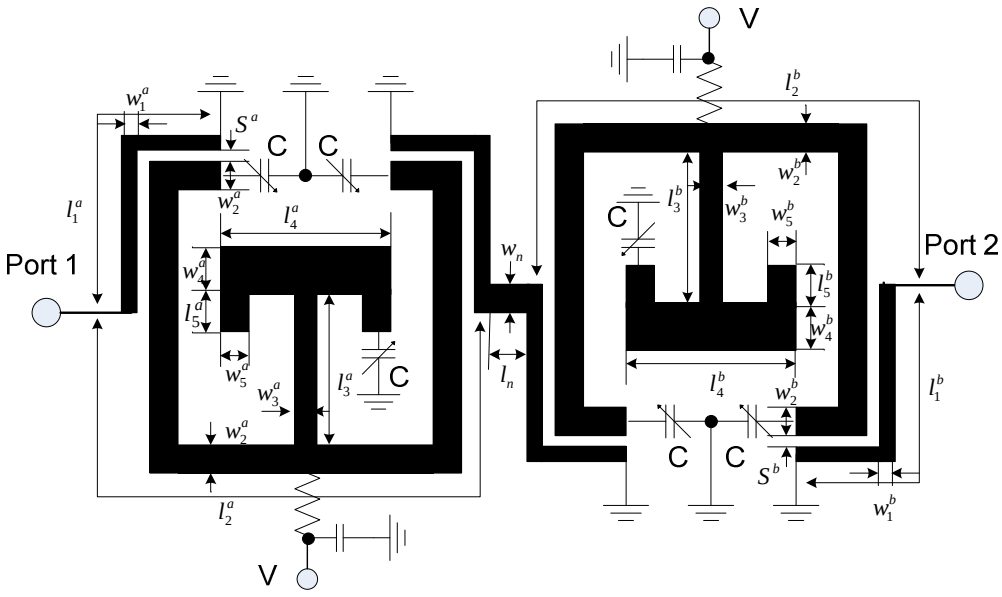


Figure 4-17. Layout of the four-pole dual-mode tunable filter.

The proposed four-pole dual-mode filter has a coupling scheme as shown in Figure 4-18, where S and L denote the input and output ports respectively; node 1, 3 denote the odd-mode and node 2, 4 denote the even-mode. N denotes the nonresonating nodes [86]. Because the four operating modes do not couple and the two nonresonating nodes can be considered as frequency independent for narrow band filters, this leads to a simple tuning scheme, that is, to tune all modal frequencies proportionally to maintain

the passband shape when the centre frequency of the proposed filter is tuned. How to achieve this is discussed as follow.

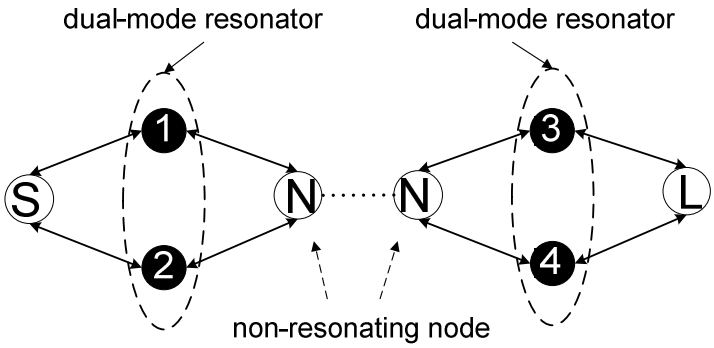


Figure 4-18. The coupling scheme of the four-pole dual-mode filter.

### *4.3.2 Four-pole dual-mode tunable filter design*

To design the proposed four-pole tunable filter, two steps may be applied.

- Step 1—to design two two-pole dual-mode tunable filters, one with a finite-frequency transmission zero on lowside of the passband (filter A) and the other with a finite-frequency transmission zero on highside of the passband (filter B), respectively.
- Step 2—to cascade the two-pole filters obtained from the step 1 using a non-resonating node structure in between.

The two-pole tunable filter can be designed by employing the design method given in Section 4.2. By properly choosing the parameters of input/output transformer and the loading elements (see Figure 4-17), the external quality factors of odd and even mode and the odd-and even-mode tuning rates could be best satisfied the desired ones according to (4.1)-(4.3). Notice that in order to achieve a good return loss of the cascaded proposed filter, the frequency response of the two two-pole filter must be matched to each other over the tuning range as shown in Figure 4-19, which are simulated using full-wave EM simulation tool [79].

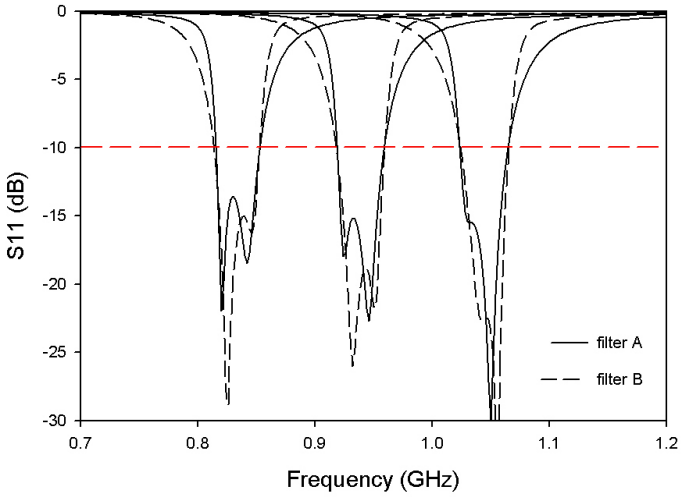


(a)

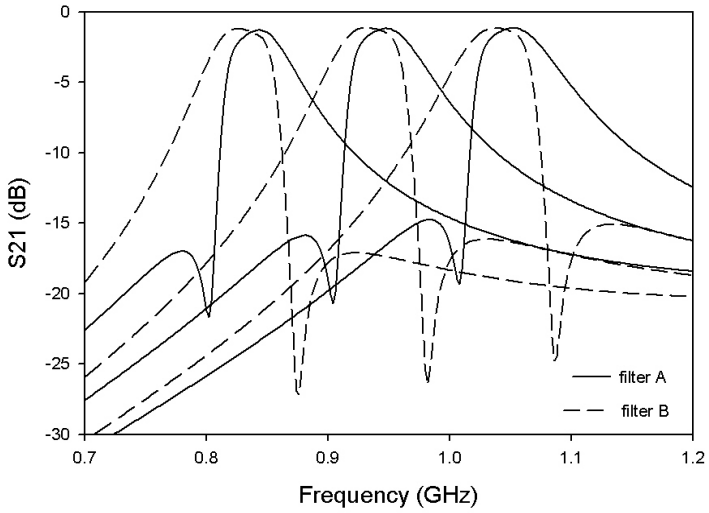


(b)

Figure 4-19. EM-simulated performance of the two two-pole filters. (a) S11. (b) S21.

From Figure 4-19(a), it is clear that the return loss of filter A and filter B are well matched at about 10 dB. A 50-Ω line is then used to connect the two designed two-pole tunable filters to form the proposed four-pole tunable filter. The length of the connecting line is chosen as short as possible, however, coupling between the four resonant modals will be introduced when filter A and filter B are placed too close. This coupling can deteriorate the performance of the cascaded filter. Notice that, in order to reduce this unwanted coupling, the orientation of filter A and filter B is opposite (see Figure 4-17). The final layout of the proposed four-pole dual-mode filter is given in Table 4-3 and its frequency responses are presented in Figure 4-20 by performing full-wave EM simulation. As can be seen, the tunable filter exhibits a quasi-elliptic function

response over a tuning range of 20% from 0.83 to 1.04 GHz when the capacitance C of loading varactors changes from 2.0 to 0.6 pF. The simulated 3-dB absolute bandwidth is $41 \pm 1.5$ MHz over the entire tuning range.

**TABLE 4-3**

**Parameters of the proposed four-pole tunable dual-mode filter ( (in millimeters) (see Figure 4-17)**

| $w_1^a$ | $w_2^a$ | $w_3^a$ | $w_4^a$ | $w_5^a$ | $w_1^b$ | $w_2^b$ | $w_3^b$ | $w_4^b$ | $w_5^b$ |
|---|---|---|---|---|---|---|---|---|---|
| 0.2 | 1.2 | 0.3 | 1.0 | 1.2 | 0.2 | 1.0 | 0.7 | 1.0 | 1.2 |
| $l_1^a$ | $l_2^a$ | $l_3^a$ | $l_4^a$ | $l_5^a$ | $l_1^b$ | $l_2^b$ | $l_3^b$ | $l_4^b$ | $l_5^b$ |
| 14.5 | 22.1 | 12.5 | 7.9 | 1.4 | 14.5 | 23.1 | 13.3 | 7.9 | 1.5 |
| C | 0.6 to 2.0 pF | | | | | | | | |

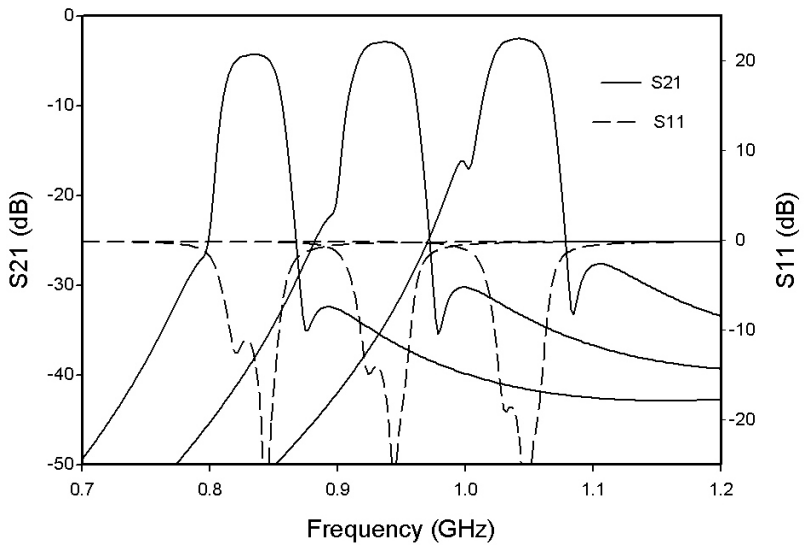


Figure 4-20. EM-simulated performance of the proposed four-pole tunable filter.

### *4.3.3 Fabrication and measurements*

To demonstrate this type of tunable filter experimentally, the filter is fabricated on a substrate with a relative dielectric constant of 10.2 and a thickness of 1.27 mm as shown in Figure 4-21. The variable capacitance C is implemented by M/A COM MA46H202 varactor [85] which is applied by a single DC bias circuit. The measured results are plotted in Figure 4-22, which are obtained using Agilent 8510B network analyzer. From Figure 4-22, we can observe that the experimental four-pole tunable bandpass filter exhibits two finite-frequency transmission zeros on each side of the passband, which is similar to the simulated ones. The measured centre frequency is tuned from 0.83 to 1.01 GHz when the DC bias varies from 6.7 to 22 V with the return loss is better than 10 dB. The measured 3-dB absolute bandwidth is $30 \pm 1.6$ MHz over the entire tuning range. The overall circuit size of the filter is 35.6 mm×25.7 mm.

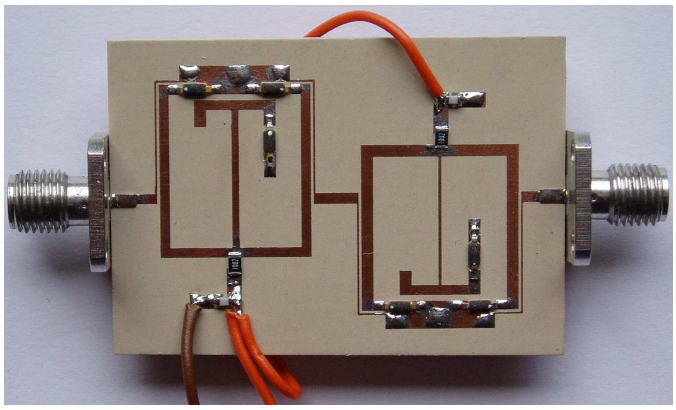

Figure 4-21. Photograph of the fabricated proposed filter.

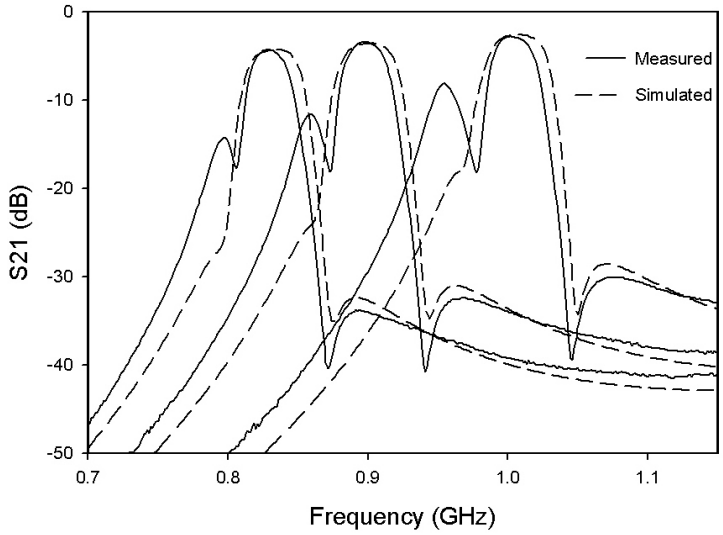


(a)

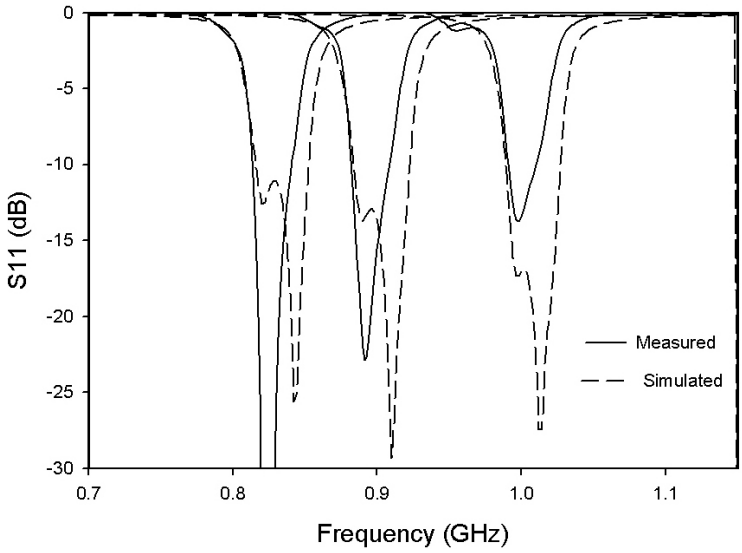


(b)

Figure 4-22. Measured and EM simulated S-parameters of the proposed four-pole tunable filter. (a) S21 and (b) S11. The bias voltage is between 6.7-22 V. The 3-dB absolute-bandwidth is $30 \pm 1.6$ MHz from 0.83 to 1.01 GHz.

Discussion:

The side lob of the four-pole tunable filter on lowside of the passband (see Figure 4-22(a)) may be due to the non-ideal of the nonresonating node, which actually has a resonant peak at about 1.6 GHz (see Figure 4-23). To minimize this effect, a possible solution is using two layers with ground plane inserted between the two two-pole filters,

the connecting line can be implemented by a via, so that the length of the connecting line is minimized, resulting in a better performance of the proposed four-pole filter.

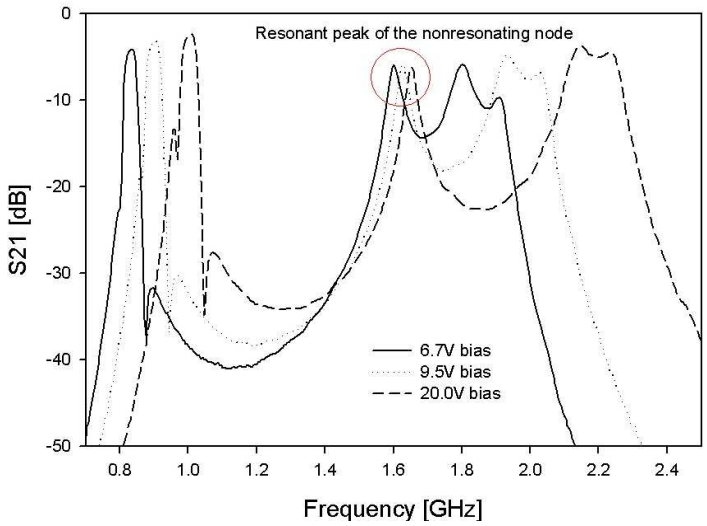


Figure 4-23. Measured harmonic responses of the four-pole tunable filter.

## 4.4 Summary

A new type of varactor-tuned dual-mode microstrip open-loop resonator bandpass filter has been investigated for a constant absolute bandwidth tuning. This type of filter can be tuned in a simple manner by controlling the resonant frequencies of the odd-mode and even-mode since these two operating modes do not couple. In order to tune this type of dual-mode filter by using a single DC bias circuit and to achieve constant absolute bandwidth over a broad tuning range, a wideband input/output transformer network and odd/even-mode tuning rate method have been introduced. Design equations and design procedures have been presented. By applying the design procedures, two two-pole tunable bandpass filters with opposite asymmetric responses and a four-pole tunable bandpass filter with quasi-elliptic function response have been demonstrated with both simulated and experimental results. Good agreement between simulation and measurement is obtained.

# Chapter 5

# DUAL-MODE FILTERS WITH NOVEL CONFIGURATIONS

## 5.1 Introduction

Figure 5-1(a) shows a new type of miniature dual-mode microstrip open-loop resonator [10]. The miniature dual-mode resonator can be used as a doubly tuned resonant circuit, and therefore the number of resonators required for a given degree of filter is reduced by half, resulting in a compact filter configuration.

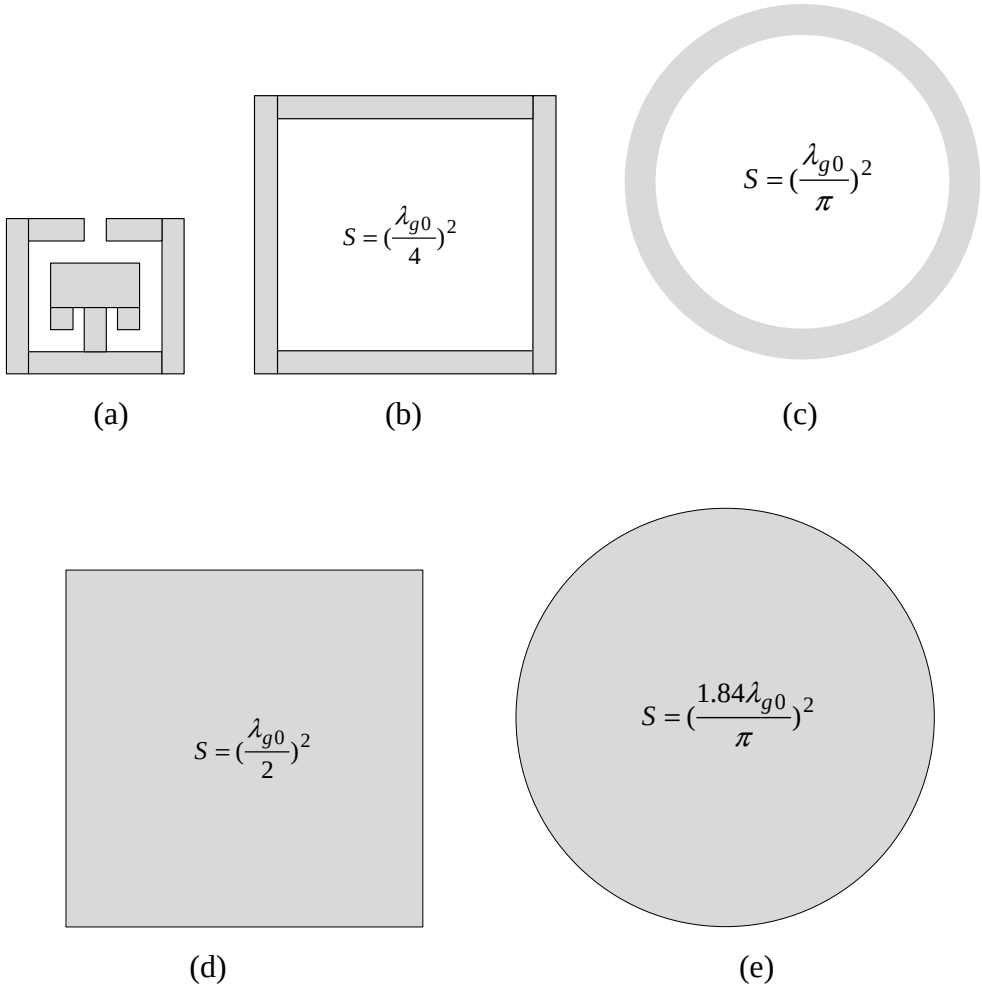


Figure 5-1. (a) Miniature dual-mode resonator. (b) Square loop dual-mode resonator. (c) Ring dual-mode resonator. (d) Square patch dual-mode resonator. (e) Disk patch dual-mode resonator. (where $S$ denotes the circuit surface area, $\lambda_{g0}$ is the guided wavelength at resonant frequency [5].)

Moreover, as compared with the size of the conventional dual-mode square loop resonator; ring resonator; square patch resonator and disk patch resonator of Figure 5-1(b-e) [5], the size of dual-mode open-loop resonator is only about 25% of the square loop resonator; 18% of the ring resonator and 12% of the square/disk patch resonator, which is a significant size reduction and make this type of miniature dual-mode resonator attractive filter applications.

By employing a tapped line feed structure into the miniature dual-mode resonator, double behaviour of the dual-mode resonator can be obtained, which forms a new class of miniature dual-mode filters that exhibits quasi-elliptic function response without any cross coupling. This will be discussed in Section 5.2.

Parallel feed configuration of the dual-mode resonators has also been investigated, which leads to a lower insertion loss and a better midband of passband performance than the reported work [10], with a trade-off of less rejection level in the stopband. Moreover, by relocating the modal frequencies, a dual-band operation of the proposed parallel feed filter can be obtained. The design procedure of this type of filter will be given in Section 5.3.

To further reduce the size of the miniature dual-mode resonator, a slow-wave technique is employed to achieve a new type of dual-band dual-mode slow-wave open-loop resoantor filters. Flexible filtering characteristics can be obtained by using different feed schemes. This will be addressed in Section 5.4.

## 5.2 Quasi-Elliptic Function Doublet Filters without Cross Coupling

This section presents the latest results of an investigation of new doublet filter comprised of a single miniature dual-mode open-loop resonator. By introducing a tapped line feed structure, the filter exhibits a double behaviour that not only supports two trnasmission poles in the passband, but also facilitates two transmission zeros at finite frequency, resulting in a quasi-elliptic function response without any cross coupling.

The filter operation and design method of this new class of miniature doublet filters are discussed as follows.

### *5.2.1 Doublet dual-mode filter operation*

Figure 5-2(a) shows the layout of a proposed doublet filter consisting of a single microstrip dual-mode open-loop resonator. The resonator is excited by two ports with asymmetrical arrangements. The port 1 has a tapped line feed structure, whereas the port 2 uses a coupled line feed structure. The filter is simulated with a commercially available full-wave electromagnetic (EM) simulator [79] and the result is plotted in Figure 5-2(b). As can be seen the filter exhibits a two-pole quasi-elliptic function response centered at 1.04 GHz with two finite-frequency transmission zeros (TZs) allocating at 0.935 and 1.165 GHz, respectively.

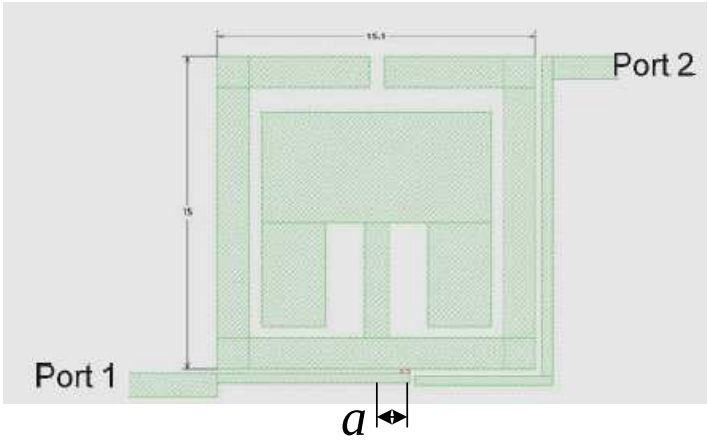


(a)

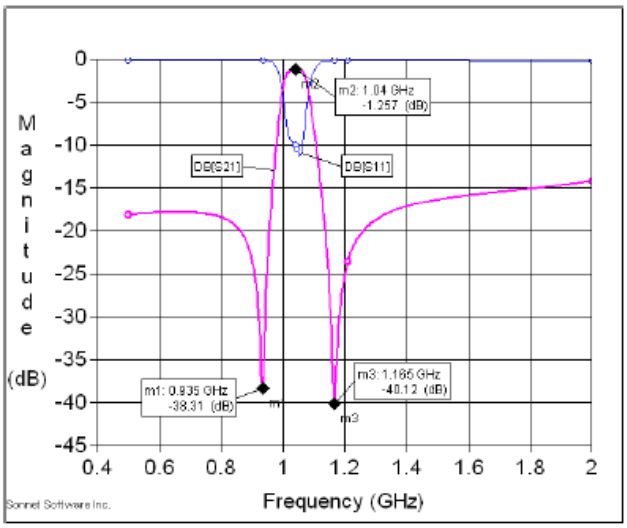


(b)

Figure 5-2. (a) The proposed doublet dual-mode filter. (b) EM simulated performance.

To understand the operation of the doublet and the mechanism of generating the transmission zeros, a coupling structure of Figure 5-3(a) is first studied, where the nodes 1 and 2 indicate the resonant modes 1 and 2 of the dual-mode resonator, and S and L denote the source (port 1) and load (port 2), respectively.

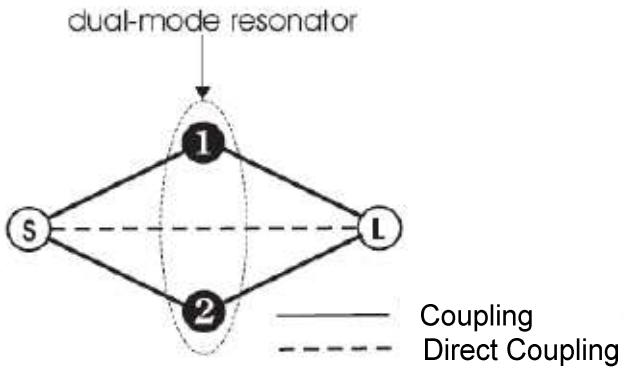


(a)

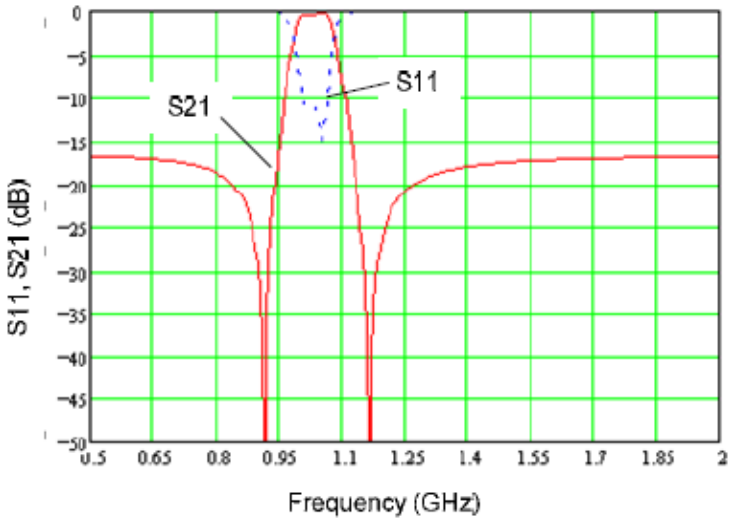


(b)

Figure 5-3. (a) A possible doublet coupling structure. (b) Computed response.

For this doublet coupling structure, a direct coupling between the source and load is assumed. The coupling matrix for this structure is given by (5.1)

$$M = \begin{bmatrix} 0 & ms1 & ms2 & MsL \\ ms1 & m11 & 0 & mL1 \\ ms2 & 0 & m22 & mL2 \\ MsL & mL1 & mL2 & 0 \end{bmatrix} \qquad (5.1)$$

The transmission coefficient S21 and reflection coefficient S11 of the coupling matrix can be calculated by (4.5) and (4.6). The associated element values for a possible solution of (5.1) are $ms1 = 0.65$, $ms2 = 0.84$, $m11 = -1.05$, $m22 = 1.58$, $mL1 = -0.75$, $mL2 = 0.58$, and $MsL = -0.075$. Figure 5-3(b) plots the computed response, which would show a good agreement with the simulated response of Figure 5-2(b).

For this coupling structure, the transmission zeros are attributed to the direct coupling between the source and load, and hence the TZ locations strongly depend on the strength of this direct coupling. However, when we change the coupling between the source and load using the two alternative output (port 2) feed arrangements shown in Figure 5-4(a) and (b), it is found from the EM simulation that the TZs are entirely independent of the coupling between the source and load as shown in Figure 5-4(c).

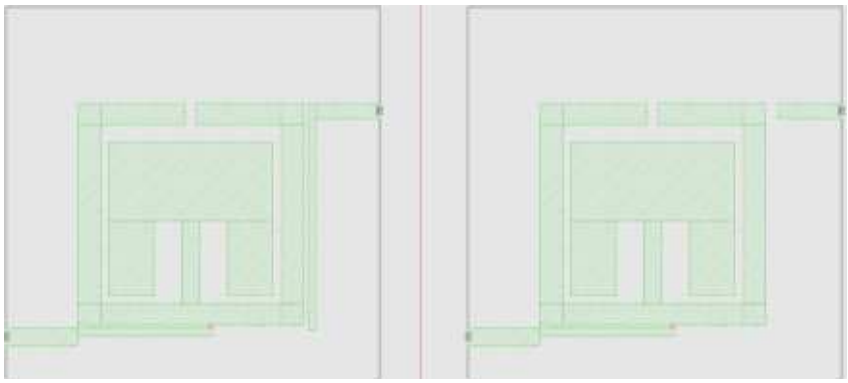

(a) (b)

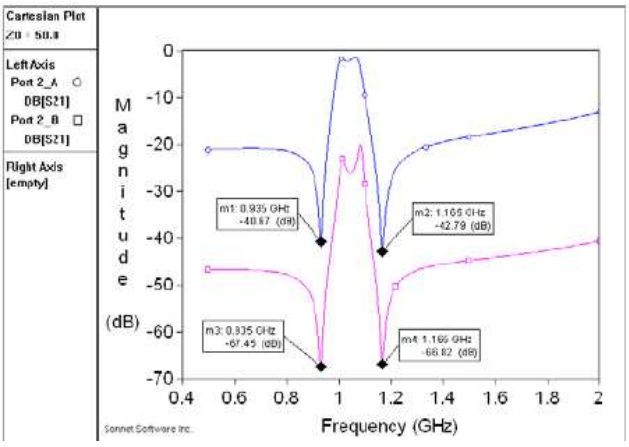


(c)

Figure 5-4. (a) The doublet filter with a weak coupling to the load (Port 2_A). (b) The doublet filter with a much weaker coupling to the load (Port 2_B). (c) Simulated responses.

This implies that the occurring of the two TZs for the proposed doublet filter should be attributed to something else but not the source and load coupling. Furthermore, since the couplings from the load to mode 1 (mL1), and from the load to mode 2 (mL2) change too for the port 2 arrangements in Figure 5-4(a) and (b), the results of Figure 5-4(c) also suggest that the TZs are independent of mL1 and mL2 as well.

In order to find out the mechanism that produces the two TZs in the proposed doublet dual-mode filter, the EM simulations are performed to obtain the field distributions of the doublet filter at the frequencies of the two TZs. Figure 5-5 shows the current distributions when the port 1 is excited. Now, it becomes clear that at a TZ's frequency, there is a resonance associated with the even mode of the dual-mode open-loop resonator, as shown in Figure 5-5(a). And, at the other TZ's frequency a resonance occurs in association with the odd mode as shown in Figure 5-5(b).

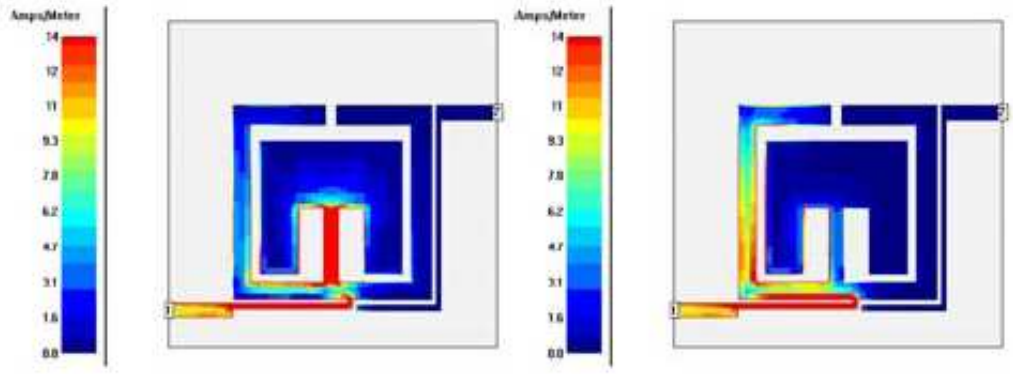

(a) (b)

Figure 5-5. Current distribution of the proposed doublet filter. (a) at the first TZ frequency of 0.935 GHz. (b) at the second TZ frequency of 1.165 GHz.

It appears that these two resonances produce a short circuit along the feed line of the port 1, and hence block the signal transmission leading to the transmission zeros observed at these two frequencies. This suggests that microstrip dual-mode open-loop resonator associated with the tapped line feed structure has a double behaviour that not only supports two transmission poles in the passband, but also facilitates two transmission zeros at finite frequencies.

According to the analysis above, the additional transmission zero located at 1.165 GHz may be produced by extracted attenuation pole [1]. The circuit model of the proposed doublet filter can be derived as shown in Figure 5-6. Where $L_o$ and $C_o$ denote shunt parallel-type resonator that represents odd mode. $L_e$ and $C_e$ denote shunt parallel-type resonator that represents even mode. $L(a)$ and $C(a)$ denote shunt series-type resonator that represents an extracted attenuation pole. $a$ is a coefficient associated with the feed position of the tapped line as indicated in Figure 5-2(a). $K$ and $J$ present impedance inverter and admittance inverter, respectively. The use of $K$ and $J$ inverters is because the external coupling from port 1 can be considered as inductive coupling and the external coupling from port 2 can be considered as capacitive coupling. $R_A$ and $R_B$ are terminal impedances. As can be seen that impedance inverter $K(a)$ and shunt series resonator ( $L(a)$ and $C(a)$ ) are a function of coefficient $a$. Hence, the feed position of the tapped line can affect both extracted attenuation pole and external coupling to odd and even modes.

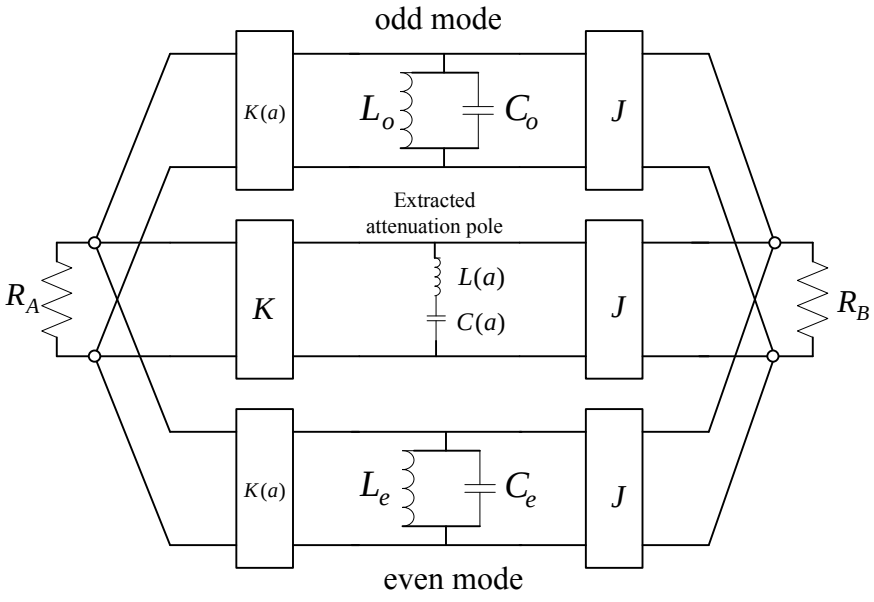


Figure 5-6. Circuit model of the proposed doublet filter.

### *5.2.2 Fabrication and experimental results*

For the experimental demonstration, the above filter is fabricated on a substrate with a relative dielectric constant of 10.8 and a thickness of 1.27 mm. Figure 5-7(a) is a photograph of the fabricated filter with an overall circuit size of 15 mm×15.1 mm. The measured and simulated results are given in Figure 5-7(b) for the comparison. The measured response agrees well with that of the EM simulation.

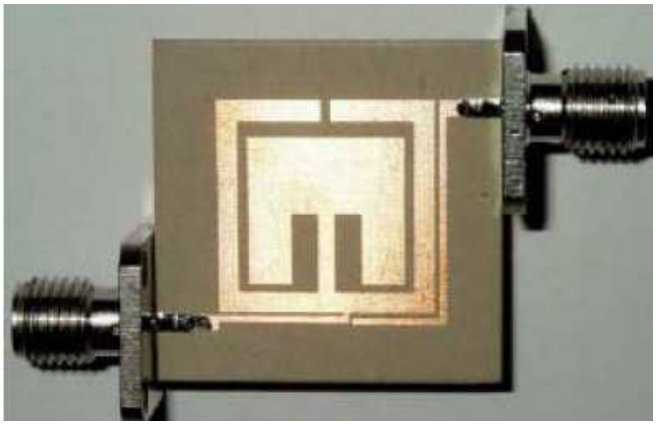

(a)

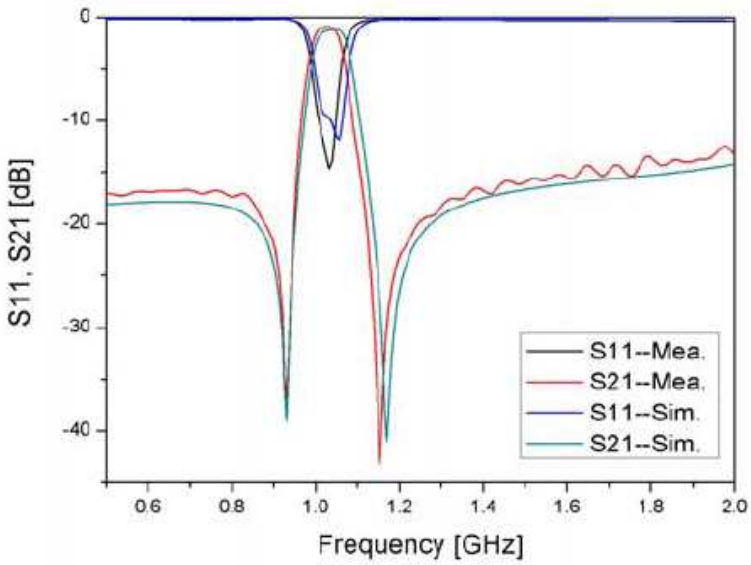


(b)

Figure 5-7. (a) Fabricated doublet dual-mode filter. (b) Measured and simulated response.

### *5.2.3 More examples*

According to the above study of the mechanism of producing transmission zeros in the doublet filter comprised of a single microstrip dual-mode open-loop resonator, it is also possible to control both TZs frequencies and allocate the both at the upper stopband. Figure 5-8 shows an example of this type of doublet and its simulated response. Note that the position of the tapped line feed structure has been changed.

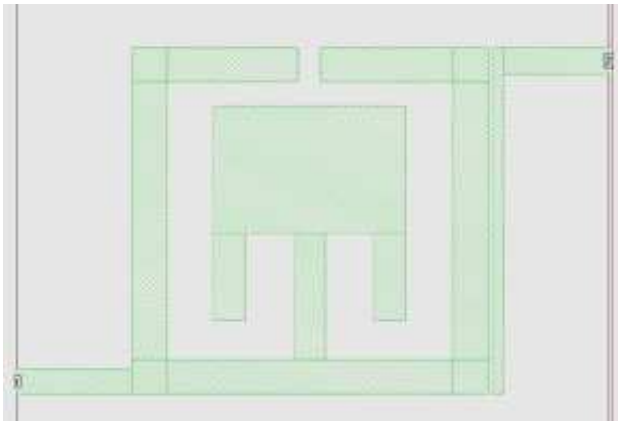

(a)

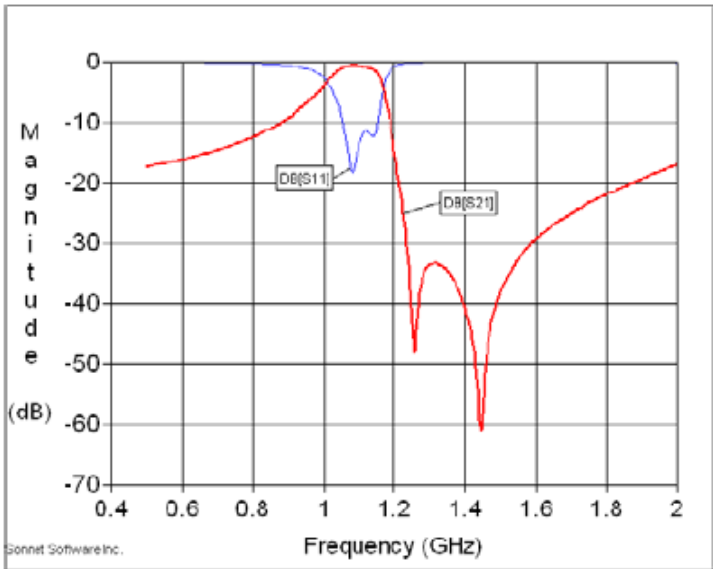


(b)

Figure 5-8. (a) A doublet dual-mode filter that exhibits two TZs at the upper stopband. (b) Simulated response.

Multi-pole quasi-elliptic function filters can be built up by cascading several doublets. Shown in Figure 5-9(a) is a 4-pole filter of this type, which consists of two doublets. The performance of the filter is displayed in Figure 5-9(b). As can be seen,

three finite-frequency TZs are generated without implementing any cross couplings. As a matter of fact, the doublet on the left produces the TZ at 1.16 GHz, and the doublet on the right produces the TZs at 0.935 and 1.4 GHz. The overall circuit size of the filter is 34.5 mm×15.1 mm.

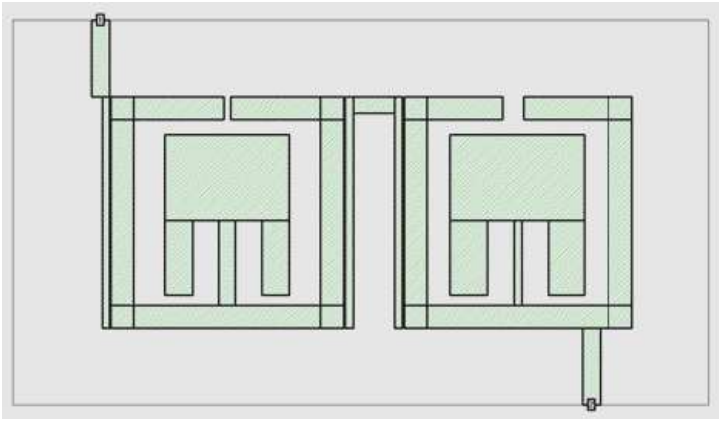

(a)

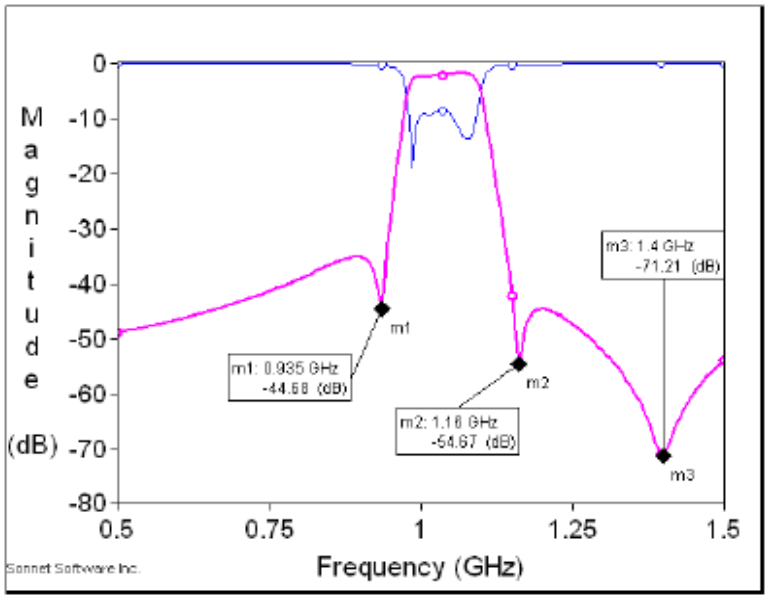


(b)

Figure 5-9. (a) 4-pole quasi-elliptic function filter comprised of two doublets to exhibit three finite-frequency TZs. (b) Simulated performance.

## 5.3 Parallel Feed Microstrip Quasi-Elliptic Function Bandpass Filter

A new type of four-pole microstrip quasi-elliptic function bandpass filter based on dual-mode open-loop resonator has been investigated recently [10]. The four-pole filter is formed by cascading two dual-mode resonators in a series configuration using non-resonating nodes, as shown in Figure 5-10(a).

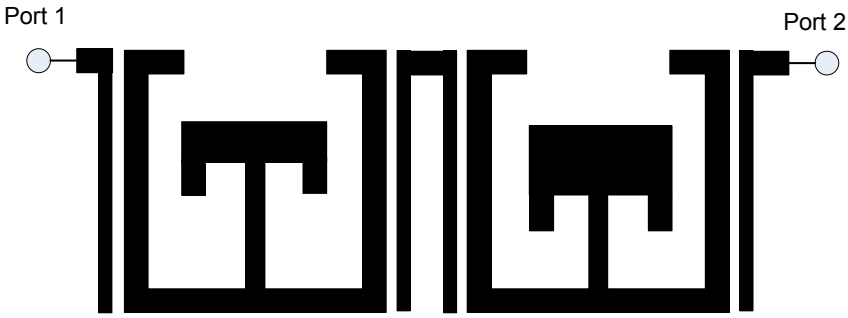


(a)

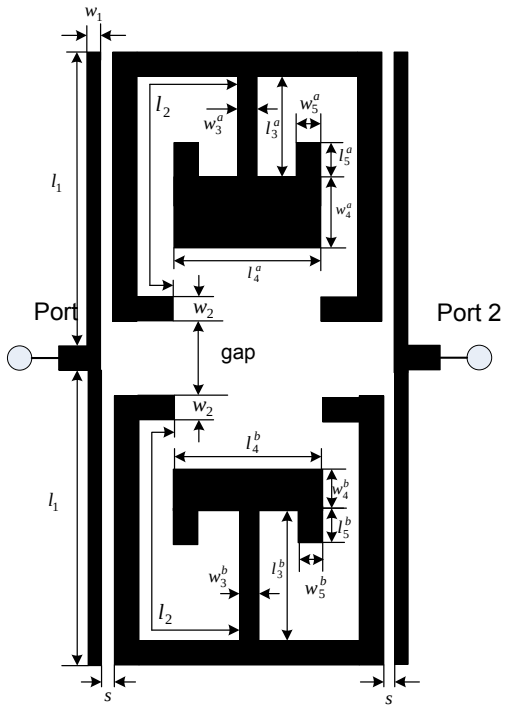


(b)

Figure 5-10. (a) A layout of reported work cascaded in series configuration [10]. (b) A layout of proposed filter built in parallel feed configuration.

In order to improve in-band perforamce, such as less less insertion loss and better matching at mid-band of passband, parallel feed configuration of the microstrip dual-mode quasi-elliptic function bandpass filter is proposed in Figure 5-10(b). As comparing with the previous topology in Figure 5-10(a). the odd modes of the proposed parallel feed filter are coincided, resulting in a 3-pole quasi-elliptic function response rather than a 4-pole quasi-elliptic function response by cascading in series configuration. Hence, less insertion loss can be achieved with a better mid-band performance. Moreover, by relocating the modal frequencies, a dual-band operation of the proposed parallel feed filter can be obtained. Design coupling scheme and design procedure are discussed below.

### *5.3.1 Filter operation and design*

Figure 5-10(b) is a layout of the proposed filter with two dual-mode open-loop resonators that are built in parallel feed configuration with respect to the input and output ports. The gap between the two dual-mode open-loop resonators is chosen such that the coupling between them is negligible. The proposed dual-mode filter has a coupling scheme as shown in Figure 5-11, where S and L denote the input and output ports respectively; node 1, 3 denote the odd-mode and node 2, 4 denote the even-mode.

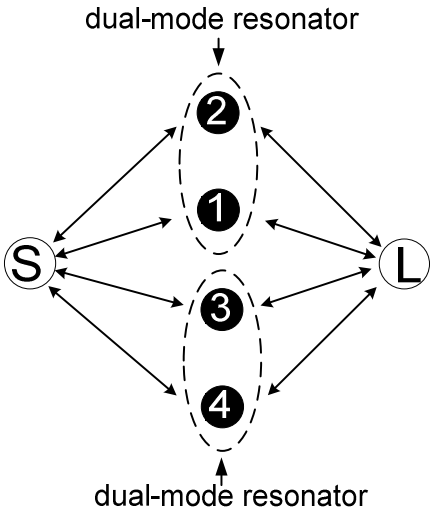


Figure 5-11. The coupling scheme of the parallel feed three-pole filter.

It should be mentioned that the pair of operating modes in each dual-mode open-loop resonator do not couple to each other [10]. Also, notice that, in order to achieve a good matching at the mid-band of passband, the odd modes of the two dual-mode resonators, namely, node 1 and node 3, are needed to be identical. The two transmission zeros located at each side of passband are associated with the two even modes having different loading elements inside the open-loop as illustrated in Figure 5-10(b). This implies that the location of the two transmission zeros can be controlled by adjusting the loading elements of the two even modes, respectively.

To design the proposed three-pole parallel feed dual-mode filter, a coupling matrix method may be applied (see Section 4.2.1.1). According to the coupling scheme and the filter operation, the coupling matrix may be defined as

$$M = \begin{bmatrix} 0 & ms1 & ms2 & ms3 & ms4 & 0 \\ ms1 & m11 & 0 & 0 & 0 & mL1 \\ ms2 & 0 & m22 & 0 & 0 & mL2 \\ ms3 & 0 & 0 & m33 & 0 & mL3 \\ ms4 & 0 & 0 & 0 & m44 & mL4 \\ 0 & mL1 & mL2 & mL3 & mL4 & 0 \end{bmatrix} \qquad (5.2)$$

where $msi$ (i=1 to 4) presents the coupling between the source and resonators, $mLi$ denotes the coupling between the load and resonators, $mii$ denotes resonator tuning. As the odd modes are identical, this results $m11 = m33$ ; $ms1 = ms3$ ; $mL1 = -ms1$ ; $mL3 = -ms3$. In order to achieve symmetrical response, the relations should be held as $ms2 = ms4$ and $m22 = -m44$. Moreover, for the symmetrical plane locates at the odd mode resonant frequency, this requires $m11 = m33 = 0$. To calculate the transmission coefficient S21 and reflection coefficient S11 of the proposed coupling matrix, the following expressions may be employed (see Section 4.2.1.1).

$$S_{21} = -2j[A]^{-1}_{n+2,1} \qquad (5.3)$$

$$S_{11} = 1 + 2j[A]^{-1}_{1,1} \qquad (5.4)$$

where n denotes the number of resonators, $[A]$ is an associated matrix including the coupling matrix $[M]$ as referring to Section 4.2.1.1.

**Design example:**

The proposed parallel feed configuration filter has been designed using microstrip lines with the following specifications:

| | |
|---|---|
| Center frequency: | 1.087 GHz |
| Fractional bandwidth (FBW) | 10% |
| Number of poles: | 3 |
| Finite-frequency transmission zeros: | 1.0 GHz and 1.17 GHz |

For the synthesis of the coupling matrix coefficients according to the prescribed frequency response, a gradient-based optimization technique can be employed [1], which results in $ms1 = 0.52$ ; $ms2 = 0.37$ ; $m11 = m33 = 0$ ; $m22 = -1.1$ ; $m44 = 1.1$ . By using (4.8)-(4.11), the design parameters can be determined as $f_0^o = 1.087$ GHz; $f_0^{e1} = 1.147$ GHz; $f_0^{e2} = 1.027$ GHz; $Q_{exo} = 37.0$ and $Q_{exe} = 73.0$ . Where $f_0^{e1}$ , $f_0^{e2}$ denote the even-mode resonant frequencies at high side and low side of the passband, respectively. In order to extract the physical dimensions by employing the even-and odd-mode analysis method given in Section 4.2.1.3, the proposed parallel feed configuration filter may be decomposed into two two-pole filters as given in Figure 5-12.

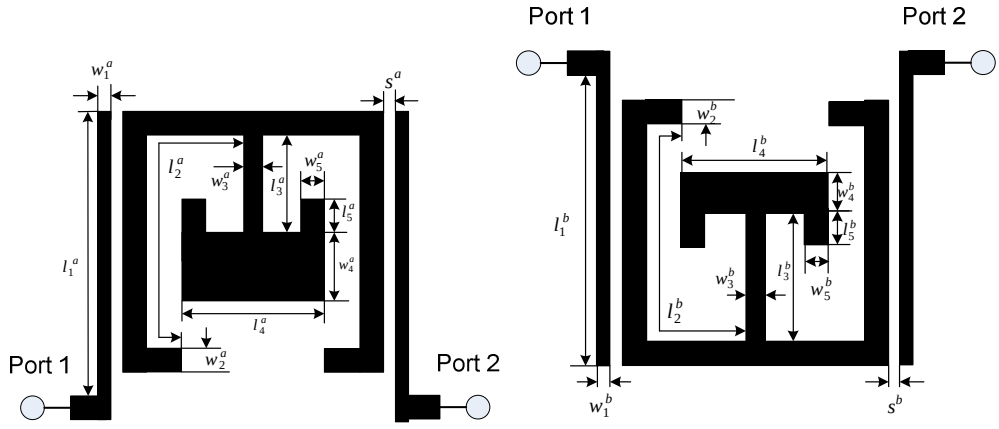


Figure 5-12. Layout of (a) upper two-pole dual-mode filter and (b) lower two-pole dual-mode filter.

After the upper two-pole dual-mode filter and the lower two-pole filter are designed, they are built in parallel feed configuration to form the proposed three-pole filter as

displayed in Figure 5-10(b). Notice that the external coupling of the two-pole dual-mode filters is twice stronger than the three-pole parallel feed configuration filter. This is because the transmitted power is divided by half for the filter in parallel feed configuration. Hence, the design parameters for the upper two-pole dual-mode filter are modified as $f_0^o = 1.087$ GHz; $f_0^{e1} = 1.147$ GHz; $Q_{exo} = 37.0/2 = 18.5$ and $Q_{exe} = 73.0/2 = 36.5$ , and for the lower two-pole dual-mode filter are $f_0^o = 1.087$ GHz; $f_0^{e2} = 1.027$ GHz; $Q_{exo} = 37.0/2 = 18.5$ and $Q_{exe} = 73.0/2 = 36.5$ . The design parameters extracted from full-wave EM simulation [79] comparing with the calculated ones are listed in Table 5-1.

**TABLE 5-1**

**Comparison of calculated and extracted design parameters**

| Design parameters | Calculated | Extracted | Design parameters | Calculated | Extracted |
|---|---|---|---|---|---|
| $f_0^o$ | 1.087 | 1.032 | $f_0^o$ | 1.087 | 1.032 |
| $f_0^e$ | 1.027 | 1.04 | $f_0^e$ | 1.147 | 1.149 |
| $Q_{exo}$ | 18.5 | 19.0 | $Q_{exo}$ | 18.5 | 19.0 |
| $Q_{exe}$ | 36.5 | 43.9 | $Q_{exe}$ | 36.5 | 37.3 |
| The upper two-pole dual-mode filter | | | The lower two-pole dual-mode filter | | |

**TABLE 5-2**

**Parameters of the proposed parallel feed three-pole filter (in millimeters) (see Figure 5-10(b))**

| $w_1$ | $w_2$ | $w_3^a$ | $w_4^a$ | $w_5^a$ | $w_3^b$ | $w_4^b$ | $w_5^b$ | $s$ |
|---|---|---|---|---|---|---|---|---|
| 0.3 | 1.5 | 1.1 | 5.5 | 1.8 | 0.9 | 5.5 | 2.7 | 0.15 |
| $l_1$ | $l_2$ | $l_3^a$ | $l_4^a$ | $l_5^a$ | $l_3^b$ | $l_4^b$ | $l_5^b$ | gap |
| 16.2 | 23.2 | 5.5 | 8.1 | 3.5 | 5.5 | 9.9 | 3.9 | 3.5 |

Note that the extracted odd-mode resonant frequency is slightly lower than the calculated one is due to the unwanted coupling between the odd modes in physical realization, which will be discussed in Section 5.3.4. The final layout of the proposed parallel feed three-pole filter is given in Table 5-2.

The frequency responses of the proposed three-pole filter are presented in Figure 5-13, where both results, i.e. calculated by using the coupling matrix and simulated by using the full-wave EM simulator [79], are plotted together for the comparison, which show a good agreement. The simulated out of band rejection level on the lowside of passband is smaller than the one on the highside of passband, which is due to the coupling to the even mode associated with the lowside transmission zero is weaker than the one associated with the highside transmission zero by using the proposed topology in Figure 5-10(b) as indicated in Table 5-1.

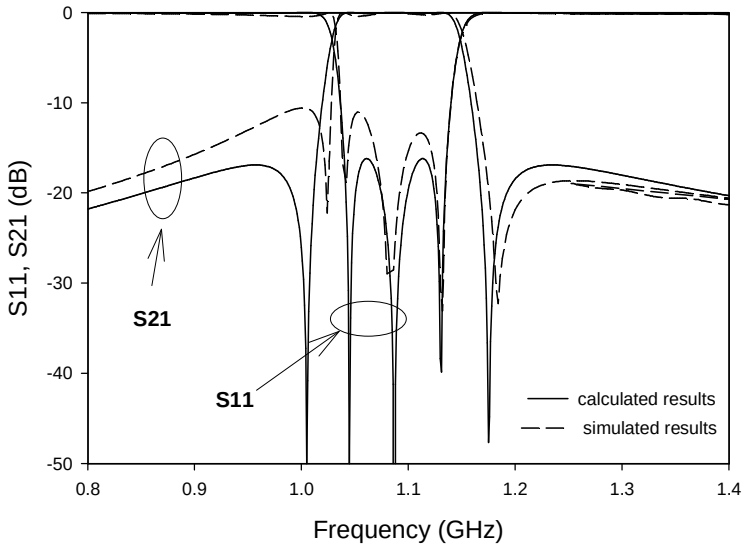


Figure 5-13. Calculated and EM-simulated performance of the proposed parallel feed three-pole filter.

### *5.3.2 Comparison study*

In order to make a comparison with previous work (see Figure 5-10(a)), a previous work with similar bandwidth and centre frequency using the same substrate

has been designed and its frequency responses comparing with the proposed filter are displayed in Figure 5-14.

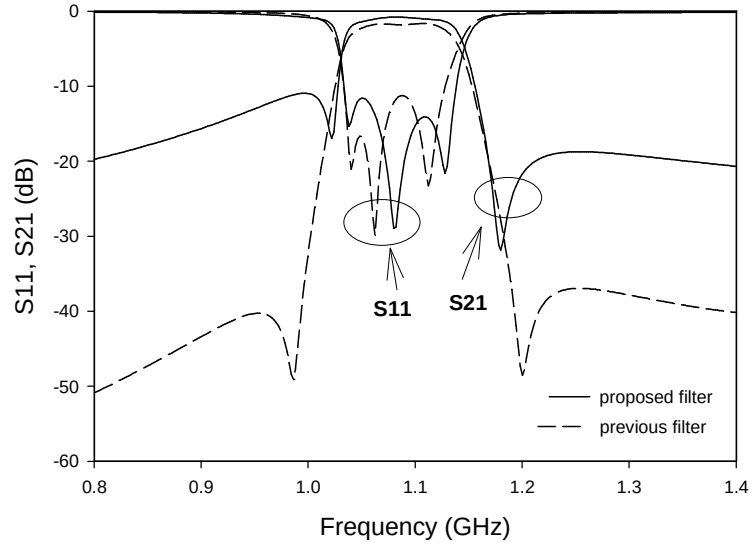


(a)

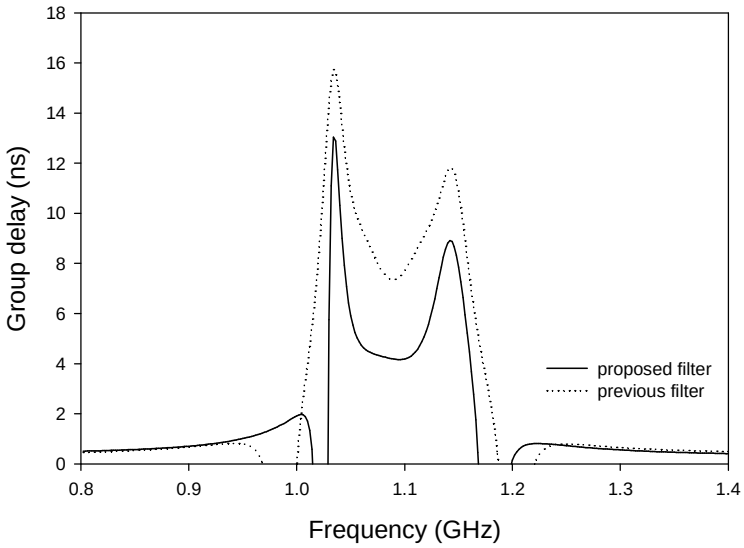


(b)

Figure 5-14. The comparison of simulated proposed filter and previous work: (a) S-parameter performance. (b) Group delay.

It is envisaged that the proposed filter has smaller insertion loss at the passband and nearly half group delay less than the previous work due to 3-pole instead of 4-pole filter topology of the proposed parallel feed configuration filter. At the mid-band of passband,

the return loss of the proposed filter is about 30 dB, while the previous work obtains only about 12 dB, which shows a better matching condition of the proposed filter. However, the out of band rejection level is lower than the previous work, which is a typical characteristic similar to that reported in [87]. Therefore, there is a trade off between the two designs.

### *5.3.3 Fabrication and measurements*

To demonstrate this type of filter experimentally, the filter is fabricated on a substrate with a relative dielectric constant of 10.2 and a thickness of 1.27 mm as shown in Figure 5-15(a) with an overall circuit size of 16 mm×33.5 mm. The measured results are plotted in Figure 5-15(b), which is obtained using Agilent 8510B network analyzer. From Figure 5-15(b) we can observe that the experimental four-pole bandpass filter exhibits good performance over the passband, which is similar to the simulated one. The measured centre frequency is 1.04 GHz with a fractional bandwidth of 10% (3 dB bandwidth). The insertion loss at the mid-band is better than 0.7dB. Notice that the measured centre frequency is slightly lower than the simulated one (1.08 GHz). This may be due to the slightly larger dielectric constant of the substrate used in the fabrication.

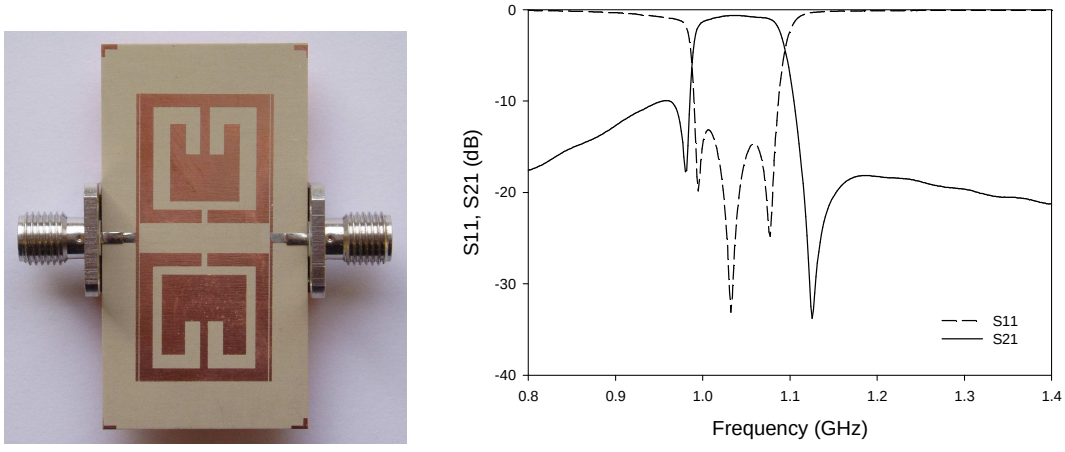


(a) (b)

Figure 5-15. (a) Photograph of the fabricated proposed parallel feed three-pole filter. (b) Measured results.

### *5.3.4 Discussion*

It is notice that there are small coupling exist between node 1 and node 3, and, node 2 and node 4 due to the close placement of the two dual-mode resonators. It is interesting that these coupling seem to shift both odd modes and even modes in the same direction, but not splitting them in a conventional way. These can be observed in Figure 5-16. It can be seen that as the gap between the two dual-mode resonators (see Figure 5-10(b)) is changed, both odd modes and even modes are shifted accordingly in the same direction. It is also shown that the even modes are hardly affected by the coupling, which implies that the gap may be employed to improve the passband performance by relocating the odd mode resonant frequencies while the even mode resonant frequencies are kept nearly the same. For large gaps, the coupling between the odd modes or even modes can be neglected as the modal frequencies are nearly the same for the gap of 3.5 mm and 5.9 mm, observed from Figure 5-16.

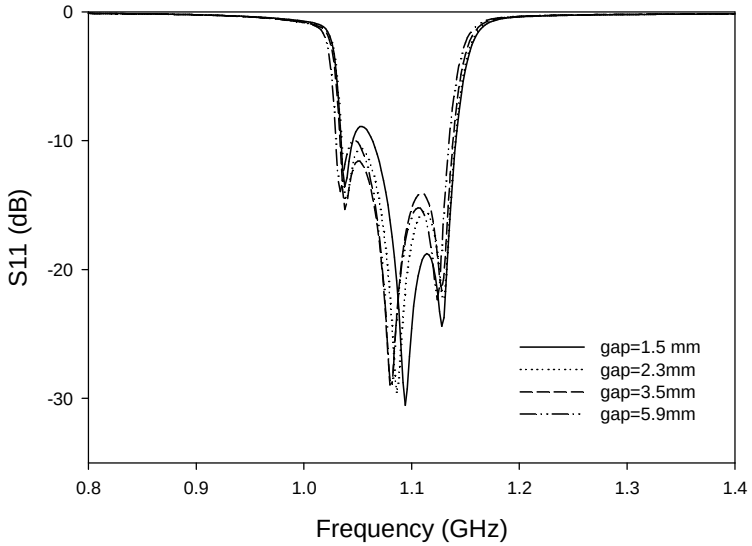


Figure 5-16. The coupling effects between the two odd modes or the even modes.

### *5.3.5 Parallel feed configuration dual-band filters*

The proposed parallel feed configuration filter can be designed as a dual-band filter when the two dual-mode resonators i.e. node 1 and 2, and node 3 and 4 are located

at dual-band frequencies. In order to derive the dual-band frequency responses using coupling matrix method, the frequency variable matrix in (4.7) is modified as indicated in (5.5) and (5.6)

$$\begin{bmatrix} 0 & 0 & 0 & 0 & 0 & 0 \\ 0 & \Omega(f) & 0 & 0 & 0 & 0 \\ 0 & 0 & \Omega(f) & 0 & 0 & 0 \\ 0 & 0 & 0 & \Omega(f) & 0 & 0 \\ 0 & 0 & 0 & 0 & \Omega(f) & 0 \\ 0 & 0 & 0 & 0 & 0 & 0 \end{bmatrix} \quad (5.5) \quad \Rightarrow \quad \begin{bmatrix} 0 & 0 & 0 & 0 & 0 & 0 \\ 0 & \Omega 1(f) & 0 & 0 & 0 & 0 \\ 0 & 0 & \Omega 1(f) & 0 & 0 & 0 \\ 0 & 0 & 0 & \Omega 2(f) & 0 & 0 \\ 0 & 0 & 0 & 0 & \Omega 2(f) & 0 \\ 0 & 0 & 0 & 0 & 0 & 0 \end{bmatrix} \quad (5.6)$$

with

$$\Omega 1(f) = \frac{1}{FBW1}\left(\frac{f}{f_{01}} - \frac{f_{01}}{f}\right) \qquad (5.7)$$

$$\Omega 2(f) = \frac{1}{FBW2}\left(\frac{f}{f_{02}} - \frac{f_{02}}{f}\right) \qquad (5.8)$$

where $\Omega(f)$ is the frequency variable of the lowpass prototype. $f_{01}$, $f_{02}$ denote center frequency of the dual passbands and $FBW1$, $FBW2$ denote the fractional bandwidth of the dual passbands, respectively. The coupling matrix $[M]$ is the same as (5.2). By using (5.3) and (5.4), parallel feed configuration dual-band filters with different filtering characteristics are computed and demonstrated in the following.

Figure 5-17(a) presents a dual-band filter (filter A) with high selectivity on the lowside of the high passband and high selectivity on the highside of the low passband with the design parameters are $f_{01}$ =1.08 GHz; $f_{02}$ =1.6GHz; $FBW1$ = $FBW2$ =0.1; $ms1 = ms3 = 0.6$; $ms2 = ms4 = 0.37$; $m11 = 0.5$; $m22 = -0.5$; $m33 = -0.5$; $m44 = 0.5$. By only exchanging the odd-and even-mode resonant frequencies of the dual-mode resonators, the filtering characteristics of filter A has an opposite frequency responses as displayed in Figure 5-17(b) (filter B), where $m11 = -0.5$; $m22 = 0.5$; $m33 = 0.5$; $m44 = -0.5$.

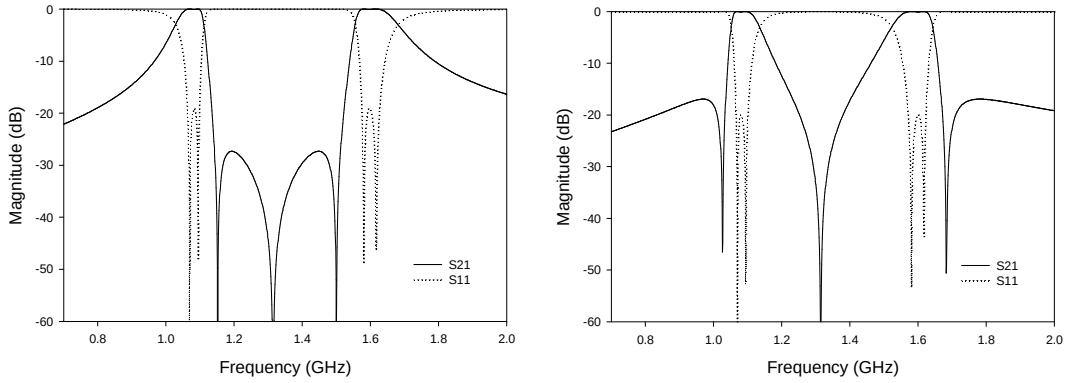


(a) (b)

Figure 5-17. Calculated frequency responses of (a) filter A and (b) filter B.

The bandwidth of the dual bands can be controlled independently as the four modes of the dual-mode resonators do not couple to each other. They are illustrated in Figure 5-18, where the design parameters of filter C are the same as filter A except $FBW1$=0.05; $FBW2$ =0.1, and the design parameters of filter D are the same as filter A except $FBW1$=0.1; $FBW2$ =0.05.

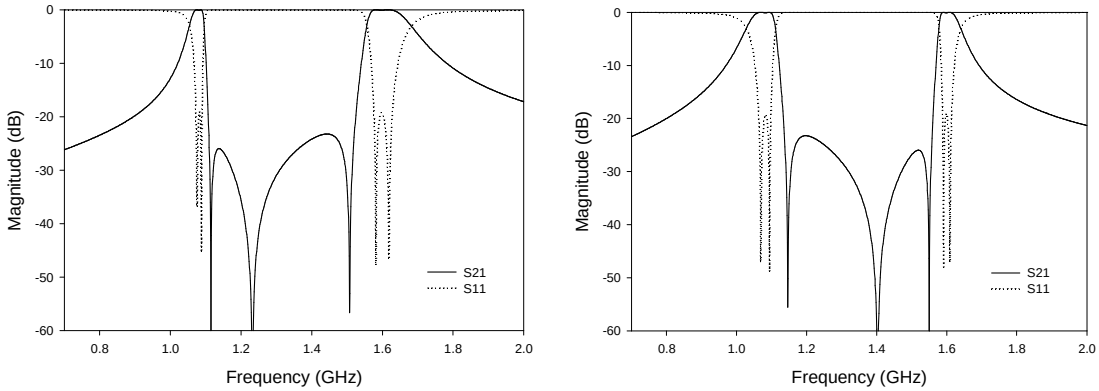


(a) (b)

Figure 5-18. Calculated frequency responses of (a) filter C and (b) filter D.

To realize the parallel feed configuration dual-band filter using microstrip lines, the design method given in Section 5.3.1 can be employed. Take filter D as an example, the proposed parallel feed configuration dual-band filter may be decomposed into two two-pole filters, i.e. the low passband filter and the high passband filter. The EM simulated layouts of the two filters are depicted in Figure 5-19.

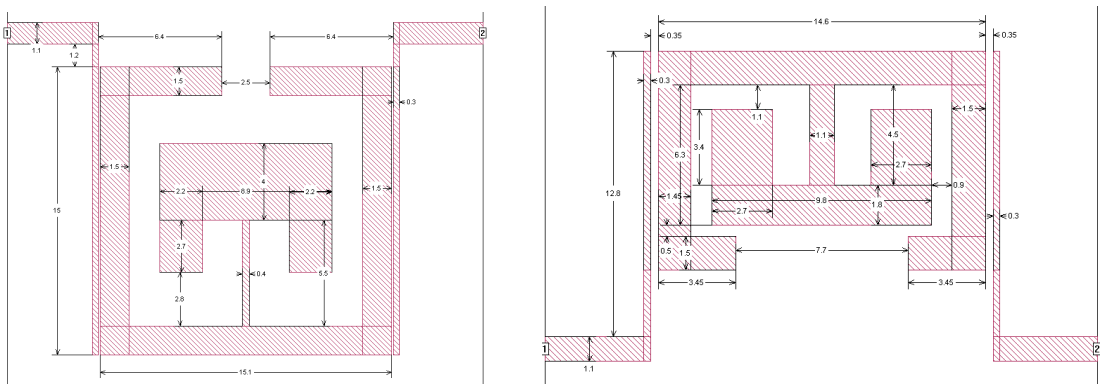

(a) (b)

Figure 5-19. (a) EM simulated layout of the low passband filter. (b) EM simulated layout of the high passband filter.

The ideal design parameters can be calculated using (4.8)-(4.11) as $f_0^o = 1.053$ GHz; $f_0^e = 1.107$ GHz; $Q_{exo} = 27.8/2 = 13.9$ and $Q_{exe} = 73.0/2 = 36.5$ for the low passband filter, and for the high passband filter are $f_0^o = 1.62$ GHz; $f_0^e = 1.58$ GHz; $Q_{exo} = 55.6/2 = 27.8$ and $Q_{exe} = 146.0/2 = 73.0$. By using the design method given in Section 4.2.1.3, the design parameters extracted from full-wave EM simulation comparing with the calculated ones are listed in Table 5-3. The final layout of the dual-band filter is given in Table 5-4.

**TABLE 5-3**

**Comparison of calculated and extracted design parameters of filter D**

| Design parameters | Calculated | Extracted | Design parameters | Calculated | Extracted |
|---|---|---|---|---|---|
| $f_0^o$ | 1.053 | 1.052 | $f_0^o$ | 1.62 | 1.624 |
| $f_0^e$ | 1.107 | 1.106 | $f_0^e$ | 1.58 | 1.586 |
| $Q_{exo}$ | 13.9 | 14.62 | $Q_{exo}$ | 27.8 | 27.87 |
| $Q_{exe}$ | 36.5 | 35.85 | $Q_{exe}$ | 73 | 74.4 |
| The low passband filter | | | The high passband filter | | |

**TABLE 5-4**

**Parameters of the proposed parallel feed configuration dual-band filter (filter D) (in millimeters) (see Figure 5-19)**

| $w_1^a$ | $w_2^a$ | $w_3^a$ | $w_4^a$ | $w_5^a$ | $w_1^b$ | $w_2^b$ | $w_3^b$ | $w_4^b$ | $w_5^b$ | $s^a$ | gap |
|---|---|---|---|---|---|---|---|---|---|---|---|
| 0.3 | 1.5 | 1.3 | 1.8 | 2.7 | 0.3 | 1.5 | 0.4 | 4 | 2.2 | 0.35 | 6.1 |
| $l_1^a$ | $l_2^a$ | $l_3^a$ | $l_4^a$ | $l_5^a$ | $l_1^b$ | $l_2^b$ | $l_3^b$ | $l_4^b$ | $l_5^b$ | $s^b$ | |
| 13.6 | 17.1 | 4.5 | 9.8 | 3.9 | 16.2 | 24.2 | 5.5 | 8.9 | 2.7 | 0.1 | |

Figure 5-20 shows the full-wave EM simulated frequency responses of the proposed parallel feed configuration dual-band filter (filter D), comparing with the one calculated by using the coupling matrix. It can be seen that the center frequency of the high passband filter is lower the calculated one and its bandwidth is smaller than the calculated one. The differences may due to the asymmetrical topology of the filter (The size of the high passband filter is smaller than the low passband filter as shown in Figure 5-19). Thus, the design method may be suitable for an initial design.

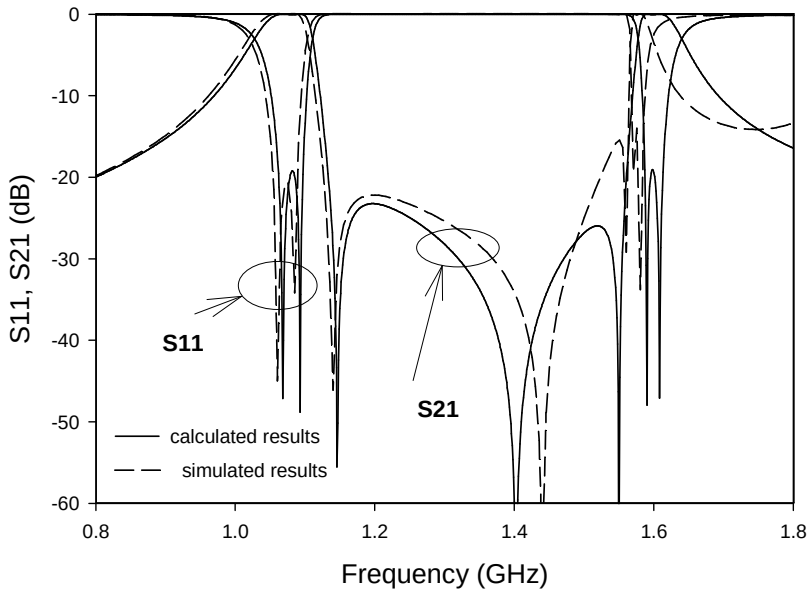


Figure 5-20. Calculated and EM-simulated performance of the proposed parallel feed configuration dual-band filter (filter D).

**Discussion**

Comparing to the dual-band filter described in Section 5.4, the dual-band filter with parallel feed configuration has more flexible filtering characteristics regarding to the control of finite-frequency transmission zero that associated with even-mode and the bandwidth of the dual passbands. However, the parallel feed configuration dual-band filter is difficult to form a higher order filter.

## 5.4 Dual-Band Filter based on Non-Degenerate Dual-Mode Slow-Wave Open-Loop Resonators

This section presents a new class of compact dual-band filters based on the dual-mode microstrip slow-wave open-loop resonator of Figure 5-21(a), which is evolved from the previous work [1], [10]. The slow-wave effect of this type of resonator has been investigated in Section 3.5. This resonator can support two non-degenerate modes, which do not couple regardless of the separation of the two modes. Therefore, it can be treated as doublet with a coupling structure of Figure 5-21(b). The non-degenerate dual-mode microstrip slow-wave open-loop resonator can be used as a building block for designing high order miniature dual-band filters. By employing different feed schemes and coupling structures, this type of dual-band filter exhibits different filtering characteristics, which are demonstrated in the following.

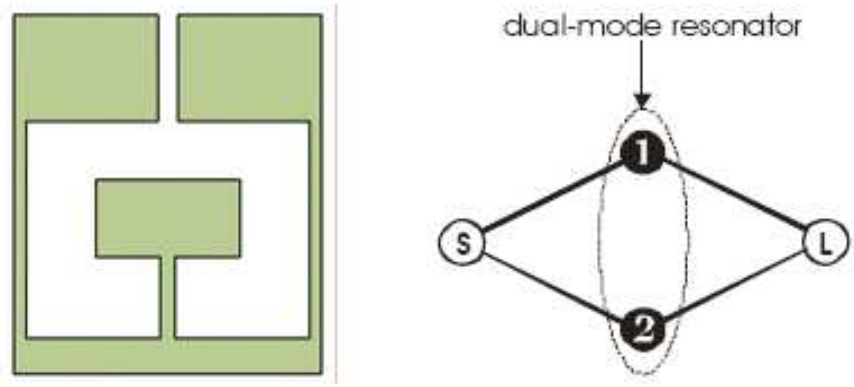


(a) (b)

Figure 5-21. (a) Non-degenerate dual-mode microstrip slow-wave open-loop resonator. (b) Its coupling structure as a doublet.

### *5.4.1 Filter operation and design examples*

#### *5.4.1.1 Filter with coupled-line input/output structure*

Figure 5-22(a) shows a dual-band filter comprised of two non-degenerate dual-mode resonators. The input and output (I/O) of the filter use a coupled line structure. Figure 5-22(b) displays the full-wave electromagnetic (EM) simulated frequency response of the proposed dual-band filter on a dielectric substrate with a relative dielectric constant of 10.8 and a thickness of 1.27 mm. The EM simulation is performed using a commercially available tool, i.e. Sonnet EM [79].

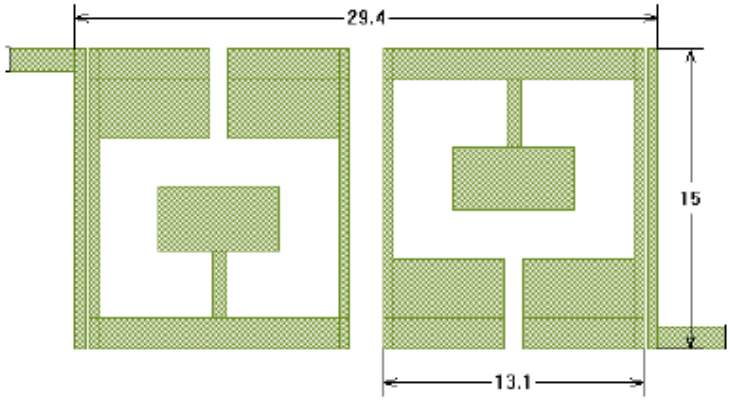


(a)

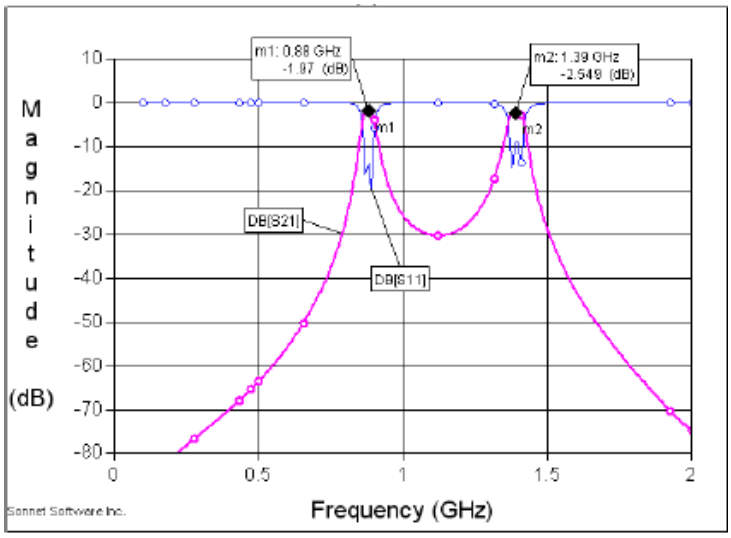


(b)

Figure 5-22. (a) Dual-band filter with coupled-line I/O. (b) EM simulated response.

Figure 5-23 shows the fabricated filter and measured response. The two passbands are centered at 0.86 GHz and 1.39 GHz, respectively. The maximum rejection between the two bands is 30 dB. The overall circuit size of the filter is 29.4 mm×15 mm.

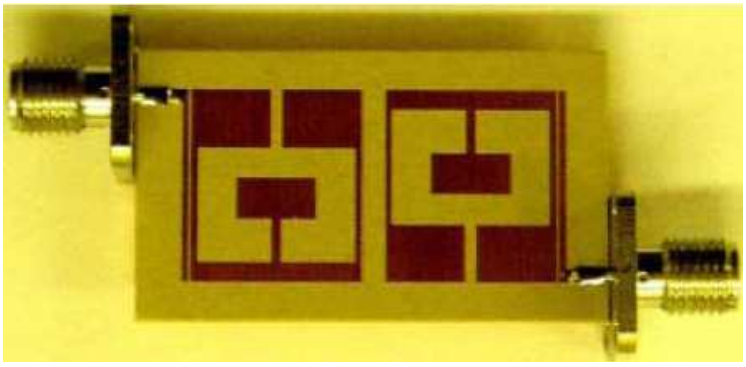

(a)

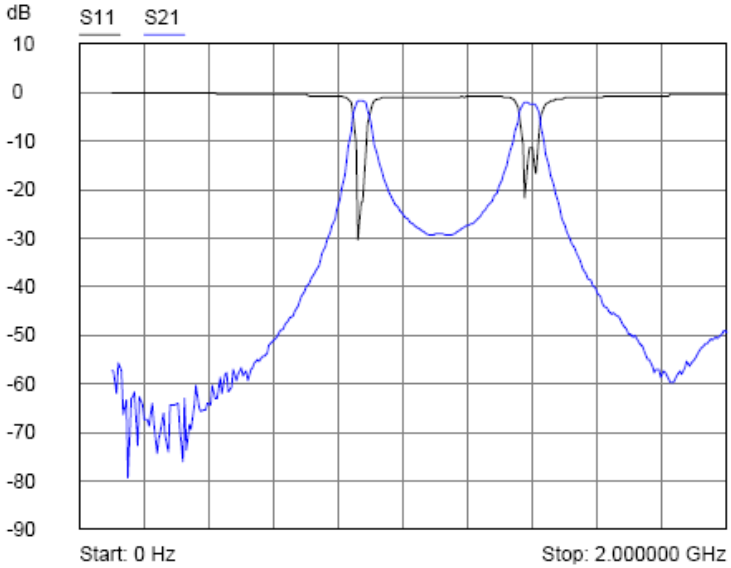


(b)

Figure 5-23. (a) Fabricated dual-band filter with coupled-line structure. (b) Its measured performance.

### *5.4.1.2 Filter with tapped-line input/output structure*

Figure 5-24(a) shows another dual-band filter which is fed by the tapped line at the input and output. The simulated response is shown in Figure 5-24(b).

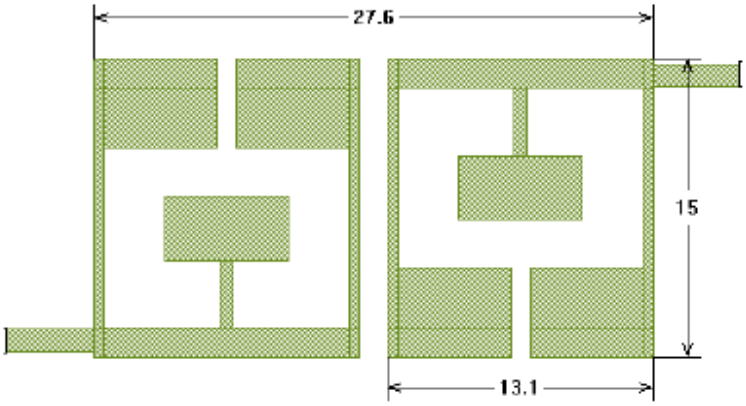


(a)

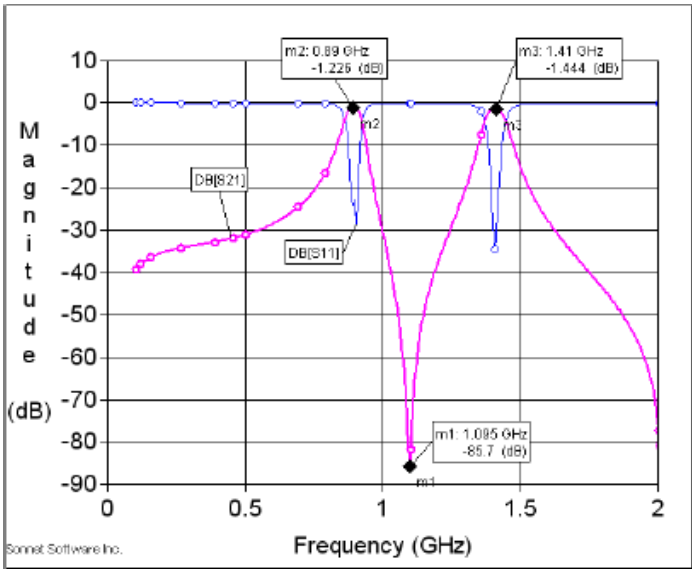


(b)

Figure 5-24. (a) Dual-band filter with tapped-line I/O. (b) EM simulated response.

It is notable that there is a transmission zero (TZ) allocated at a frequency between the two passbands. The EM simulation is carried out to obtain the EM field distribution at this frequency, i.e. 1.095 GHz in this case, and the results are illustrated in Figure 5-25. It is clear to see that one arm of the first dual-mode resonator is resonant at this frequency, which presents a short circuit at the input resulting in the transmission zero observed in Figure 5-24(b). For the experimental demonstration, the filter is fabricated on the same substrate mentioned in the last section. Figure 5-26(a) is a photograph of the fabricated filter and Figure 5-26(b) is the measured response. The overall circuit size of the filter is 27.6 mm×15 mm.

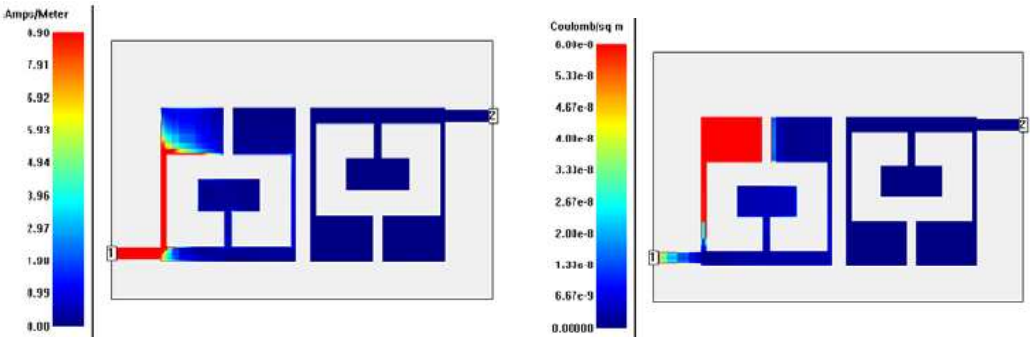


(a) (b)

Figure 5-25. Field distribution at the frequency of the transmission zero (1.095 GHz). (a) Current. (b) Charge.

(a)

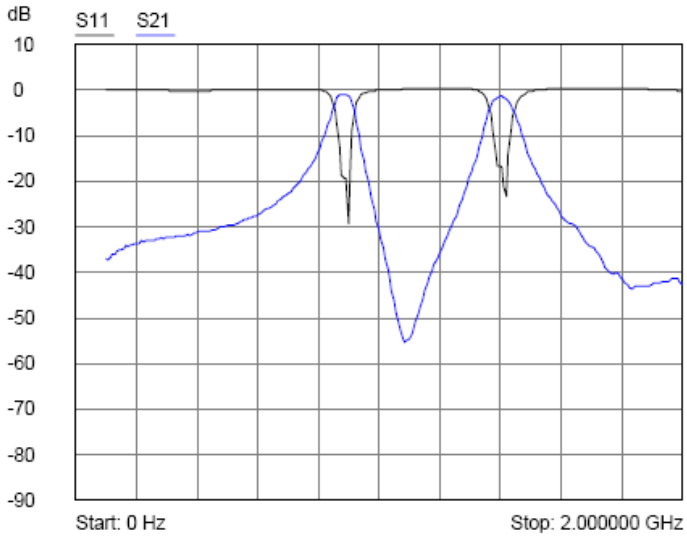


(b)

Figure 5-26. (a) Fabricated dual-band filter with tapped-line structure. (b) Its measured performance.

### *5.4.2 Higher order dual-band filters*

Higher order filters of this type can be easily built up in a cascade structure. Two examples of three-pole dual-band filter of this type are shown in Figure 5-27 and Figure 5-28 with the circuit sizes indicated. The filters are designed on a 1.27-mm thick dielectric substrate with a dielectric constant of 10.8. The filter responses shown are obtained by using the EM simulation. It is interesting to note that there is a transmission zero at around 1.8 GHz for both filters. This is believed to be caused by the resonance of the loading element inside the slow-wave open loop.

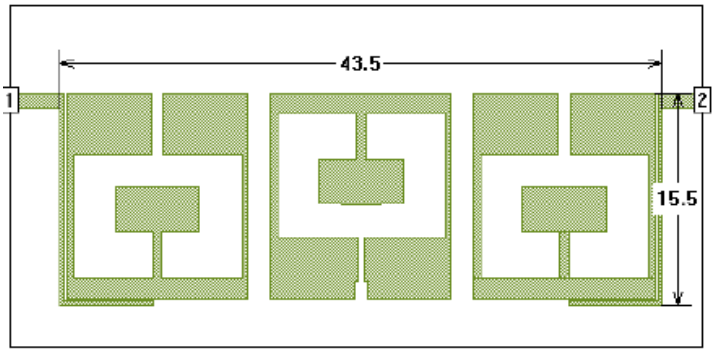


(a)

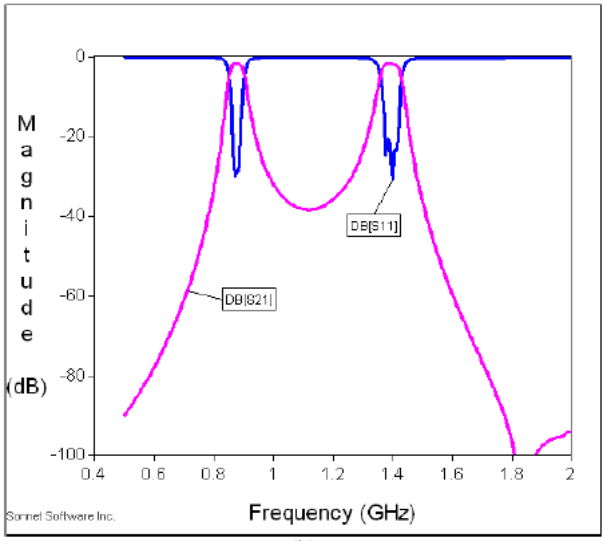


(b)

Figure 5-27. (a) Three-pole dual-band filter A. (b) Simulated response.

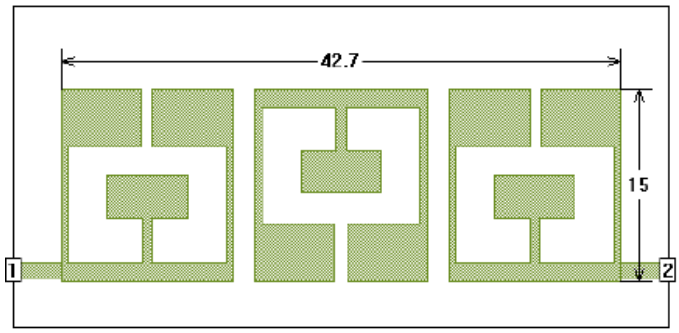


(a)

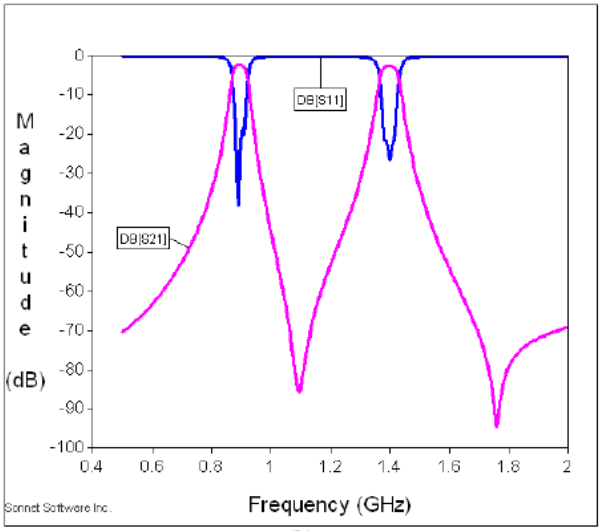


(b)

Figure 5-28. (a) Three-pole dual-band filter B. (b) Simulated response.

Except for the I/O feed structure, the above two filters have a similar topology, in which the adjacent dual-mode resonators have an opposite orientation. In fact, this is not necessary and the proposed non-degenerate dual-mode resonator is very flexible for forming different filter topologies. For the demonstration, Figure 5-29(a) illustrates the layout of another three-pole dual-mode filter, where all resonators have the same orientation. The simulated response is given in Figure 5-29(b). An extra transmission zero is found on the low side of the first passband. The overall circuit size of the filter is 43.3 mm×15.5 mm.

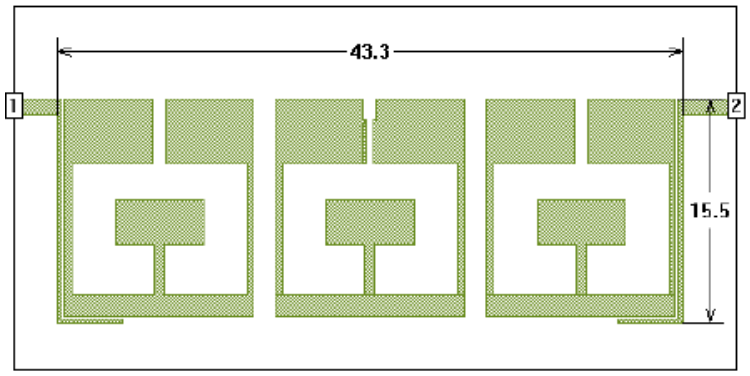


(a)

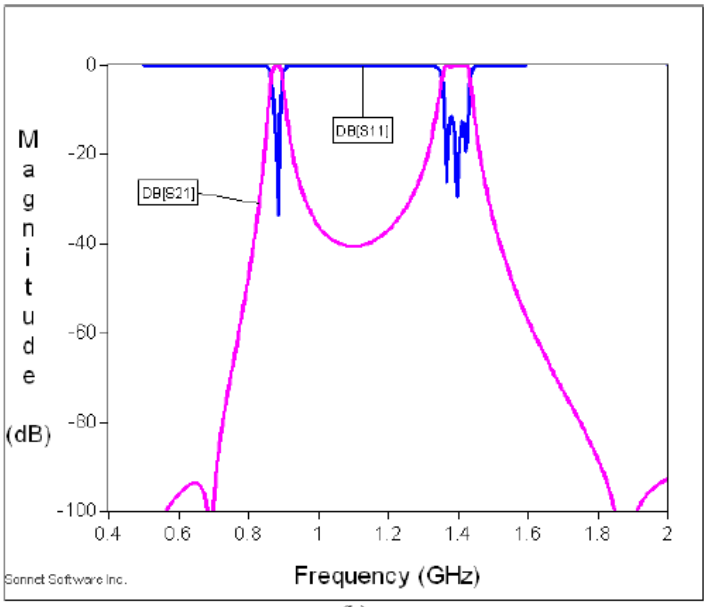


(b)

Figure 5-29. (a) Three-pole dual-band filter C. (b) Simulated response.

## 5.5 Summary

Three new types of dual-mode filters based on a miniature dual-mode resonator with novel configurations have been investigated.

Miniature doublet filters that exhibit quasi-elliptic function response without any cross coupling has been introduced in Section 5.2. It has been found that the TZs are produced by a double behaviour of the microstrip dual-mode open-loop resonator associated with the tapped line feed structure used in the doublet filter. It is this double

behaviour that not only supports two transmission poles in the passband, when a single doublet is designed as a 2-pole bandpass filter, but also facilitates two transmission zeros at finite frequencies resulting in a quasi-elliptic function response without the need of cross coupling. It is envisaged that the doublet of this type can also be used as a basic building block for modular design of higher order quasi-elliptic function filters. A four-pole filter of this has been demonstrated.

A three-pole parallel feed microstrip dual-mode open-loop resonator filter that exhibits a quasi-elliptic function response has been investigated in Section 5.3. By forming two dual-mode resonators in parallel feed configuration, the odd modes of the proposed parallel feed configuration filter are coincided, resulting a 3-pole quasi-elliptic function response rather than a 4-pole quasi-elliptic function response by cascading in series configuration. Hence, less insertion loss can be achieved with a better mid-band performance. Moreover, by relocating the modal frequencies, a dual-band operation of the proposed parallel feed filter can be obtained. An experimental filter of this type has been designed, fabricated and tested.

A new type of compact dual-band filters that consist of non-degenerate dual-mode microstrip slow-wave open-loop resonators has been addressed in Section 5.4. Different feed schemes and coupling structures have been investigated. Both simulated and experimental results have been described. It has been shown that the design of this type of dual-band filter is very flexible in terms of filter topologies and filtering characteristics.

# Chapter 6

# BANDSTOP FILTERS WITH HARMONIC SUPPRESSION

## 6.1 Introduction

Planar bandstop filters are useful for RF/microwave applications [1]. In particular, narrow-band band-reject or notch filters have become more and more important in most microwave communications and radar systems as there exist more unwanted signals or interference at air interfaces. This has stimulated new developments of microstrip band reject filters [70]-[73]. Usually, transmission line bandstop filters comprised of distributed resonators would have encountered a restriction on the extent of the upper passband because of spurious response. Recent efforts have been made to overcome this restriction using a new design technique [17]-[18], in which both directly coupled stub and two types of parallel-coupled line designs with very wide upper passband have been demonstrated.

In this chapter, an alternative new technique is proposed, which is to cancel or suppress the first spurious mode by employing coupled three-section stepped impedance resonator (SIR), leading to a wide upper passband. In general, the purpose of SIR is to achieve a higher spurious frequency response or to have a compact size of circuit [75], [80], [88]. However, for the bandstop filter of this type, the three-section SIR is also employed to control the bandwidth of the first spurious mode. A comprehensive study of the building block for the proposed filter configuration shown in Figure 6-1, covering theoretical works to explain the mechanism behind achieving a wide upper passband for this type of bandstop filter.

A stripline filter design and a microstrip filter design are detailed to verify the theory. In addition, as a preliminary investigation, the microstrip bandstop filter is tuned electronically using ferroelectric thin film varactors.

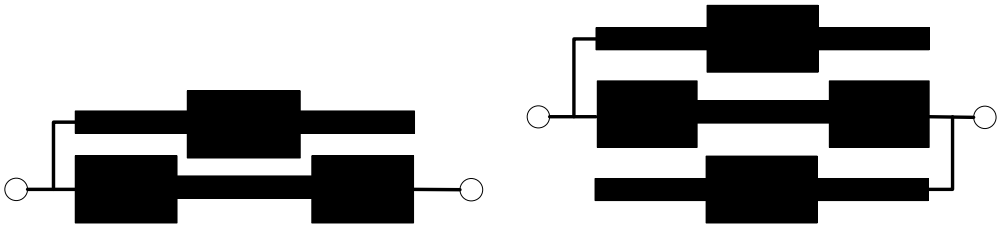

(a) (b)

Figure 6-1. The configuration of proposed filter. (a) One-section. (b) Cross-coupled section.

## 6.2 Theory and Design Equations

To cancel or suppress the first spurious mode of the proposed bandstop filter, both the three-section stepped impedance resoantor (SIR) effects and the coupling between the SIR and the main transmission line need to be considered. Ther are investigated theorectically as below.

### *6.2.1 Effects of stepped impedance resonator*

The purpose of using three-section SIR is to control the bandwidth of the first spurious frequency response, and then leading to its cancellation. For this reason, the characteristics of the SIR are analysed as follows to specify the configurations required for the proposed bandstop filter.

The SIR is one-quarter wavelength-type resonator at its fundamental resonant frequency for the proposed bandstop filter, which is displayed in Figure 6-2. The SIR is constructed by two different characteristic impedance lines, $Z_m$ and $Z_1$, with electrical length of $\theta_m$ and $\theta_1$. The total electrical length is denoted by $\theta_r$ with $\theta_r = \theta_m + 2\theta_1$.

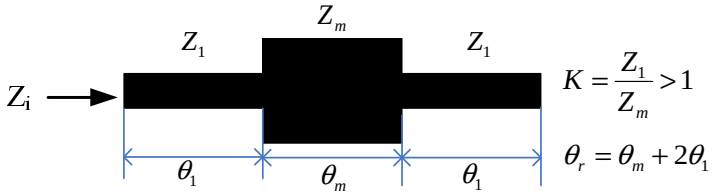


(a)

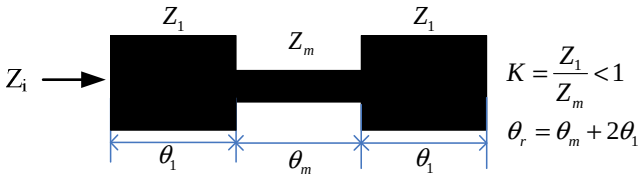


(b)

Figure 6-2. The structures of SIR. (a) $K > 1$ and (b) $K < 1$.

#### *6.2.1.1 Fundamental resonance condition*

The input impedance $Z_i$ of the SIR is given as follows:

$$Z_i = jZ_1 \cdot \frac{(1+K^2)\cdot(\tan\theta_m \cdot \tan\theta_1) - K(1-\tan^2\theta_1)}{2K\tan\theta_1 + \tan\theta_m(K^2 - \tan^2\theta_1)} \qquad (6.1)$$

where $K$ is the impedance ratio, $K = Z_1 / Z_m$.

The fundamental resonance condition can be obtained by applying:

$$Z_i = 0 \qquad (6.2)$$

From (6.1) and (6.2), the fundamental resonance condition is determined as (6.3)

$$\frac{\tan\theta_m \cdot \tan\theta_1}{1-\tan^2\theta_1} = \frac{K}{1+K^2} \qquad (6.3)$$

For $\theta_r = \theta_m + 2\theta_1$, we can derive from (6.3) that

$$\tan\theta_r = \frac{2A + \tan^2\theta_m}{\tan\theta_m(1-2A)} \qquad (K \neq 1) \qquad (6.4)$$

$$\theta_r = \frac{\pi}{2} \qquad (K = 1)$$

where

$$A = \frac{K}{1+K^2}$$

Using (6.4), the relationship between $\theta_r$ and $\theta_m$ is plotted in Figure 6-3, which shows that either the larger $K$ for the SIR of Figure 6-1(a) or the smaller $K$ for the SIR of Figure 6-1(b) is, the shorter electrical length of the resonator is. The minimum value for $\theta_r$ with varying $K$ occurs when

$$\theta_m = \tan^{-1}\sqrt{\frac{2K}{1+K^2}} \qquad (6.5)$$

which can be obtained by differentiating (6.4) with respect to $\theta_m$.

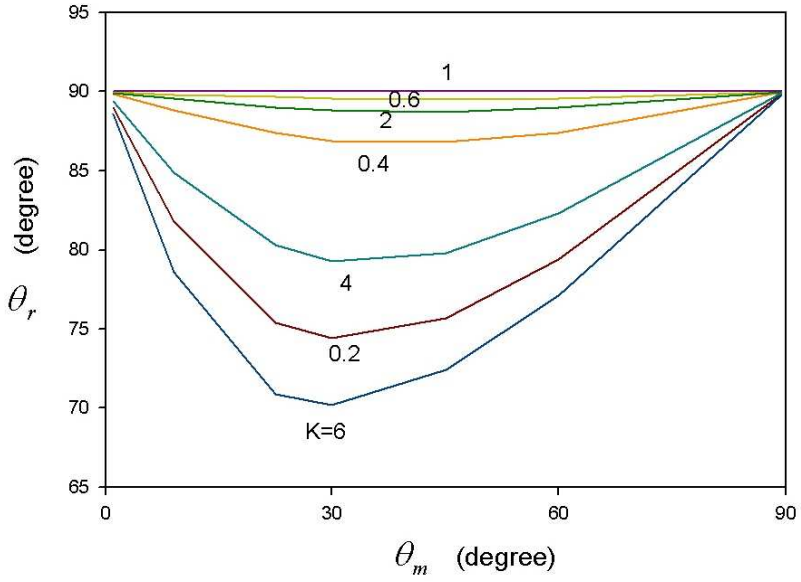


Figure 6-3. Resonance condition of the SIR.

Next, consider $\theta_m = \theta_1 = \theta$, and the input impedance of SIR from (6.1) can be simplified as

$$Z_i = jZ_1 \cdot \frac{(1+K+K^2)\tan^2\theta - K}{\tan\theta(2K+K^2-\tan^2\theta)} \tag{6.6}$$

By applying the resonance condition of (6.2), the electrical length $\theta_0$ at the fundamental frequency $f_0$ can be determined as

$$(1+K+K^2)\tan^2\theta_0 - K = 0$$

$$\theta_0 = \tan^{-1}\sqrt{\frac{K}{1+K+K^2}} \tag{6.7}$$

#### *6.2.1.2 Spurious resonance frequency for $Z_i = 0$*

By applying the condition $Z_i = 0$, the electrical length $\theta_{sn}$ (n = 1, 2, 3…) at spurious resonance frequent $f_{sn}$ (n = 1, 2, 3…) can be derived from (6.6). For $f_{s1}$ and $f_{s2}$, it is found that

$$\theta_{s1} = \frac{\pi}{2}$$

$$\theta_{s2} = \pi - \tan^{-1}\sqrt{\frac{K}{1+K+K^2}} \tag{6.8}$$

Thus,

$$\frac{f_{s1}}{f_0} = \frac{\theta_{s1}}{\theta_0} = \frac{\pi}{2\tan^{-1}\sqrt{\frac{K}{1+K+K^2}}}$$

$$\frac{f_{s2}}{f_0} = \frac{\theta_{s2}}{\theta_0} = \frac{\pi}{\tan^{-1}\sqrt{\frac{K}{1+K+K^2}}} - 1 \tag{6.9}$$

For a desired BSF centered at the fundamental frequency, these spurious resonances generate additional transmission zeros ($S_{21}$ = 0) resulting in unwanted stopbands. In particular, the spurious resonance at $f_{s1}$ limits the bandwidth of upper passband.

#### *6.2.1.3 Transmission pole frequency for* $Z_i = \infty$

In contrast to the spurious resonance for $Z_i = 0$, the SIR produces transmission poles ($S_{11}$ = 0) when $Z_i = \infty$. By applying the condition $Z_i = \infty$, the electrical length $\theta_{pn}$ (n = 1, 2, 3…) at the transmission pole frequency $f_{pn}$ (n = 1, 2, 3…) can also be derived from (6.6). This is done by imposing the term $2K + K^2 - \tan^2\theta = 0$. For $f_{p1}$ and $f_{p2}$, we obtain

$$\theta_{p1} = \tan^{-1}\sqrt{2K + K^2}$$

$$\theta_{p2} = \pi - \theta_{p1} \qquad (6.10)$$

Therefore,

$$\frac{f_{p1}}{f_0} = \frac{\theta_{p1}}{\theta_0} = \frac{\tan^{-1}\sqrt{2K + K^2}}{\tan^{-1}\sqrt{\dfrac{K}{1 + K + K^2}}}$$

$$\frac{f_{p2}}{f_0} = \frac{\theta_{p2}}{\theta_0} = \frac{\pi - \theta_{p1}}{\theta_0} \qquad (6.11)$$

#### *6.2.1.4 Discussions*

Figure 6-4 illustrates the results of (6.9) and (6.11) against the impedance ratio $K$. It is notable that as the $K$ increase, the transmission pole frequencies $f_{p1}$ and $f_{p2}$ are getting closer with the spurious frequency $f_{s1}$ in between. As a consequence, the bandwidth of the first spurious frequency response is expected to become narrower.

This interesting phenomenon can be observed clearer in light of the circuit modeling results presented in Figure 6-5, where the single section BSF of Figure 6-5(a), terminated with $Z_0 = 50\,\Omega$, consists of a SIR with $\theta_m = \theta_1 = 30^o$, $Z_m = 30\,\Omega$, $Z_1 = KZ_m$. For the comparison, the results for $K$ = 1 is also presented.

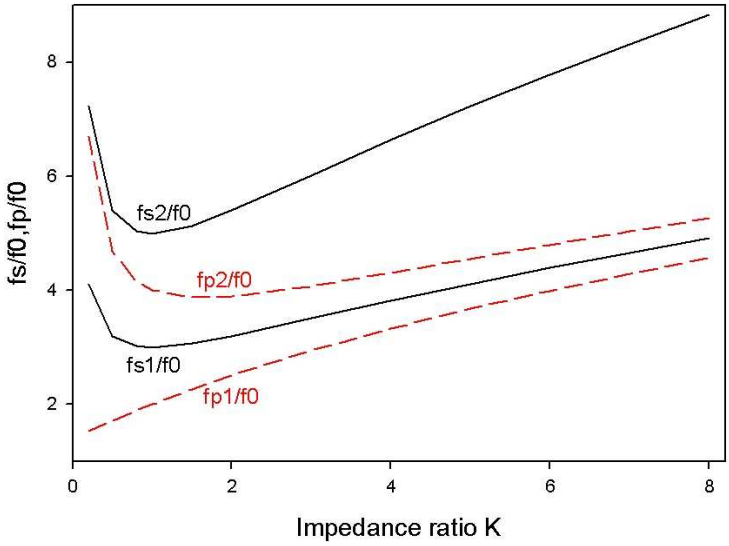


Figure 6-4. Spurious resonance frequency and transmission pole frequency of SIR against the impedance ratio of $K$ for $\theta_m = \theta_1$.

When $K$ = 1, the SIR is actually a uniform line quarter-wavelength resonator, and in this case the first spurious stopband is centered at $f_{s1}/f_0 = 3$ and the first non-zero frequency transmission pole occurs at $f_{p1}/f_0 = 2$. The K=1 corresponds to a case where there is no dispersion and the phase velocity is a constant. For K=3, the first spurious stopband is centred at $f_{s1}/f_0 = 3.5$, but its bandwidth is significantly reduced as can be seen from Figure 6-5(b). In this case, the two transmission pole frequencies, referring to Figure 6-5(c), are located at $f_{p1}/f_0 = 2.9$ and $f_{p2}/f_0 = 4.1$, respectively. Hence, it is evident that when these two transmission pole frequencies are close, the bandwidth of the first spurious response becomes small. As a matter of fact, for K>1, the step impedance discontinuities are introduced which cause a dispersion in the transmission line resonator [1] so that the phase velocities are different at $f_{s1}$, $f_{p1}$ and $f_{p2}$.

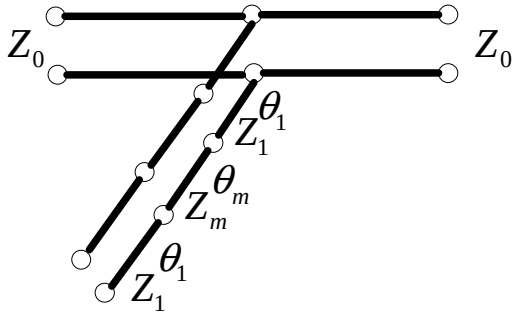


(a)

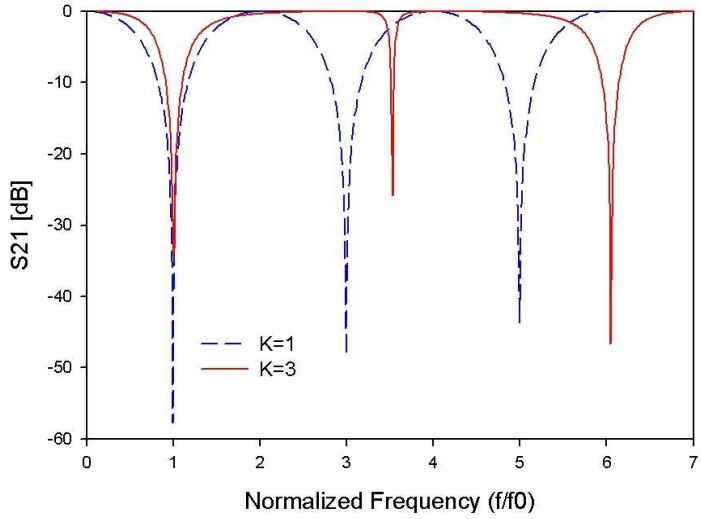


(b)

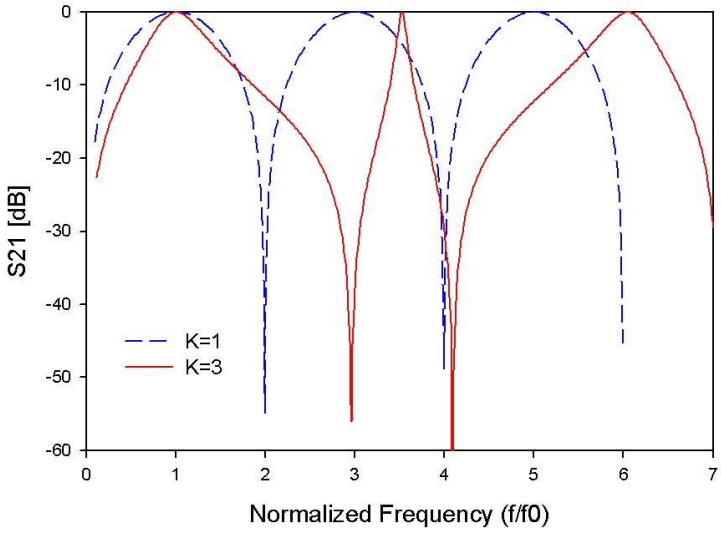


(c)

Figure 6-5. (a) The single section BSF circuit. (b) Magnitude of $S_{21}$. (c) Magnitude of $S_{11}$.

For the filter deigns discussed later on, Figure 6-6 displays the bandwidth varying with $Z_m$ while $K$ is kept constant for the bandstop filter circuit of Figure 6-5(a). The smaller the $Z_m$, the larger is the stopband bandwidth.

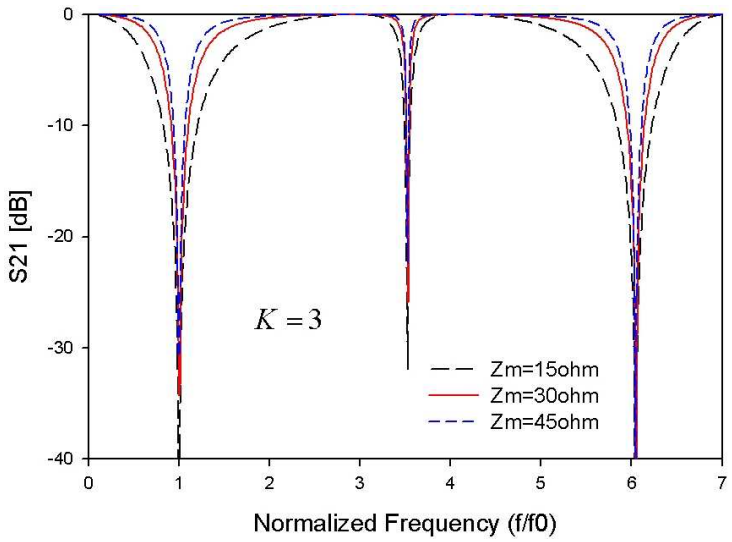


Figure 6-6. Stopband bandwidth change for varying with $Z_m$.

### *6.2.2 Coupling effects*

According to the analysis above, with large $K$, the first spurious mode of an un-coupled SIR can be minimised. However, for a perfect cancellation of this spurious mode, the coupling between the SIR and the main transmission line, as shown in Figure 6-1(a), plays an important role as well, in particular when a large $K$ is difficult to implement in a practical design. Moreover, the primary bandwidth at the fundamental frequency may be controlled by varying $Z_m$ while keeping the cancellation of the first spurious mode. These effects are demonstrated as follows with the help of Microwave Office tool [89].

#### *6.2.2.1 Spurious suppression*

To investigate the coupling effect on the suppression of the first spurious response, consider a stripline bandstop filter consisting of one section coupled SIR and using a dielectric substrate with a relative dielectric constant of 3.02 and a thickness of 1.52 mm. Figure 6-7(a) is the circuit model for the filter and Figure 6-7(b) shows its frequency responses for the step impedance ratio $K = 3$. The gap between the SIR and the main transmission line is denoted by S.

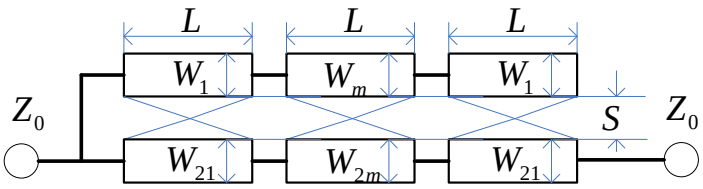


(a)

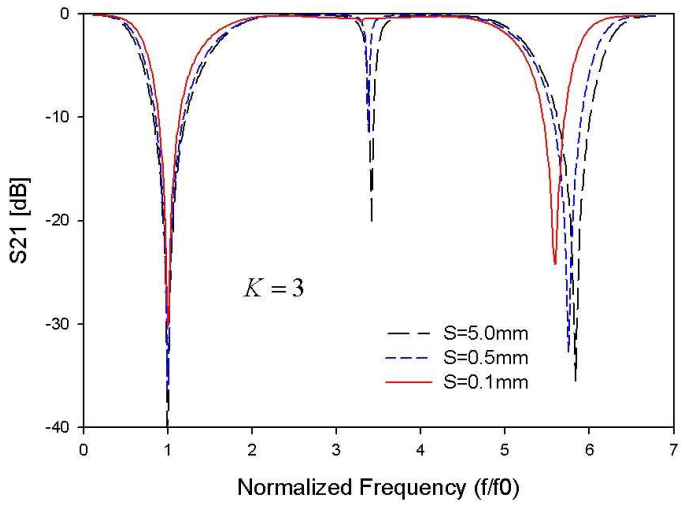


(b)

Figure 6-7. (a) Circuit model of one-section BSF with a SIR coupled to the main line. (b) Frequency responses varying with the coupling gap *S* for *K* =3. (where $W_m = 2.4\,\text{mm}, W_{2m} = 0.2\,\text{mm}, W_{21} = 0.48\,\text{mm}, L = 14.3\,\text{mm}, Z_0 = 50\,\Omega$)

By comparing the results shown in Figure 6-7(b), it can be concluded that

i. The narrower the gap (*S*) is, the narrower is the bandwidth of the first spurious mode.

ii. The cancellation or suppression of the first spurious response depends on both the SIR ( $K$ ) and the coupling gap ($S$), for larger $K$ , the gap ($S$) may be chosen not too small, so that it is easy for fabrication.

iii. The bandwidth of the fundamental frequency response is also affected by the coupling, but insignificantly.

Following the discussion in Section 6.2.1, in fact, the coupling has an additional effect on the phase velocities at $f_{s1}$, $f_{p1}$ and $f_{p2}$. This effect adjusts these phase velocities in such a way that $f_{s1}$, $f_{p1}$ and $f_{p2}$ occur at the same frequency so that the spurious at $f_{s1}$ can be completely suppressed.

#### *6.2.2.2 Bandwidth control*

The bandwidth of the fundamental frequency response may be controlled by different $Z_m$ ($W_m$) with the same impedance ratio $K$ while keeping the first spurious response suppressed. This is demonstrated in Figure 6-8, using the same circuit model of Figure 6-7(a).

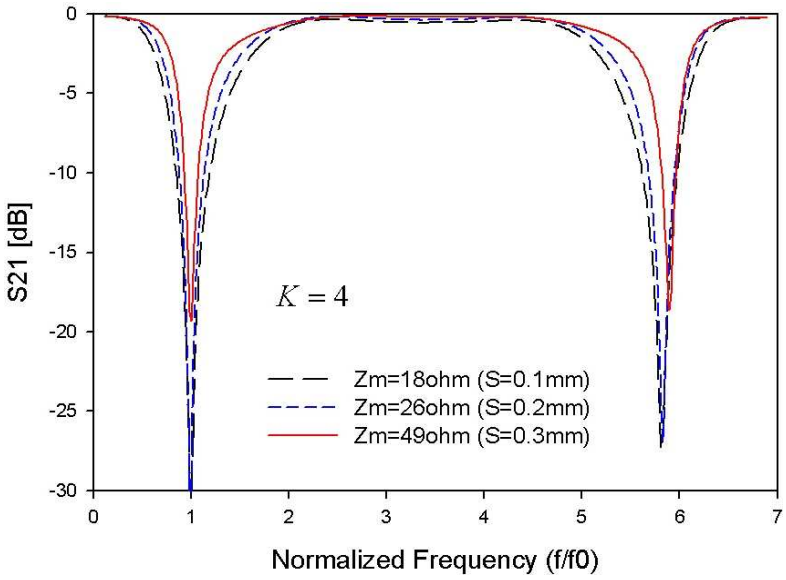


Figure 6-8. Different bandwidth varying with $Z_m$ .

It should be noticed that the cancellation condition is changed with different $Z_m$, so the gap (S) needs to be readjusted accordingly as indicated. Figure 6-8 shows that for a wide bandwidth, low characteristic impedance of $Z_m$ and strong coupling are required, whereas for narrow band, the requirement is opposite.

### *6.2.3 Design procedure*

Based on the above analysis and discussion, a useful procedure for the proposed filter design is developed. For a given filter specification of stopband centre frequency and fractional bandwidth, the following desired circuit parameters are to be determined, which are $W_m$, $W_1$, $W_{2m}$, $W_{21}$, $S$ and $L$ as indicated in Figure 6-7(a). The design procedure is outlined below:

(a) For given a required fractional bandwidth, $Z_m$ can be estimated from Figure 6-6, which should be chosen by considering the coupling effect as well. Because the coupling effect can narrow the bandwidth slightly, $Z_m$ should be chosen smaller than the one found in Figure 6-6. This $Z_m(W_m)$ then is set as initial value for optimisation later on.

(b) The impedance ratio $K$ may be set larger than 3, so that the gap (S) can be chosen not too small for spurious suppression as well as easy fabrication.

(c) After the impedance ratio $K$ is determined, the electrical length of the SIR can be derived from Figure 6-3 ($\theta_m$=30˚).

(d) Initially, $Z_{21}$ for $W_{21}$ can be set slightly smaller than 50 Ω and $Z_{2m}$ for $W_{2m}$ can be set slightly larger than 50 Ω.

(e) For multi-section design, all sections may be set with the same parameters first.

(f) After all the initial values of the circuit parameters are determined, the optimisation can be performed for the cancellation of the first spurious stopband to obtain a desired frequency response.

## 6.3 Filter Design (Stripline)

For demonstration, a two-section proposed stripline filter, whose circuit model is shown in Figure 6-9(a), is designed on a dielectric substrate with a relative dielectric constant of 3.02 and a thickness of 1.52 mm. The filter specification is

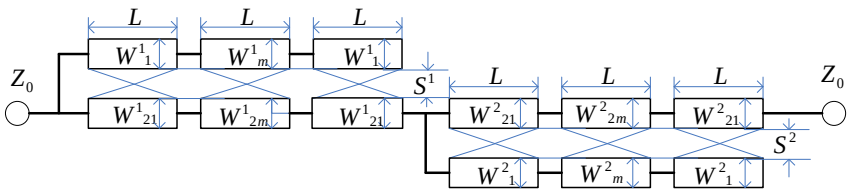


(a)

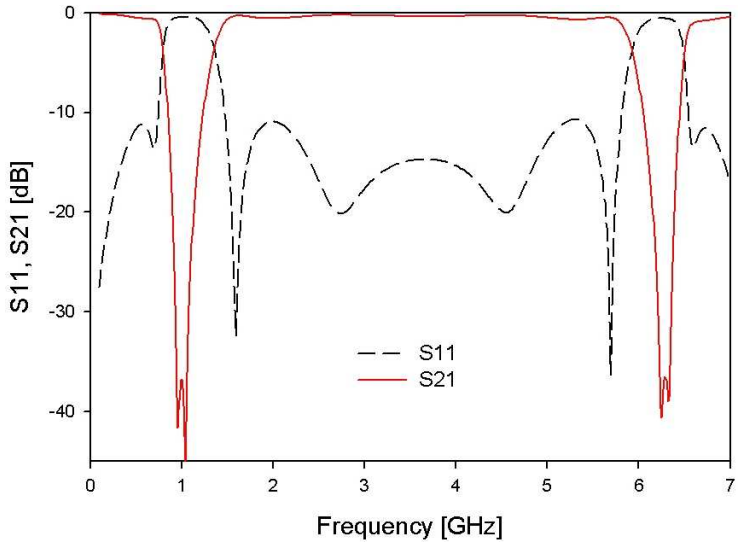


(b)

Figure 6-9. (a) Circuit model of two-section proposed stripline filter. (b) Its frequency responses.

Stopband centre frequency: 1 GHz

Fractional bandwidth (3 dB): 60%

By employing the design procedure above, for the required fractional bandwidth, $Z_m$ can be estimated as 20 Ω ($W_m$ = 3.5 mm), the impedance ratio $K$ is chosen to be about 4. For a centre frequency of 1 GHz, the electrical length of the SIR can be derived from Figure 6-3 with $\theta_m$ =30˚, which is found as 79.3˚. In our design, the electrical length of each section of the SIR can then be calculated as $\theta_m = \theta_1 = \theta_r / 3$=26.3˚. For the given substrate, the corresponding physical length (L) can be derived as 12.6 mm. As the SIR is coupled to the main transmission line with a gap (S) of 0.2 mm initially, the actual value of L would be slightly shorter than 12.6 mm, which is found to be 11 mm by performing the circuit optimisation [89]. $Z_{21}$ and $Z_{2m}$ are set with the initial values of 45 and 55 Ω, respectively. By performing the circuit optimisation for the cancellation of the first spurious mode, all the circuit parameters are determined. The initial and optimised circuit parameters are listed in Table 6-1. Note that the final circuit parameters for Sections 1 and 2 are different because the filter structure of Figure 6-9(a) is asymmetrical. Figure 6-9(b) shows the performance of the designed filter. It can clearly be observed from Figure 6-9(b) that the first spurious mode is cancelled, leading to a very wide upper passband up to 6.2 times the fundamental stopband centre frequency with a return loss of better than 11 dB.

**TABLE 6-1**

**Initial and optimized circuit parameters of the two-section stripline filter (all dimensions are in millimeter).**

| Section one | $W^1{}_m$ | $W_1^1$ | $W^1{}_{2m}$ | $W^1{}_{21}$ | $S^1$ | $L$ |
|---|---|---|---|---|---|---|
| Initial value | 3.5 | 0.35 | 0.82 | 1.15 | 0.2 | 11 |
| Optimized value | **2.4** | **0.14** | **0.56** | **0.7** | **0.4** | **11.8** |
| Section two | $W^2{}_m$ | $W_1^2$ | $W^2{}_{2m}$ | $W^2{}_{21}$ | $S^2$ | $L$ |
| Initial value | 3.5 | 0.35 | 0.82 | 1.15 | 0.2 | 11 |
| Optimized value | **2** | **0.21** | **0.51** | **0.82** | **0.27** | **11.8** |

In order to reduce the circuit size of the two-section stripline filter, the symmetrical topology of the cross-coupled section bandstop filter introduced in Figure 6-1(b) can be used. Its circuit model is presented in Figure 6-10 with the same circuit parameters for upper and lower sections. Its initial and optimised circuit parameters are list in Table 6-2.

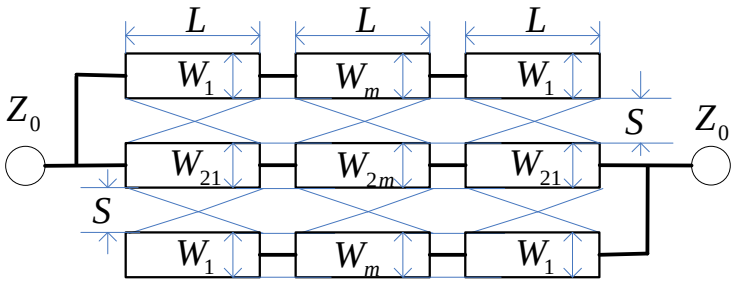


Figure 6-10. Circuit model of cross-coupled section proposed stripline filter.

**TABLE 6-2**

**Initial and optimized circuit parameters of the cross-coupled section stripline filter (all dimensions are in millimeter).**

| Upper and Lower Section | $W_m$ | $W_1$ | $W_{2m}$ | $W_{21}$ | $S$ | $L$ |
|---|---|---|---|---|---|---|
| Initial value | 3.5 | 0.35 | 0.82 | 1.15 | 0.2 | 11 |
| Optimized value | **2.2** | **0.2** | **0.4** | **0.7** | **0.3** | **11.8** |

The stripline filter design is verified by both EM simulation [79] and experiment. Figure 6-11(a) shows the layout of the fabricated stripline filter before assembling, whereas Figure 6-11(b) shows the filter after the assembly. The overall circuit size of the stripline filter is 35.4 mm×5.4 mm. The EM simulated and measured responses of the filter are plotted in Figure 6-11(c). The measurement was performed using Agilent 8510B network analyser. In general, both simulated and measured results are in good agreement. Slight discrepancy is mainly because of the assembly tolerance. Nevertheless, the experimental filter demonstrates good performance of the proposed

bandstop filter. As can be seen, the measured primary stopband is centred at 1.0 GHz, while the first significant spurious response is observed at about 6 GHz, resulting in a very wide upper passband with a ratio of 6:1.

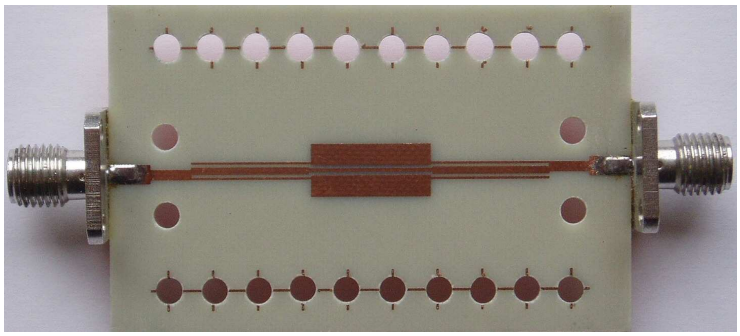

(a)

（b）

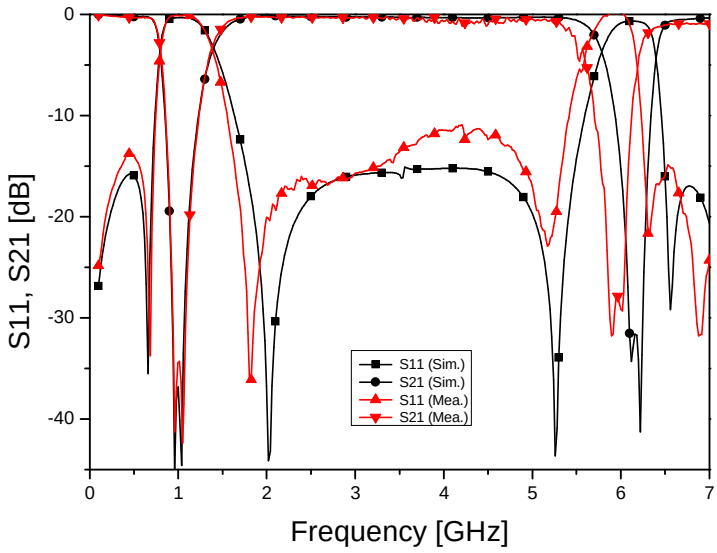


(c)

Figure 6-11. Photograph of fabricated stripline bandstop filter. (a) Before assembling. (b) After the assembly. (c) Simulated and Measured frequency responses.

## 6.4 Filter Design (Microstrip)

For further demonstration, the proposed filter is implemented using microstrip line. The proposed microstrip BSF is based on a dielectric substrate with a relative dielectric constant of 3.02 and a thickness of 0.76mm.

Filter specifications:

Stop band center frequency: 1GHz
Fractional bandwidth (3dB): 26%

With the same design procedure as stripline filter, for a fractional bandwidth of 26%, $Z_m$ is estimated as 58 Ω, the impedance ratio $K$ is chosen to be about 3. By performing the optimization, the desired circuit parameters are derived and present in Table 6-3 using the same structure as Figure 6-10. Its frequency responses are displayed in Figure 6-12.

**TABLE 6-3**

**Initial and optimized circuit parameters of the cross-coupled section microstrip filter (all dimensions are in millimeter).**

| Upper and Lower Section | $W_m$ | $W_1$ | $W_{2m}$ | $W_{21}$ | $S$ | $L$ |
|---|---|---|---|---|---|---|
| Initial value | 1.5 | 0.24 | 1.6 | 2.2 | 0.2 | 15.2 |
| Optimized value | **1.4** | **0.2** | **1.4** | **2.0** | **0.2** | **16** |

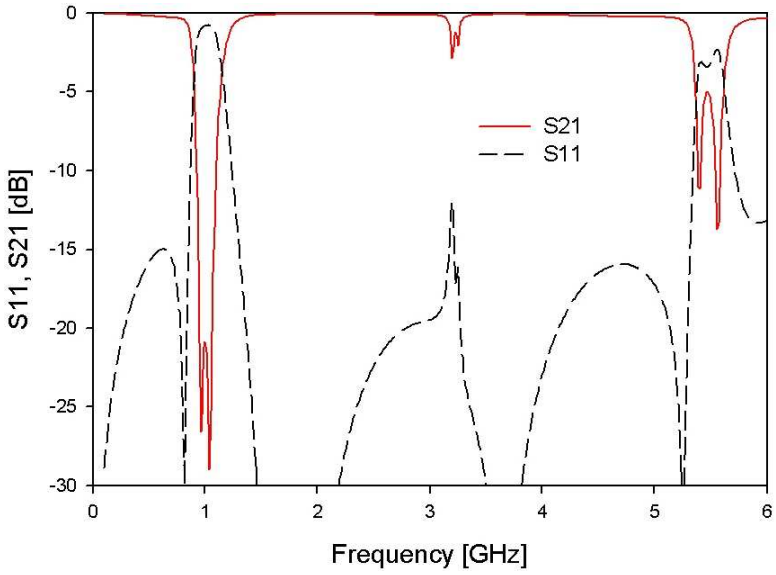


Figure 6-12. Circuit modeling responses of cross-coupled section proposed microstrip filter.

It is obvious that the first spurious mode is not cancelled, this may due to the asymmetrical passband response of the microstrip filter, which has different phase velocity of the c mode and $\pi$ mode of the asymmetrical coupled lines. To overcome this, an inductively compensated method [90] is introduced to eliminate the first spurious mode for the proposed microstrip filter by equalizing the different phase velocities, shown in Figure 6-13(a).

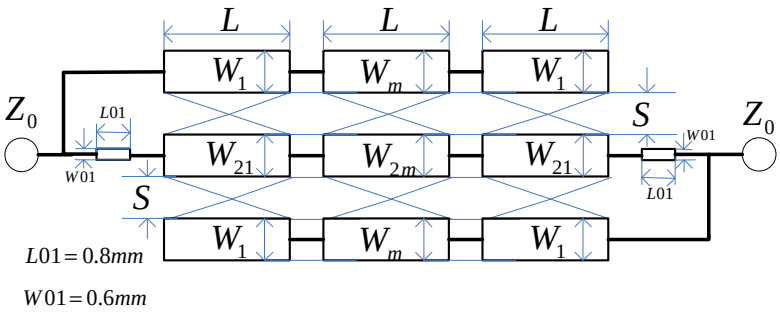


(a)

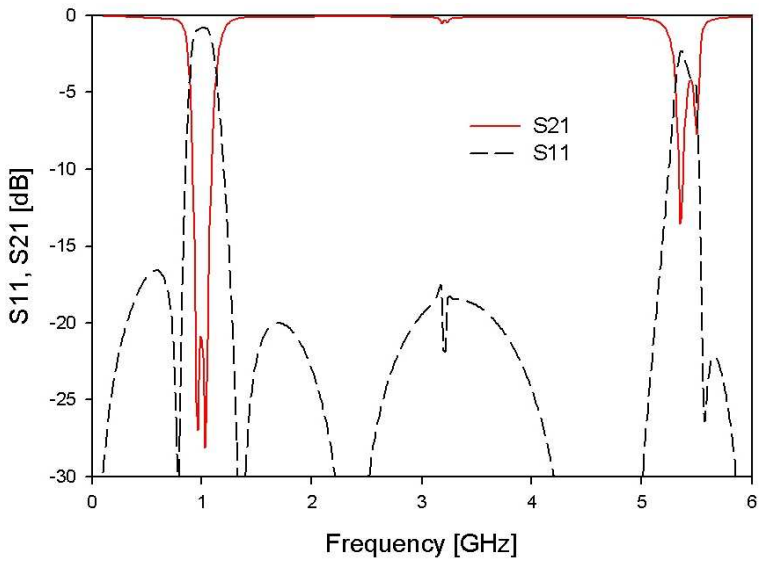


(b)

Figure 6-13. (a) Circuit model of proposed cross-coupled SIR microstrip filter. (b) Its frequency responses.

The two small transmission lines at each end can be considered as inductive loading for the compensation of the different phase velocities. The circuit parameters remain the same as in Table 6-3, apart from the two small transmission lines. By performing the optimization for the cancellation of the first spurious mode, the parameter for this two transmission lines are determined as shown in Figure 6-13(a) and the desired responses are given in Figure 6-13(b).

To verify this circuit model results, the proposed cross-coupled section microstrip filter is simulated and fabricated. The results are displayed in Figure 6-14(b) and the photograph of the fabricated microstrip filter is given in Figure 6-14(a) with an overall circuit size of 49.6 mm×4.6 mm. The measured bandstop filter has a 3-dB bandwidth of 250 MHz centered at the center frequency of 1.0 GHz, and it shows no spurious responses up to 4.92 GHz, which is in good agreement with both the circuit modeling and EM simulation.

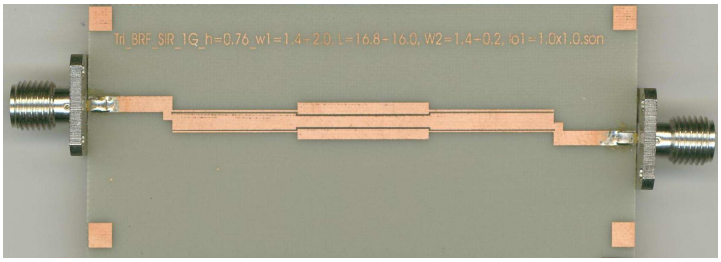

(a)

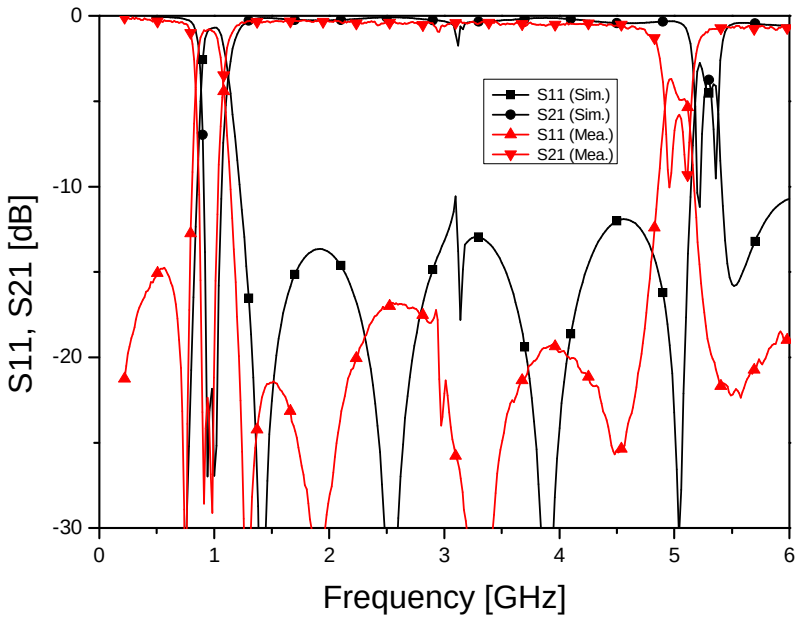


(b)

Figure 6-14. (a) Photograph of fabricated microstrip BSF. (b) Simulated and measured frequency responses.

## 6.5 Tunable Filter Design (Microstrip)

It is of interest to make this type of filter electronically tunable. A critical issue is to tune the filter's center frequency ( $f_0$ ) while keeping the first spurious mode cancelled. Full-wave EM simulations have been carried out to investigate this issue. Figure 6-15(a) presents a layout of a microstrip coupled stepped-impedance resonator (SIR) bandstop filter with a capacitance of 1 pF loaded at different locations of the SIR, i.e., location A to F.

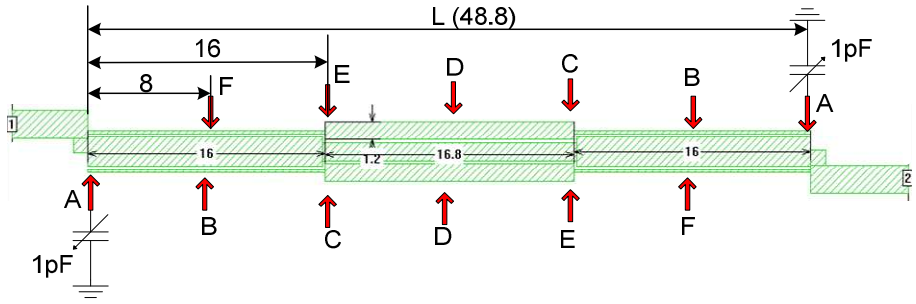


(a)

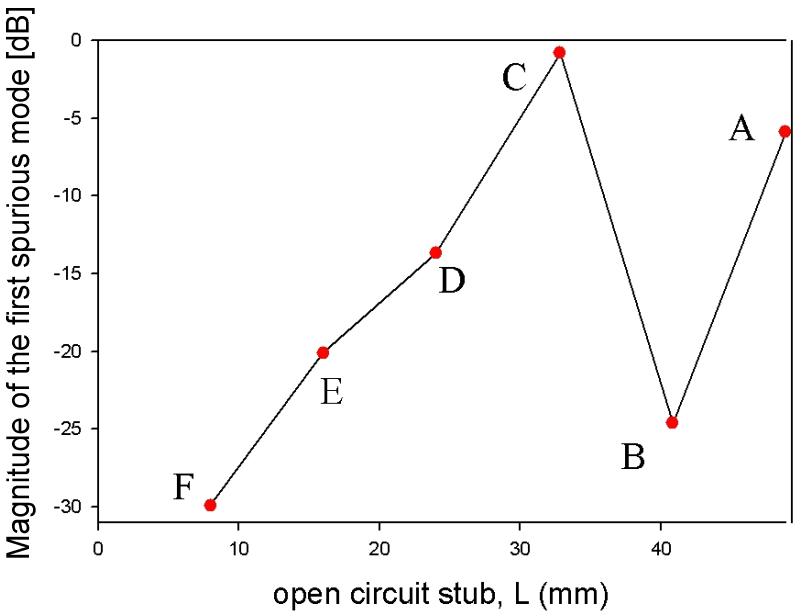


(b)

Figure 6-15. (a) Layout of the microstrip bandstop filter with loading capacitance. (b) Its first spurious mode cancellation varies with different locations while loading capacitance of 1 pF. (All dimensions are in millimetre)

By performing full-wave EM simulation [79], the magnitude of the first spurious mode against the location of the loading capacitance is plotted in Figure 6-15(b). It is obvious that location C has the best the first spurious mode cancellation. The reason behind this can be explained by the charge distribution at the frequency of the first spurious mode shown in Figure 6-16.

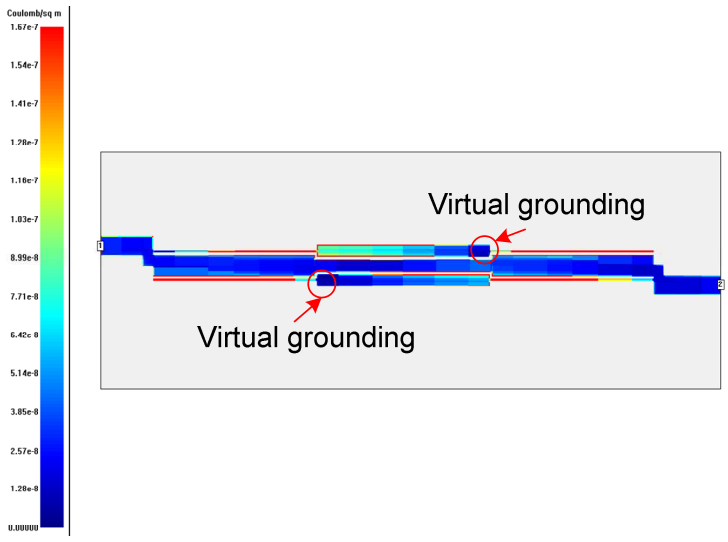


Figure 6-16. Charge distribution of the first spurious mode of the filter.

It can be observed that location C can be considered as a virtual ground for the first spurious mode of the SIR, which implies that the loading capacitance has minimum affect to the first spurious mode at this location. By changing the loading capacitance from 1 to 2 pF, the tuning range of the bandstop filter (fundamental frequency) varies with the different locations has also been investigated and given in Figure 6-17.

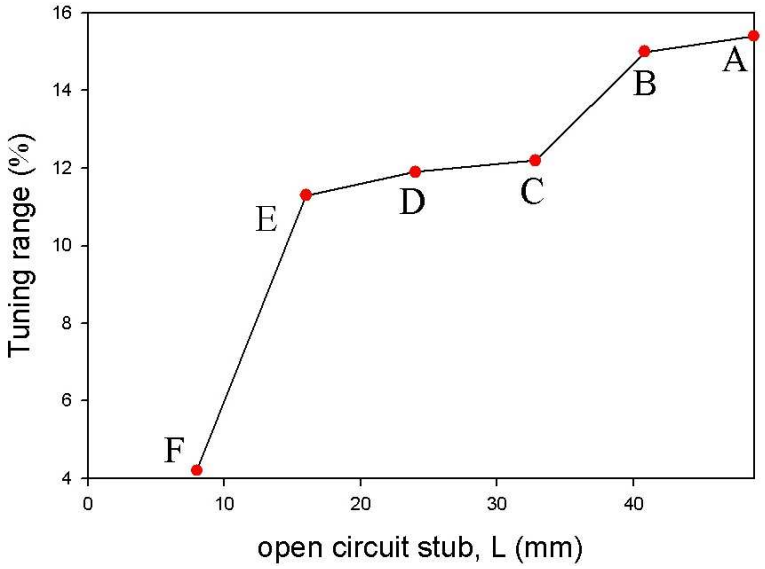


Figure 6-17. The tuning ranges against the different locations with the loading capacitance varies from 1 to 2 pF.

Note that the tuning range may be defined by

$$\text{Tuning range} = \frac{f_{tune}^{\max} - f_{tune}^{\min}}{f_{tune}^{\max}} \times 100(\%) \qquad (6.12)$$

where $f_{tune}^{\max}$ and $f_{tune}^{\min}$ denote the two edge frequencies within the tuning range.

Figure 6-17 shows that location A has the largest tuning range, but for a better cancellation of the first spurious mode, location C is chosen for tuning this type of filter.

A PST varactor chip [91] shown in Figure 6-18(a) is used for tuning the filter in our design. Two schemes of implementation of the PST varactor chip are investigated and displayed in Figure 6-18(b) and (c).

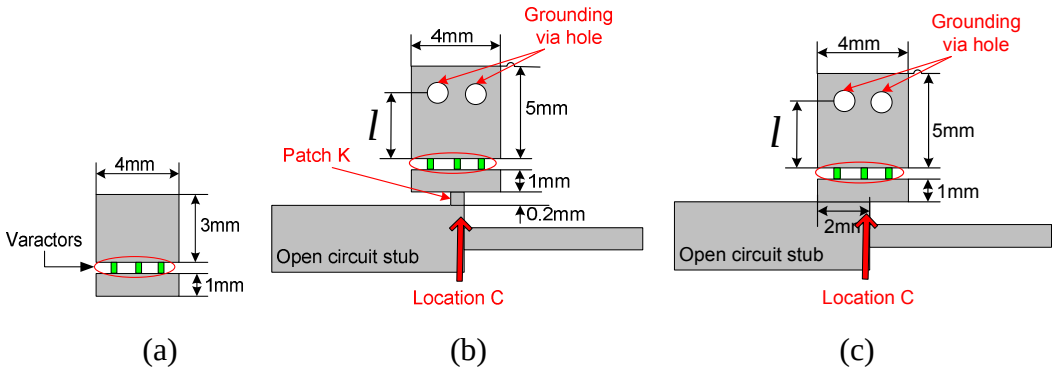


Figure 6-18 (a) Layout of PST varactor chip. (b) Implementation scheme A. (c) Implementation scheme B.

The capacitance value for the PST varactor chip is estimated to be 1 to 2 pF. By performing full-wave EM simulation, the tuning range and 3dB-upper passband of the bandstop filter for the two implementation schemes are computed and presented in Table 6-4. Where 3dB-upper passband is defined by

$$\text{3dB-upper passband} = \frac{f_{3dB}^{upper\_passband}}{f_0}(f_0) \qquad (6.13)$$

where $f_{3dB}^{upper\_passband}$ is the upper passband frequency of the bandstop filter at 3dB.

**TABLE 6-4**

**Comparison of the implementation scheme A and B.**

| Implementation scheme | Tuning range | 3dB-upper passband |
|---|---|---|
| A | 13.9% | 4.47 $f_o$ |
| B | 12.5% | 4.87 $f_o$ |

Table 6-4 shows that scheme B has a wider 3dB-upper passband up to 4.87 $f_0$, while scheme A has a better tuning range 13.9%. This is because in scheme A, the PST varactor chips are loaded more close to the end of the open circuit stub as present in Figure 6-18(b), but has more loading effect (small patch K) for the resonators, resulting in a narrower 3dB-upper passband performance.

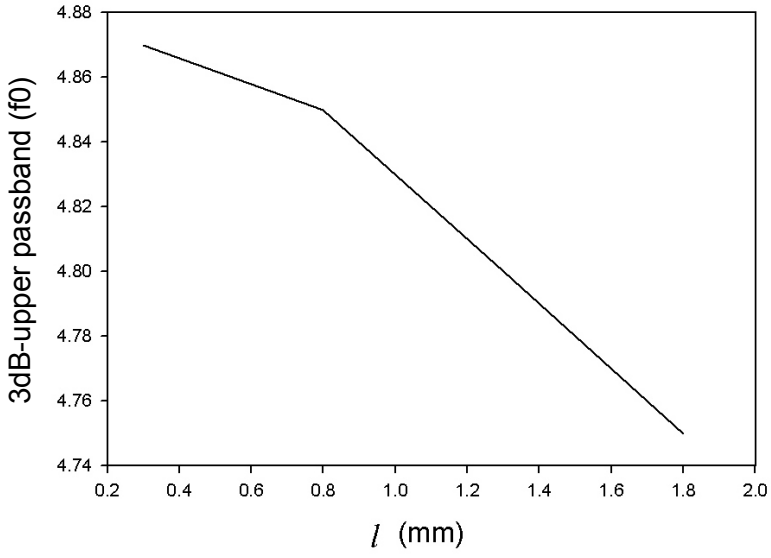


Figure 6-19. 3dB-upper passband varies with different locations of grounding via holes.

It is noticed that the location of grounding via hole for the PST varactor chip can also affect the 3dB-upper passband performance, which is investigated by using full-wave EM simulation with a loading capacitance of 1pF, shown in Figure 6-19. It is clear that the grounding via holes need to be located as near as possible to the edge of the PST varactor chip ($l \to 0$ see Figure 6-18(b)) to achieve a wider 3dB-upper passband.

From the investigation above, it is found that the location of loading capacitance plays an important role in the design, and hence there is an optimum location (location C) to tune the frequency of the desired rejection band, and in the meantime not to excite the third spurious resonance. To verify this experimentally, a tunable BSF of this type is designed and fabricated on a substrate with a relative dielectric constant of 3.02 and a thickness of 0.76mm. Figure 6-20 shows the photograph of the fabricated filter with an overall circuit size of 49.6 mm×16.6 mm. Two ferroelectric thin film varactors fabricated using Lead-Strontium-Titanate (PST) materials [91] are implemented in the optimum location for electronically tuning. The experimental results, obtained using Agilent 8510B network analyzer, are plotted in Figure 6-21. When the DC bias voltage across the PST varactors is changed from 0 to 28V, the center frequency of the desired rejection band is tuned over 60 MHz, as can be seen from Figure 6-21(a). It is more interesting to see from Figure 6-21(b) that there is a good suppression of the third spurious mode while tuning.

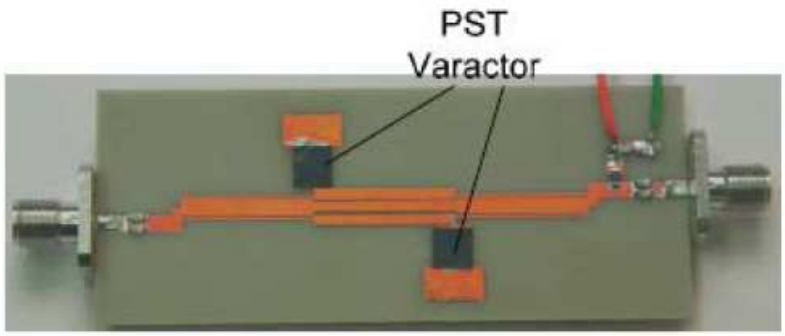


Figure 6-20. Photograph of the fabricated tunable BSF using PST varactors.

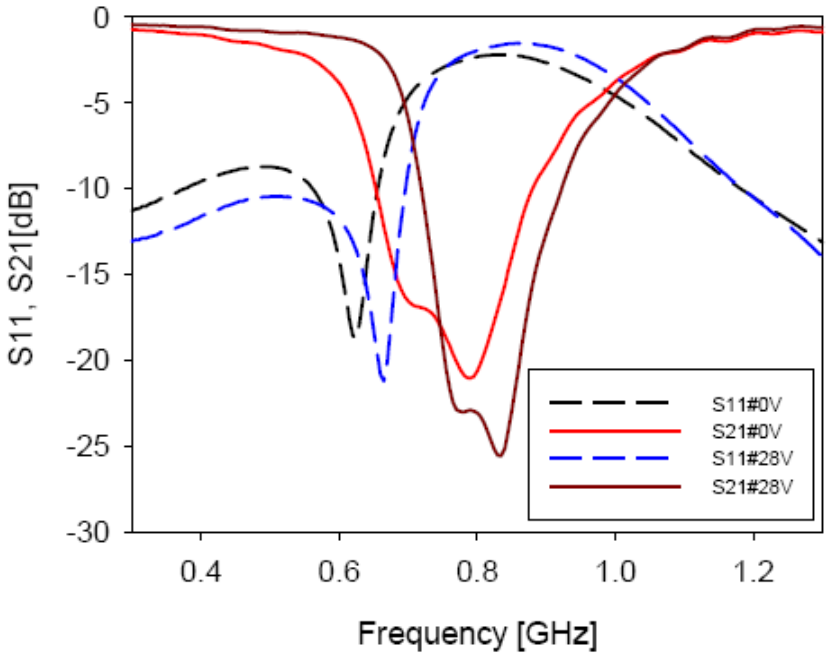


(a)

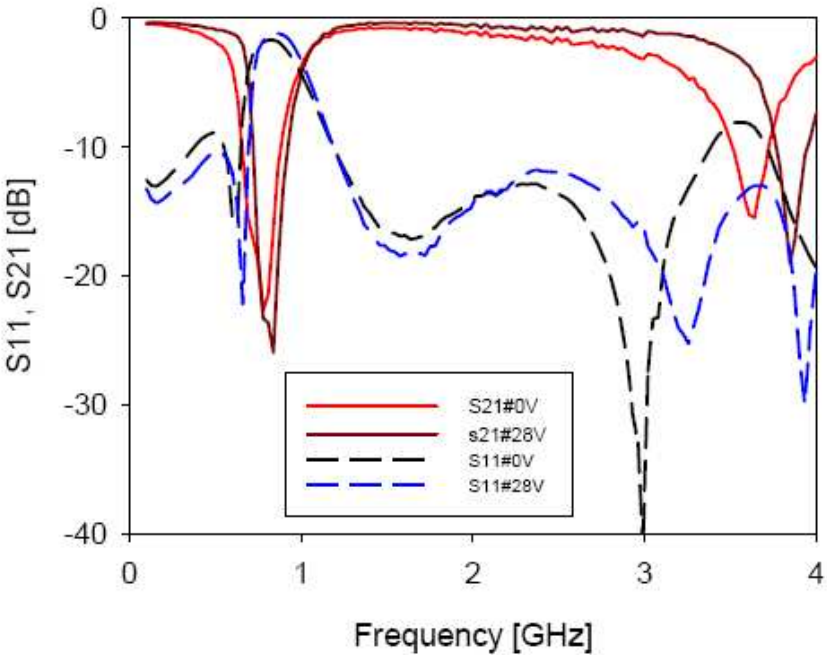


(b)

Figure 6-21. Measured response of the tunable BSF. (a) Narrow band. (b) Wideband.

## 6.6 Summary

A novel type of wide spurious-free planar bandstop filters using coupled stepped impedance resonators has been introduced. A wide upper passband of this type of

bandstop filter is attainable because the cancellation of the first spurious resonance occurs when two transmission poles coincide with the first spurious mode (transmission zero) by properly choosing the impedance ratio $K$ of the SIR and the gap between the SIR and the main transmission line. The effects of the stepped impedance resonator and the coupling between the SIR and the main transmission line have been analysed theoretically. According to this analysis, the design procedure of this type of bandstop filter has been developed.

To verify the theory, a proposed stripline filter has been demonstrated experimentally with achieving an upper passband width of up to six times the fundamental stopband centre frequency at 1.0 GHz with 3-dB fractional bandwidth of 60%. And, a microstrip bandstop filter of this type has also been designed, centring at frequency of 1 GHz with 3dB fractional bandwidth of 26%, and it shows no spurious responses up to 4.92 GHz.

Tunable microstrip bandstop filter of this type has also been investigated. It has been found that the location of loading capacitance plays an important role in maintaining the cancellation of the third spurious resonance while tuning the center frequency of the desired rejection band. This has been verified by an experimental tunable BSF using the PST varactors.

# Chapter 7

# CONCLUSIONS

## 7.1 Contributions of the thesis

A new type of varactor-tuned dual-mode microstrip open-loop resonator bandpass filter for a constant absolute bandwidth tuning has been presented [92]-[95]. This type of filter can be tuned in a simple manner by controlling the resonant frequencies of the odd-mode and even-mode since these two operating modes do not couple. In order to tune this type of dual-mode filter by using a single DC bias circuit and to achieve constant absolute bandwidth over a broad tuning range, a wideband input/output transformer network and odd/even-mode tuning rate method have been introduced. Design equations and design procedures have been presented. By applying the design procedures, two two-pole tunable bandpass filters with opposite asymmetric responses and a four-pole tunable bandpass filter with quasi-elliptic function response have been demonstrated with both simulated and experimental results. Good agreement between simulation and measurement is obtained. Both two-pole tunable bandpass filters exhibit a tuning range of 41% by using single DC bias circuits, comparing to the reported filters [11]-[12], which show a tuning range of about 10% by using two DC bias circuits. This indicates a significant improvement in the tuning range and a simpler DC bias scheme has been achieved. The proposed four-pole bandpass tunable filter shows a tuning range of 20% with high selectivity on each side of passband, which is also tuned by a single DC bias circuit.

Based on a miniature dual-mode open-loop resonator [10], three new types of dual-mode filters with novel configurations have been investigated [96]-[98].

Miniature doublet filters that exhibit quasi-elliptic function response without any cross coupling have been demonstrated [96]. It has been found that the transmission zeros are produced by a double behaviour of the microstrip dual-mode open-loop resonator associated with the tapped line feed structure used in the doublet filter. It is this double behaviour that not only supports two transmission poles in the passband, when a single doublet is designed as a 2-pole bandpass filter, but also facilitates two

transmission zeros at finite frequencies resulting in a quasi-elliptic function response without the need of cross coupling. It is envisaged that the doublet of this type can also be used as a basic building block for modular design of higher order quasi-elliptic function filters. A four-pole filter of this type has been demonstrated.

To achieve a better passband performance, parallel feed configuration of a three-pole dual-mode filter has been introduced [97]. By forming two dual-mode resonators in parallel feed configuration, the odd modes of the proposed parallel feed filter are coincided, resulting in a 3-pole quasi-elliptic function response rather than a 4-pole quasi-elliptic function response by cascading in series configuration. Hence, less insertion loss and a better mid-band performance can be achieved with a tradeoff of lower out of band rejection. Moreover, by relocating the modal frequencies, a dual-band operation of the proposed parallel feed filter can be obtained. An experimental filter of this type has been designed, fabricated and tested.

A new type of compact dual-band filters that consist of non-degenerate dual-mode microstrip slow-wave open-loop resonators has also been addressed [98]. Different feed schemes and coupling structures have been investigated. Both simulated and experimental results have been described. It has been shown that the design of this type of dual-band filter is very flexible in terms of filter topologies and filtering characteristics.

In order to achieve a wide spurious-free upper passband, planar bandstop filters using coupled stepped impedance resonators have been introduced [99]. A wide upper passband of this type of bandstop filter is attainable because the cancellation of the first spurious resonance occurs when two transmission poles coincide with the first spurious mode (transmission zero) by properly choosing the impedance ratio $K$ of the SIR and the gap between the SIR and the main transmission line. The effects of the stepped impedance resonator and the coupling between the SIR and the main transmission line have been analysed theoretically. According to this analysis, the design procedure of this type of bandstop filter has been developed. To verify the theory, a proposed stripline filter has been demonstrated experimentally with achieving an upper passband width of up to six times the fundamental stopband centre frequency at 1.0 GHz with 3-dB fractional bandwidth of 60%. And, a microstrip bandstop filter of this type has also

been designed, centring at frequency of 1 GHz with 3dB fractional bandwidth of 26%, and it shows no spurious responses up to 4.92 GHz.

Tunable microstrip bandstop filter of this type has also been investigated [100]. It has been found that the location of loading capacitance plays an important role in maintaining the cancellation of the third spurious resonance while tuning the center frequency of the desired rejection band. This has been verified by an experimental tunable BSF using the PST varactors.

## 7.2 Future works

Although most of the proposed works have been investigated intensively, there are several issues that have not been explored in this thesis due to the limit of study period. Hence, there is no doubt that further studies and efforts are needed to solve out the issues in the proposed works. They are listed below:

1. Nonresonating node effects in the proposed four-pole dual-mode tunable filter design in Chapter 4 need to be eliminated. Multilayer structures or an alternative input/output transformer network are suggested for the solution.

2. Theoretical investigation of the miniature doublet filters and the dual-band filters introduced in Chapter 5 is a potential research area.

3. As most of tunable filters are of narrow-band bandwidth tunable filters currently reported, developing theories for wide-band bandwidth tunable filters is another potential research area.

# APPENDIX

## Circuit Modeling of the Proposed Two-Pole Dual-Mode Filter

The electrical circuit modeling of the proposed two-pole dual-mode filter may be obtained using even and odd-mode analysis method [1]. By placing a short circuit or open circuit at the symmetric plane of the circuit in Figure 3-1, we obtain the circuit model for the odd-mode or even-mode, respectively, as shown in the Figure below (same as Figure 3-17). As can be seen, there is a folded asymmetric coupled line section in both circuit models. To characterize the coupled lines, let $Z_{c1}$, $Z_{\pi 1}$, $Z_{c2}$, $Z_{\pi 2}$ denote the $c$ and $\pi$ modes characteristic impedance of the coupled lines; $\theta_1$ is the electrical length of the coupled lines.

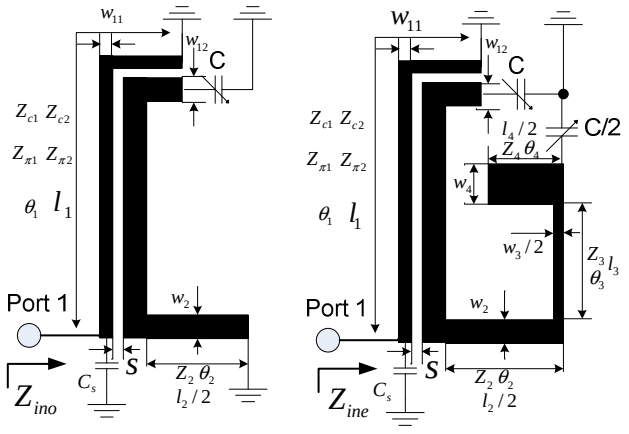


(a) (b)

Figure 3-17. Circuit model of (a) odd-mode and (b) even-mode.

The two-port scattering parameters ($S_{11}$ and $S_{21}$) of the filter may be found by

$$S_{11} = \frac{S_{11e} + S_{11o}}{2} \qquad (1)$$

$$S_{21} = \frac{S_{11e} - S_{11o}}{2} \qquad (2)$$

where $S_{11e}$ and $S_{11o}$ denote the input reflection coefficient of even mode and odd mode, which can be given by

$$S_{11e/o} = \frac{Z_{ine/o} - Z_0}{Z_{ine/o} + Z_0} \qquad (3)$$

where $Z_{ine}$ and $Z_{ino}$ are the input impedances of the two one-port networks for even- and odd-mode respectively, as indicated in the Figure above and $Z_0$ is terminal impedance (50 Ω). By inspecting these two circuit models, the input impedances of even- and odd-mode may be expressed as

$$Z_{ine/o} = \frac{Z^1_{ine/o} \cdot \dfrac{1}{j\omega C_s}}{Z^1_{ine/o} + \dfrac{1}{j\omega C_s}} \qquad (4\text{-}1)$$

where $C_s$ is a shunt capacitor at port 1, which is used for a matching purpose. $Z^1_{ine/o}$ denotes the input impedance of the coupled lines at port 1 without $C_s$.

Since the asymmetric coupled lines can be treated as a four-port network, we may use a set of Z-parameters, i.e. $z_{11}$, $z_{12}$, $z_{13}$, $z_{14}$ and so on, to represent it [75]. The port 2 of the coupled lines is short circuited, the port 3 is terminated with a transmission line element, and the port 4 is connected with the varactor of capacitance $C$. By applying 4-port to 1-port transformation of the asymmetric coupled lines, we obtain

$$Z^1_{ine/o} = \frac{Z_{11e/o} \cdot Z_{22e/o} - Z_{12e/o} \cdot Z_{21e/o}}{Z_{22e/o} \cdot Z_{ne/o} \cdot Z_{L4}} \qquad (4\text{-}2)$$

In the equation

$$Z_{11e/o} = z_{11} \cdot z_{44} \cdot Z_{ne/o} - z_{14} \cdot z_{41} \cdot Z_{ne/o} - Z_{11k} \qquad (5)$$

$$Z_{12e/o} = z_{12} \cdot z_{44} \cdot Z_{ne/o} - z_{14} \cdot z_{42} \cdot Z_{ne/o} - Z_{12k} \qquad (6)$$

$$Z_{21e/o} = z_{21} \cdot z_{44} \cdot Z_{ne/o} - z_{24} \cdot z_{41} \cdot Z_{ne/o} - Z_{21k} \quad (7)$$

$$Z_{22e/o} = z_{22} \cdot z_{44} \cdot Z_{ne/o} - z_{24} \cdot z_{42} \cdot Z_{ne/o} - Z_{22k} \quad (8)$$

$$Z_{11k} = (z_{13} \cdot z_{44} - z_{14} \cdot z_{43})(z_{31} \cdot z_{44} - z_{34} \cdot z_{41}) \quad (9)$$

$$Z_{12k} = (z_{13} \cdot z_{44} - z_{14} \cdot z_{43})(z_{32} \cdot z_{44} - z_{34} \cdot z_{42}) \quad (10)$$

$$Z_{21k} = (z_{23} \cdot z_{44} - z_{24} \cdot z_{43})(z_{31} \cdot z_{44} - z_{34} \cdot z_{41}) \quad (11)$$

$$Z_{22k} = (z_{23} \cdot z_{44} - z_{24} \cdot z_{43})(z_{32} \cdot z_{44} - z_{34} \cdot z_{42}) \quad (12)$$

$$Z_{L4} = z_{44} + \frac{1}{j\omega C} \quad (13)$$

$$Z_{ne/o} = z_{33e/o} \cdot z_{44} - z_{34} \cdot z_{43} \quad (14)$$

$$z_{33o} = z_{33} + jZ_2 \tan\theta_2 \quad (15)$$

$$z_{33e} = z_{33} + Z_2 \frac{Z_3 \dfrac{Z_{Le} + jZ_3 \tan\theta_3}{Z_3 + jZ_{Le} \tan\theta_3} + jZ_2 \tan\theta_2}{Z_2 + jZ_3 \dfrac{Z_{Le} + jZ_3 \tan\theta_3}{Z_3 + jZ_{Le} \tan\theta_3} \tan\theta_2} \quad (16)$$

$$Z_{Le} = \frac{-jZ_4 \cot\theta_4 \dfrac{1}{j\omega(C/2)}}{-jZ_4 \cot\theta_4 + \dfrac{1}{j\omega(C/2)}} \quad (17)$$

where $z_{mn}$ denote the Z-parameters of asymmetric coupled lines [75] (m, n=1 to 4); $C$ is the loading capacitance; $C_s$ is the matching capacitance of transformer; $Z_2$, $Z_3$, $Z_4$, $\theta_2$, $\theta_3$ and $\theta_4$ are the characteristic impedances and electrical lengths for the transmission line sections shown in the Figure above.

**Deriving the design parameters:**

The resonant frequencies of the even-mode ( $f_0^e$ ) and odd-mode ( $f_0^o$ ) may be determined from (4-5).

$$\mathrm{Im}[Z_{ine}] = 0 \qquad (18)$$

$$\mathrm{Im}[Z_{ino}] = 0 \qquad (19)$$

The external quality factor for even mode ( $Q_{exe}$ ) and odd mode ( $Q_{exo}$ ) may be determined from (20-21).

$$Q_{exe} = \frac{x_e}{Z_0} \qquad (20)$$

$$Q_{exo} = \frac{x_o}{Z_0} \qquad (21)$$

where $x_e$ , $x_o$ are the slope parameters of the even-and odd-mode, respectively, which are given by

$$x_e = \frac{f_o^e}{2} \cdot \left. \frac{\partial(\mathrm{Im}[Z_{ine}(f_0^e)])}{\partial f} \right|_{f=f_0^e} \qquad (22)$$

$$x_o = \frac{f_o^o}{2} \cdot \left. \frac{\partial(\mathrm{Im}[Z_{ino}(f_0^o)])}{\partial f} \right|_{f=f_0^o} \qquad (23)$$

## References


[1] J.-S. Hong and M. J. Lancaster, "Microstrip Filters for RF/Microwave Applications " *Wiley New York*, 2001.

[2] P. Jarry and J. Beneat, "Design and Realizations of Miniaturized Fractal RF and Microwave Filters," *Wiley, USA*, 2009.

[3] P. Jarry and J. Beneat, "Advanced Design Techniques and Realizations of Microwave and RF Filters," *Wiley-IEEE Press, USA*, 2008.

[4] I. Wolff, "Microstrip bandpass filter using degenerate modes of a microstrip ring resonator," *Electronics Letters*, vol. 8, pp. 302-303, 1972.

[5] J.-S. Hong and M. J. Lancaster, "Bandpass characteristics of new dual-mode microstrip square loop resonators," *Electronics Letters*, vol. 31, pp. 891-892, 1995.

[6] J.-S. Hong and M. J. Lancaster, "Microstrip bandpass filter using degenerate modes of a novel meander loop resonator," *Microwave and Guided Wave Letters, IEEE*, vol. 5, pp. 371-372, 1995.

[7] M. Matsuo, H. Yabuki, and M. Makimoto, "Dual-mode stepped-impedance ring resonator for bandpass filter applications," *Microwave Theory and Techniques, IEEE Transactions on*, vol. 49, pp. 1235-1240, 2001.

[8] E. Hanna, P. Jarry, E. Kerherve, and J. M. Pham, "A novel compact dual-mode bandpass filter using fractal shaped resonators," presented at Electronics, Circuits and Systems, 2006. ICECS '06. 13th IEEE International Conference on, 2006.

[9] J.-S. Hong and L. Shuzhou, "Theory and experiment of dual-mode microstrip triangular patch resonators and filters," *Microwave Theory and Techniques, IEEE Transactions on*, vol. 52, pp. 1237-1243, 2004.

[10] J.-S. Hong, H. Shaman, and C. Young-Hoon, "Dual-Mode Microstrip Open-Loop Resonators and Filters," *Microwave Theory and Techniques, IEEE Transactions on*, vol. 55, pp. 1764-1770, 2007.

[11] Y. H. Chun and J.-S. Hong, "Electronically reconfigurable dual-mode microstrip open-loop resonator filter," *IEEE Microw. Wireless Compon. Lett., vol. 18, no 7, pp. 449-451, Jul. 2008.*

[12] C. K. Liao, C. Y. Chang, and J. Lin, "A reconfigurable filter based on doublet configuration," *in IEEE MTT-S Int. Microw. Symp. Dig., Jun. 2007, pp. 1607-1610.*

[13] K. Jen-Tsai, Y. Tsung-Hsun, and Y. Chun-Cheng, "Design of microstrip bandpass filters with a dual-passband response," *Microwave Theory and Techniques, IEEE Transactions on*, vol. 53, pp. 1331-1337, 2005.

[14] M. Mokhtaari, J. Bornemann, and S. Amari, "New Reduced-Size Step-Impedance Dual-Band Filters with Enhanced Bandwidth and Stopband Performance," *Microwave Symposium Digest, 2006. IEEE MTT-S International June 2006 Page(s):1181 – 1184*

[15] K. K. M. Cheng and C. Law, "A New Approach to the Realization of a Dual-Band Microstrip Filter with Very Wide Upper Stopband," *Microwave Theory and Techniques, IEEE Transactions on*, vol. 56, pp. 1461-1467, 2008.

[16] S. Amari and M. Bekheit, "A New Class of Dual-Mode Dual-Band Waveguide Filters," *Microwave Theory and Techniques, IEEE Transactions on*, vol. 56, pp. 1938-1944, 2008.

[17] R. V. Snyder and S. Sanghoon, "Parallel coupled line notch filter with wide spurious-free passbands," presented at Microwave Symposium Digest, 2005 IEEE MTT-S International, 2005.

[18] R. Levy, R. V. Snyder, and S. Sanghoon, "Bandstop filters with extended upper passbands," *Microwave Theory and Techniques, IEEE Transactions on*, vol. 54, pp. 2503-2515, 2006.

[19] J.-S. Hong, "Reconfigurable planar filters," *Microwave Magazine, IEEE*, vol. 10, pp. 73-83, 2009.

[20] I. Hunter, "Theory and Design of Microwave Filters," *The Institution of Electrical Engineers, London*, 2001.

[21] B. W. Kim and S. W. Yun, "Varactor-tuned combline bandpass filter using step-impedance microstrip lines," *IEEE Trans. Microw. Theory Tech, vol. 52, no. 4, pp. 1279 – 1283*, Apr. 2004.

[22] M. Sanches-Renedo, R. Gomez-Garcia, J. I. Alonso, and C. Briso-Rodriguez, "Tunbale combline filter with continuous control of center frequency and bandwidth," *IEEE Trans. Microw. Theory Tech., vol. 53, no 1, pp. 191-199*, Jan. 2005.

[23] M. A. El-Tanani and G. M. Rebeize, "Corrugated microstrip coupled lines for constant absolute bandwidth tunable filters," *IEEE Trans. Microw. Theory Tech., vol. 58, no 4, pp. 956-963*, Apr. 2010.

[24] M. Koochakzadeh and A. Abbaspour-Tamijani, "Switchable bandpass filter for 0.3-0.6 GHz," *in IEEE MTT-S Int. Microw. Symp. Dig., Jun. 2007, pp. 557-560.*

[25] B. Carey-Smith, P. A. Warr, M. A. Beach, and T. Nesimoglu, "Wide Tuning-range planar filters using lumped distributed coupled resonators," *IEEE Trans. Microw. Theory Tech., vol. 53, no 2, pp. 777-785*, Feb. 2005.

[26] P. S. June and G. M. Rebeiz, "Low-Loss Two-Pole Tunable Filters With Three Different Predefined Bandwidth Characteristics," *IEEE Trans. Microw. Theory Tech, vol. 56, no. 5, pp. 1137 – 1148, May 2008.*

[27] X. Y. Zhang, Q. Xue, C. H. Chan, and B. J. Hu, "Low-loss frequency-agile bandpass filters with controllable bandwidth and suppressed second harmonic," *IEEE Trans. Microw. Theory Tech., vol. 58, no 6, pp. 1557-1564, Jun. 2010.*

[28] B. Kapilevich and R. Lukjanets, "Optimization of varactor tunable microstrip resonators for wireless applications," *in Russia Microw. Conf., 1999, pp. 1160-1167.*

[29] W. W. Peng and I. C. Hunter, "A New Class of Low-Loss High-Linearity Electronically Reconfigurable Microwave Filter," *IEEE Trans. Microw. Theory Tech., vol. 56, no. 8, pp. 1945-1953, Aug. 2008.*

[30] A. A. Tamijani, L. Dussopt, and G. M. Rebeiz, "Miniature and tunable filters using MEMS capacitors," *IEEE Trans. Microw. Theory Tech., vol. 51, no 7, pp. 1878-1885, Jul. 2003.*

[31] A. Pothier, J. C. Orlianges, G. Zheng, C. Champeaux, A. Catherinot, D. Cros, P. Blondy, and J. Papaolymerou, "Low-loss 2-bit tunable bandpass filters using MEMS DC contact switches," *IEEE Trans. Microw. Theory Tech., vol. 53, no 1, pp. 354-360, Jan. 2001.*

[32] G. M. Kraus, C. L. Goldsmith, C. D. Nordquist, C. W. Dyck, P. S. Finnegan, F. Austin, IV, A. Muyshondt, and C. T. Sullivan, "A widely tunable RF MEMS end-coupled filter," *in 2004 IEEE MTT-S Int. Microwave Symp. Dig., June 6–11, 2004, vol. 2, pp. 429–432.*

[33] P. Blondy, C. Palego, M. Houssini, A. Pothier, and A. Crunteanu, "RF-MEMS reconfigurable filters on low loss substrates for flexible front ends," *in Proc. Asia-Pacific Microwave Conf. 2007 (APMC 2007), Dec. 11–14, 2007, pp. 1–3.*

[34] K. Entesari and G. M. Rebeiz, "A differential 4-bit 6.5-10-GHz RF MEMS tunable filter," *IEEE Trans. Microwave Theory Tech., vol. 53, no. 3, part 2, pp. 1103–1110, Mar. 2005.*

[35] I. C. Reines, C. L. Goldsmith, C. D. Nordquist, C. W. Dyck, G. M. Kraus, T. A. Plut, P. S. Finnegan, F. Austin, IV, and C. T. Sullivan, "A low loss RF MEMS Ku-band integrated switched filter bank," *IEEE Microwave Wireless Compon. Lett., vol. 15, no. 2, pp. 74–76, Feb. 2005*.

[36] R. Zhang and R. R. Mansour, "Novel tunable lowpass filters using folded slots etched in the ground plane," *in 2005 IEEE MTT-S Int. Microwave Symp. Dig., June 12–17, 2005, pp. 775-778*.

[37] G. M. Rebeiz, K. Entesari, I. C. Reines, M. A. El-Tanani, A. Grichener, and A. R. Brown, "Tuning in to RF MEMS," *IEEE Microw. Magazine, vol. 10, no. 6, pp. 55-72, Oct. 2009*.

[38] L.-H. Hsieh and K. Chang, "Tunable microstrip bandpass filters with two transmission zeros," *IEEE Trans. Microw. Theory Tech., vol. 51, no 2, pp. 520-525, Feb. 2003*.

[39] W.-T. Tu and K. Chang, "Piezoelectric transducer-controlled dual-mode switchable bandpass filter," *IEEE Microwave Wireless Compon. Lett., vol. 17, no. 3, pp. 199–201, Mar. 2007*.

[40] Y. Poplavko, D. Schmigin, V. Pashkov, M. Jeong, and S. Baik, "Tunable microstrip filter with piezo-moved ground electrode," *in Eur. Microw. Conf., Oct. 2005, vol. 2*.

[41] H. Joshi, H. H. Sigmarsson, M. Sungwook, D. Peroulis, and W. J. Chappell, "High-Q Fully Reconfigurable Tunable Bandpass Filters," *Microwave Theory and Techniques, IEEE Transactions on*, vol. 57, pp. 3525-3533, 2009.

[42] Y.-H. Chun, J.-S. Hong, P. Bao, T. J. Jackson, and M. J. Lancaster, "BST varactor tuned bandstop filter with slotted ground structure," *in IEEE MTT-S Int. Microw. Symp. Dig., Jun. 2008, pp. 1115-1118*.

[43] J. Nath, D. Ghosh, J.-P. Maria, A. I. Kingon, W. Fathellbab, P. D. Franzon, and M. B. Steer, "An electronically tunable microstrip bandpass filter using thin-film

barium-strontium-titanate (BST) varactors," *IEEE Trans. Microw. Theory Tech., vol. 53, no 9, pp. 2707-2712, Sep. 2005*.

[44] Y. H. Chun, J.-S. Hong, B. Peng, T. J. Jackson, and M. J. Lancaster, "BST-Varactor Tunable Dual-Mode Filter Using Variable Zc Transmission Line," *Microwave and Wireless Components Letters, IEEE*, vol. 18, pp. 167-169, 2008.

[45] F. A. Miranda, G. Subramanyam, F. W. v. Keuls, R. R. Romanofsky, J. D. Warner, and C. H. Mueller, "Design and development of ferroelectric tunable microwave components for Ku and K-band satellite communication systems," *IEEE Trans. Microwave Theory Tech., vol. MTT-48, no. 7, pp. 1181–1189, July 2000*.

[46] P. M. Suherman, T. J. Jackson, Y. Y. Tse, I. P. Jones, R. I. Chakalova, and M. J. Lancaster, "Microwave properties of Ba0.5Sr0.5TiO3 thin film coplanar phase shifters," *Journal of Applied Physics, Vol. 99, No. 104101, pp. 1-7 May 2006*.

[47] G. L. Matthaei, L. Young, and E. M. T. Jones, "Microwave Filters, Impedance-Matching Networks, and Coupling Structures," *Artech House, Norwood, MA*, 1980.

[48] J. Nath, D. Ghosh, J. P. Maria, A. I. Kingon, W. Fathelbab, P. D. Franzon, and M. B. Steer, "An electronically tunable microstrip bandpass filter using thin-film Barium-Strontium-Titanate (BST) varactors," *Microwave Theory and Techniques, IEEE Transactions on*, vol. 53, pp. 2707-2712, 2005.

[49] J.-S. Hong and M. J. Lancaster, "Couplings of microstrip square open-loop resonators for cross-coupled planar microwave filters," *IEEE Trans. Microw. Theory Tech., vol. 44, no 11, pp. 2099-2109, Nov. 1996*.

[50] J.-S. Hong, "Microstrip Filters for RF/Microwave Application," *Second Edition, Wiley*, 2010.

[51] J. A. Curitis and S. J. Fiedziuszko, "Miniature dual mode microstrip filters," *IEEE MTT-S Dig., 1991, pp.443-446*.

[52] R. R. Mansour, "Design of superconductive multiplexers using single-mode and dual-mode filters," *IEEE Trans., 1994, MTT-42, pp.1411-1418*.

[53] C. Lugo and J. Papapolymerou, "Bandpass Filter Design Using a Microstrip Triangular Loop Resonator With Dual-Mode Operation," *IEEE Microwave and Wireless Components Letters, Vol. 15, No. 7, pp.475-477, Jul. 2005*.

[54] R. Wu and S. Amari, "New Triangular Microstrip Loop Resonators For Bandpass Dual-Mode Filter Applications," *IEEE MTT-S Dig., 2005, pp.941-944*.

[55] H. A. Wheeler, "Transmission line properties of parallel strips separated by a dielectric sheet," *IEEE Trans., MTT-13, May 1965*.

[56] M. Cuhaci and D. S. James, "Radiation from triangular and circular resonators in microstrip," *in IEEE MTT-S Int. Microwave Symp. Dig., 1977, pp. 438–441*.

[57] S. Wu and B. Razavi, "A 900-MHz/1.8-GHz CMOS receiver for dual band applications," *IEEE J. Solid-State Circuits, vol. 33, no. 12, pp.2178–2185, Dec. 1998*.

[58] J. Ryynänen, K. Kivekäs, J. Jussila, A. Pärssinen, and K. A. I. Halonen, "A dual-band RF front-end for WCDMA and GSM applications," *IEEE J. Solid-State Circuits, vol. 36, no. 8, pp. 1198–1204, Aug. 2001*.

[59] D. Llorens, P. Otero, and C. Camacho-Penalosa, "Dual-band, single CPW port, planar-slot antenna," *IEEE Trans. Antennas Propagat., vol. 51, no. 1, pp. 137–139, Jan. 2003*.

[60] Y.-L. Kuo and K.-L. Wong, "Printed double-T monopole antenna for 2.4/5.2 GHz dual-bandWLANoperations," *IEEE Trans. Antennas Propagat., vol. 51, no. 9, pp. 2187–2192, Sep. 2003*.

[61] R. J. Cameron, Y. Ming, and W. Ying, "Direct-coupled microwave filters with single and dual stopbands," *Microwave Theory and Techniques, IEEE Transactions on, vol. 53, pp. 3288-3297, 2005*.

[62] G. Macchiarella and S. Tamiazzo, "Design techniques for dual-passband filters," *Microwave Theory and Techniques, IEEE Transactions on, vol. 53, pp. 3265-3271, 2005*.

[63] M. Mokhtaari, J. Bornemann, K. Rambabu, and S. Amari, "Coupling-Matrix Design of Dual and Triple Passband Filters," *Microwave Theory and Techniques, IEEE Transactions on Volume 54, Issue 11, Nov. 2006 Page(s):3940 – 3946*.

[64] Y. Zhang, K. A. Zaki, J. A. Ruiz-Cruz, and A. E. Atia, "Analytical Synthesis of Generalized Multi-band Microwave Filters," *Microwave Symposium, 2007. IEEE/MTT-S International 3-8 June 2007 Page(s):1273 – 1276*.

[65] J. T. Kuo, T. H. Yeh, and C.C.Yeh, "Design of microstrip bandpass filters with a dual-passband response," *IEEE Trans. Microw. Theory Tech., 2005, 53, (4), pp. 1331–1337*.

[66] K.-K. M. Cheng and C. Law, "A New Approach to the Realization of a Dual-Band Microstrip Filter With Very Wide Upper Stopband," *Microwave Theory and Techniques, IEEE Transactions on, Volume 56, Issue 6, June 2008 Page(s):1461 – 1467*.

[67] P. Mondal and M. K. Mandal, "Design of dual-band bandpass filters using stub-loaded open-loop resonators," *IEEE Trans. Microw. Theory Tech., vol. 56, no 1, pp. 150-155, Jan. 2008*.

[68] S. K. Alotaibi, J.-S. Hong, and Z. C. Hao, "Multilayer folded-waveguide dual-band filter," *Microwave Symposium Digest, 2008 IEEE MTT-S International, 15-20 June 2008 Page(s):731 -734*.

[69] M. Mokhtaari, J. Bornemann, and S. Amari, "New Reduced-Size Step-Impedance Dual-Band Filters with Enhanced Bandwidth and Stopband Performance," presented at Microwave Symposium Digest, 2006. IEEE MTT-S International, 2006.

[70] W. R., A. S., and R. U, "New cross-coupled microstrip band reject filters," *IEEE MTT-S Digest, 2004, pp. 1597–1600*.

[71] J.-S. Hong, "Microstrip dual-mode band reject filter," *2005 IEEE Int. Microwave Symp. Digest, Long Beach, USA, June 2005*.

[72] D. K., M. M.K., and S. S, "Sharp-rejection wideband bandstop filters," *IEEE Microw. Wirel. Compon. Lett., 2008, 18, (10), pp. 662–664*.

[73] H. Shaman and J.-S.Hong, "Wideband bandstop filter with cross coupling," *IEEE Trans. Microw. Theory Tech., 2007, MTT-55, (8), pp. 1780–1785*.

[74] D. Pozar, "Microwave Engineering," *John Wiley and Sons Inc., NY.* , 1998.

[75] R. K. Mongia, I. J. Bahi, P. Bhartia, and J.-S. Hong, "RF and Microwave Coupled-Line Circuits," *Artech House, Inc.* , 2007.

[76] R. J. Cameron, "General coupling matrix synthesis methods for Chebyshev filtering functions," *Microwave Theory and Techniques, IEEE Transactions on*, vol. 47, pp. 433-442, 1999.

[77] R. J. Cameron, "Advanced coupling matrix synthesis techniques for microwave filters," *Microwave Theory and Techniques, IEEE Transactions on*, vol. 51, pp. 1-10, 2003.

[78] S. Amari, U. Rosenberg, and J. Bornemann, "Adaptive synthesis and design of resonator filters with source/load-multiresonator coupling," *Microwave Theory and Techniques, IEEE Transactions on*, vol. 50, pp. 1969-1978, 2002.

[79] "EM User's Manual, Version 12.52," *Sonnet Software Inc., North Syracuse, NY,* , 2009.

[80] M. Makimoto and S. Yamashita, "Bandpass Filters Using Parallel Coupled Stripline Stepped Impedance Resonators," *Microwave Theory and Techniques, IEEE Transactions on*, vol. 28, pp. 1413-1417, 1980.

[81] J.-S. Hong and M. J. Lancaster, "End-coupled microstrip slow-wave resonator filter," *Electronics Letters*, vol. 32, pp. 1494-1496, 1996.

[82] J.-S. Hong and M. J. Lancaster, "Theory and experiment of novel microstrip slow-wave open-loop resonator filters," *Microwave Theory and Techniques, IEEE Transactions on*, vol. 45, pp. 2358-2365, 1997.

[83] A. F. Harvey, "Periodic and Guiding Structures at Microwave Frequencies," *Microwave Theory and Techniques, IRE Transactions on*, vol. 8, pp. 30-61, 1960.

[84] "AVX Accu-P data sheet," *AVX Corporation, Myrtle Beach, SC,* , 2006.

[85] "M/A COM MA46H202 data sheet," *M/A COM, Lowell, MA,*, 2006.

[86] S. Amari, U. Rosenberg, and J. Bornemann, "Singlets, cascaded singlets, and the nonresonating node model for advanced modular design of elliptic filters," *Microwave and Wireless Components Letters, IEEE*, vol. 14, pp. 237-239, 2004.

[87] V. Osipenkov and S. G. Vesnin, "Microwave filters of parallel-cascade structure," *Microwave Theory and Techniques, IEEE Transactions on*, vol. 42, pp. 1360-1367, 1994.

[88] M. Sagawa, M. Makimoto, and S. Yamashita, "Geometrical structures and fundamental characteristics of microwave stepped-impedance resonators," *Microwave Theory and Techniques, IEEE Transactions on*, vol. 45, pp. 1078-1085, 1997.

[89] "Microwave office user's manual," *Applied Wave Research Inc. version 7.5*, 2007.

[90] R. Phromloungsri, M. Chongcheawchamnan, and I. D. Robertson, "Inductively Compensated Parallel Coupled Microstrip Lines and Their Applications," *Microwave Theory and Techniques, IEEE Transactions on*, vol. 54, pp. 3571-3582, 2006.

[91] Y. H. Chun, C. Fragkiadakis, B. Peng, A. Luker, R. V. Wright, J.-S. Hong, P. B. Kirby, Z. Qi, T. J. Jackson, and M. J. Lancaster, "Tunable Bandstop Resonator and Filter on Si-Substrate with PST Thin Film by Sol-Gel Deposition," presented at Microwave Conference, 2008. EuMC 2008. 38th European, 2008.

[92] W. Tang and J.-S. Hong, "Varactor-Tuned Dual-Mode Bandpass Filters," *Microwave Theory and Techniques, IEEE Transactions on*, vol. 58, pp. 2213-2219, 2010.

[93] W. Tang and J.-S. Hong, "Microstrip quasi-elliptic function bandpass filter with improved tuning range," presented at Microwave Conference (EuMC), 2010 European, 2010.

[94] W. Tang, J.-S. Hong, and Y.-H. Chun, "Compact Tunable Microstrip Bandpass Filters with Asymmetrical Frequency Response," presented at Microwave Conference, 2008. EuMC 2008. 38th European, 2008.

[95] W. Tang and J.-S. Hong, "Tunable microstrip quasi-elliptic function bandpass filters," presented at Microwave Conference, 2009. EuMC 2009. European, 2009.

[96] W. Tang and J.-S. Hong, "Quasi-elliptic function doublet filters without cross coupling," presented at Microwave Conference, 2009. EuMC 2009. European, 2009.

[97] W. Tang and J.-S. Hong, "Parallel Feed Microstrip Quasi-Elliptic Function Bandpass Filter," *accepted by Microwave Conference (EuMC), 2011 European*

[98] J.-S. Hong and W. Tang, "Dual-band filter based on non-degenerate dual-mode slow-wave open-loop resonators," presented at Microwave Symposium Digest, 2009. MTT '09. IEEE MTT-S International, 2009.

[99] W. Tang and J.-S. Hong, "Coupled stepped-impedance-resonator bandstop filter," *Microwaves, Antennas & Propagation, IET*, vol. 4, pp. 1283-1289, 2010.

[100] W. Tang, J.-S. Hong, and Y.-H. Chun, "Microstrip cross-coupled stepped-impedance line bandstop filter," presented at Microwave Symposium Digest, 2009. MTT '09. IEEE MTT-S International, 2009.